Alma Mater Studiorum · Università di Bologna

Scuola di Scienze
Dipartimento di Fisica e Astronomia
Corso di Laurea in Fisica

Quality test and construction of the prototype SiPM optical readout plane for the ePIC-dRICH detector at the EIC

Relatore:
Prof. Gilda Scioli

Correlatore:
Dott. Roberto Preghenella

Presentata da:
Elena Mariotti

Anno Accademico 2023/2024

Sommario

L'Electron-Ion Collider (EIC) è un acceleratore di particelle in fase di realizzazione presso i laboratori nazionali di Brookhaven negli USA e permetterà di approfondire le nostre conoscenze sulla natura dell'interazione forte e sulla struttura nucleare, analizzando collisioni di elettroni con nuclei e protoni. Presso EIC l'esperimento ePIC prevede un sistema di identificazione di particelle, per il quale è previsto l'utilizzo nella regione in avanti di un rivelatore dual-radiator RICH. Quest'ultimo prevede l'impiego di due radiatori, in modo tale da coprire un intervallo di impulsi ampio, e l'integrazione di fotorivelatori per rivelare l'emissione di luce Cherenkov per risalire alla massa delle particelle. I fotorivelatori previsti sono i sensori al silicio SiPM.
L'obbiettivo di questo lavoro di tesi è stata la preparazione, la caratterizzazione, lo studio delle prestazioni e la messa in funzione di un prototipo del rivelatore dRICH per il test beam svolto a Maggio 2024. In particolare l'attività si concentra sui test di verifica della performance dei sistemi di controllo, quali i termistori NTC (Negative Temperature Coefficient), che tramite una resistenza variabile misurano la temperatura dei fotorivelatori, del corretto funzionamento di tutti i più di 2000 canali SiPM tramite una misura del loro Dark Count Rate, della verifica delle prestazioni termiche del sistema di raffreddamento, basato su componenti termoelettrici e sul processo di assemblaggio e test di comunicazione finale del prototipo costruito.
I test svolti hanno evidenziato che tutti i singoli componenti del rivelatore funzionavano correttamente entro i requisiti e comunicavano tra loro in modo ottimale, permettendo una buona riuscita del test beam.

Contents

Introduction

The Electron-Ion-Collider (EIC) will be a new high luminosity and high-polarization particle collider designed to investigate the nuclear structure and the strong interaction, that will be built at Brookhaven National Laboratory in the US.
The design taken in consideration in the ePIC experiment for the detector design comprehends a particle identification system. One of its key elements is the dual-radiator Ring Imaging Cherenkov (dRICH) detector that provides particle identification in the hadronic cap. The dRICH will involve the use of silicon photomultipliers (SiPM) to detect Cherenkov radiation, semiconductor photodetectors consisting of an array of single photon avalanche diodes (SPADS) with a single photon detection capability. The work here presented concerns the process of assembly and performance testing of the dRICH prototype for the test beam held in May 2024 at CERN. This prototype of the dual-radiator RICH for EIC aims to identify particles in the broad momentum range from a few GeV/c up to 50 GeV/c allowing a 3σ separation of particles, while operating in a high magnetic field, by combining the information provided by two radiators, aerogel and gas C_2F_6. The dRICH exploits Cherenkov light produced by these two mediums without penalty owing to the gas Cherenkov threshold. The fully equipped box features 2048 channels in a total box volume of 20 x 20 x 20 cm^3.

Chapter 1 evolves around the Electron Ion Collider, gives an overview on the scientific goals it aims to achieve and describes the main detectors involved in its facility with a closer examination of the dRICH.

Chapter 2 introduces the three main components of the dRICH detector concept and readout system, that have been majorly used in the experimental setups of this study: Silicon Photomultipliers (structure and possible noise sources), Peltier modules, and the ALCOR ASICS prototype for the SiPMs readout. Each component is analyzed previously through the physics operating principle it relies on and then in the designs considered for the prototype.

Chapter 3 presents an overview of the experimental equipment and setup for the test beam succeeded by a description of the characterization and quality tests carried out on every component of the dRICH prototype and its results. The tests on the NTC temperature sensors, on the DCR SiPMs communication and on the Integrated cooling system along with the obtained results are presented. Finally, is described the assembly and pre-commissioning test process of the dRICH prototype with some of the test beam results.

Chapter 1

Electron Ion Collider

The Elecron-Ion Collider (EIC) is a new 2.4-mile-circumference particle accelerator. Its start up is expected in the early part of the 2030s in the United States of America at Brookhaven National Laboratory on Long Island. As represented in Figure 1.1 it is based on the existing Relativistic Heavy Ion Collider (RHIC). The EIC is designed to collide two accelerated, polarized beams of particles, bringing high-energy electrons into head-on, high-intensity collisions with high-energy protons or ions. This one will be the first polarized electron-ion collider consenting operations at high collision luminosity. Using sophisticated and large detectors EIC will provide precise measurements that will enable us to study more thoroughly the nuclear structure and the nuclear strong force. The fundamental constituent of nucleons, which are baryons, are quarks, that are kept together through strong interaction. Gluons are bosonic particles and are the mediators of the strong force and have color charge. Gluons and quarks are collectively called partons. These elements, their color charge and interactions fall within the scope of Quantum Chromo-Dynamics (QCD) theory contained in the Standard Model. The strong force between quarks and gluons is attributed to their color charge. This causes the gluons to interact with each other, generating a significant fraction of the nucleon mass and leading to a little-explored regime of matter. Hints of this regime become manifest when nucleons or nuclei collide at nearly the speed of light. The quantitative study of matter in this new regime requires a new experimental facility: an Electron Ion Collider [1]. The EIC aims to research the origin of the nucleon's mass and spin, the distribution of momenta and position of partons inside the nucleon and the properties of dense system of gluons. The EIC will have the capability to inspect these aspects in only one facility, thanks to the beam polarization and species (from light to heavy-ion beams and proton beams) and to its wide energy range.

1.1 The Accelerator

The high-intensity beams will be polarized and will collide in specific places. In these sites will be placed a complex detector structure to obtain high precision measurements. The EIC machine aims to achieve the features listed below [3]:

- Highly polarized beams of electron and nucleon;
- Ion beams from deuteron to heaviest nuclei such as uranium (U) or lead (Pb);
- Variable $e+p$ center of mass energies between 20-100 GeV, upgradable to $\sim$ 140 GeV. This energy is needed to provide sufficient kinematic to reach the gluon dominated regime [2];

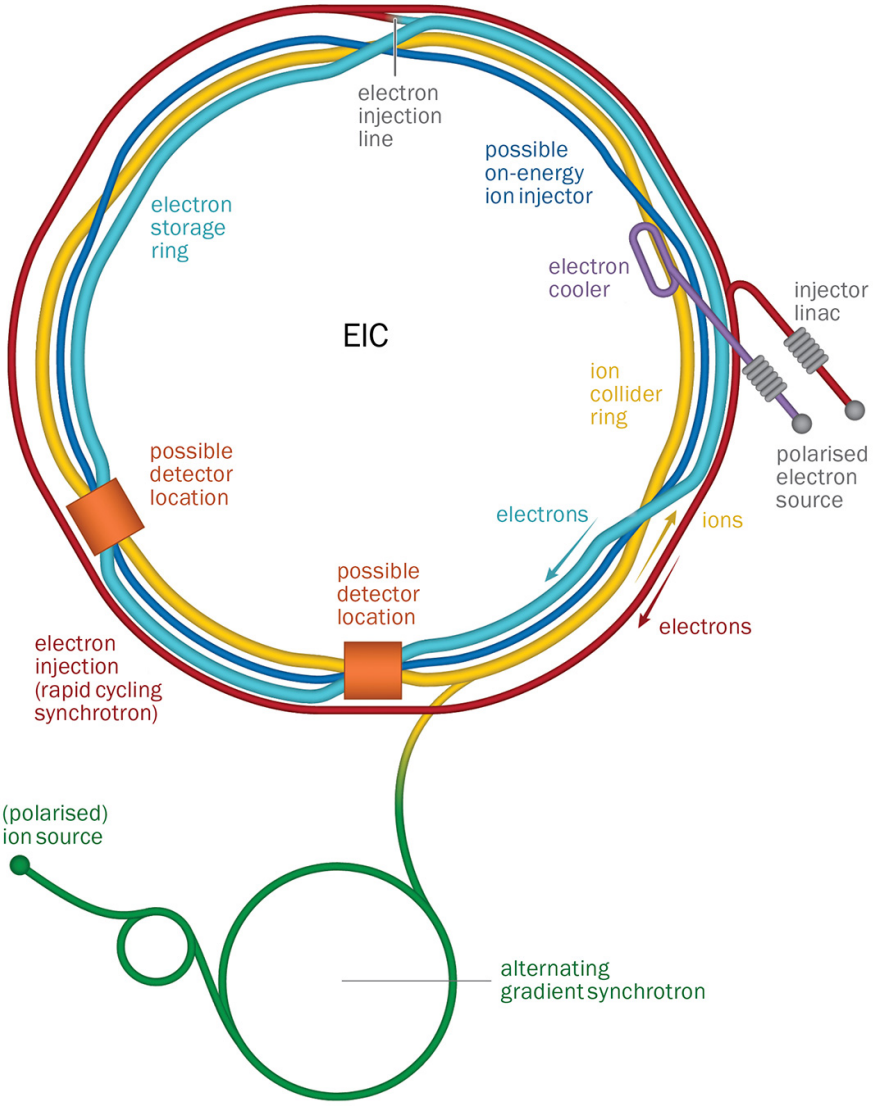

Figure 1.1: Schematic layout of the planned EIC accelerator based on the existing RHIC complex at Brookhaven National Laboratory [2].

- High collision luminosity $\sim 10^{33} - 10^{34}\,\mathrm{cm}^{-2}\mathrm{s}^{-1}$;
- Possibility to have more than one interaction region;
- Compact calorimetry, tracking, particle identification and high radiation tolerance for electronics.

1.2 Phisics observables

In this section will be introduced and briefly described the physics topics that the Elecron-Ion Collider will address. This new particle accelerator will specifically investigate how the nucleon mass and spin arise from the strong interaction between color-charged partons, how the latter ones are distributed in terms of momentum (including its transversal component) and space inside the nucleon and how a dense nuclear environment shapes their dynamics. The quarks are six of the fundamental fermionic particles described by the Standard Model, illustrated in Figure 1.2. Their color charge allows them to

participate in the strong interaction by exchanging gluons. The exchange of energy and momentum between quarks through the strong interaction inside the nucleon is a virtual effect, so virtual quark-antiquark pairs can be produced, which in turn can either emit a gluon or create more complex phenomena. Real quarks are called **valence quarks** while virtual quarks, anti-quarks and gluons are referred to as **sea**.

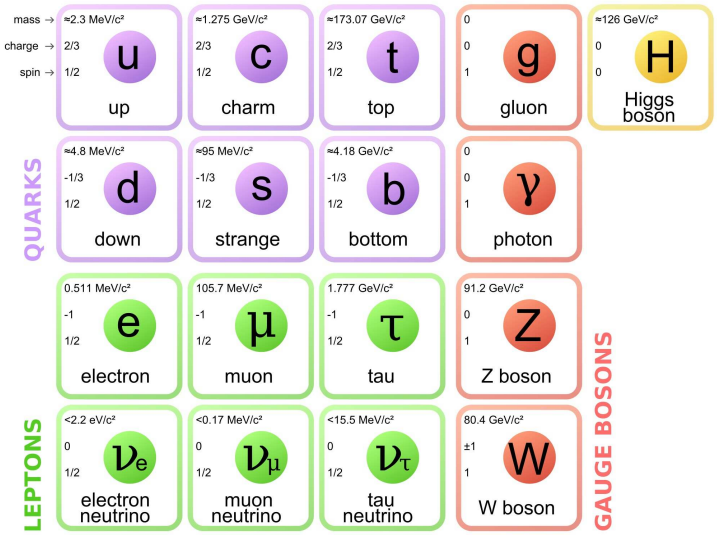

Figure 1.2: Scheme of the Standard Model's elementary particles [4].

The complexity of this model makes it necessary to be studied in high energy conditions, with the high speed collisions of the EIC.

1.2.1 Proton spin

Previous studies involving deep inelastic scattering (DIS) on nucleons using electron or muon beams have not fully clarified how partons share the spin of the nucleon and build up other nucleon intrinsic properties, such as its mass and magnetic moment [3], providing only a one-dimensional description of nuclear structure. The EIC will provide multi-dimensional maps of nucleon properties and with high energy probes of partons' transverse momenta it will clarify the role of their orbital motion contributing to nucleon spin.

Quarks and anti-quarks determine only the 30% of the proton spin. Additionally, RHIC results confirmed the presence of a non-zero gluon spin contribution, which is however not yet sufficient to account for the remaining 70%.

The EIC will allow us to lower the minimum momentum fraction accessible x[1] reaching two orders of magnitude lower and to cover a wider range of momentum transfer Q. The total helicity contribution of the partons to the proton spin is sensitive to the x accessible by the experiment. This leads to reduce measurements uncertainties, as shown in Figure 1.3, precisely quantifying the contributions of partons' spin and sea quarks to the total spin of the proton.

[1]Bjorken's x is a dimensionless variable used in deep inelastic scattering experiments to describe the fraction of the momentum of a hadron carried by a struck parton. It is defined as $x = \frac{Q^2}{2P \cdot q}$, where Q^2 is the negative square of the four-momentum transfer, P is the four-momentum of the target hadron, and q is the four-momentum of the virtual photon exchanged in the scattering process. It plays a crucial role in parton distribution functions (PDFs) and is an essential parameter in describing the internal structure of hadrons.

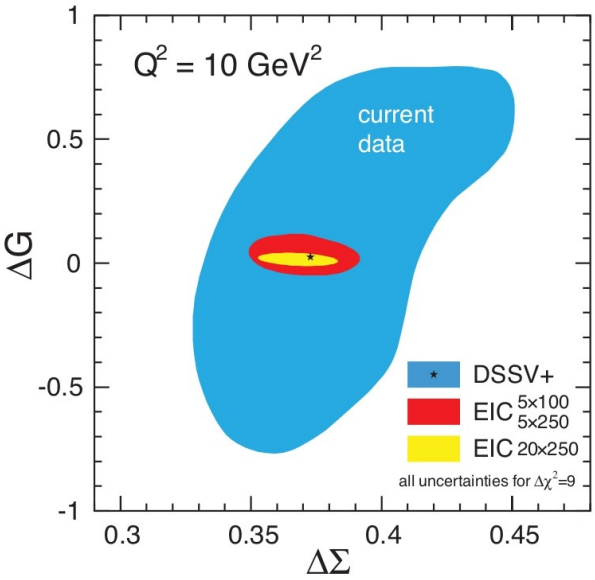

Figure 1.3: Reduction in the uncertainities of the gluon's helicity (spin's projection in momentum direction) contribution ΔG vs the quark helicity contribution $\Delta\Sigma$ to the proton spin from the region of parton momentum fractions $x > 0.001$, which would be achieved by the EIC for different center-of-mass energies [3].

1.2.2 Confined Motion of Partons inside the Nucleon

The confined motion and spin of partons inside a fast-moving nucleon are linked to transverse momentum-dependent parton distributions (TMDs). The spin-orbit coupling among partons, which is mostly unknown to date, can explain the correlation between parton motion, their spin and the spin of the parent nucleon. Thus, using in the EIC electron and nucleon polarized beams, TMDs allow to investigate the three-dimensional dynamics of the proton, going forward the so far known information about longitudinal momentum in conventional parton distributions. The Electron-Ion Collider will be the first facility capable of exploring the internal 3-dimensional sea quark and gluon structure of fast-moving nucleons and nuclei [3].

1.2.3 Tomography of the Nucleon

The EIC by probing the transversal spatial distribution of partons as a function of their longitudinal momentum fraction, can obtain an image of the proton complementary to the one obtained from the transverse momentum distribution. Therefore, EIC can provide a tomographic image of the proton with a level of accuracy on the transversal distances better than any other existing facility. This imaging technique can provide information about spin-orbit correlation and about the angular momentum, spin and orbital motion of partons.

1.2.4 Gluon saturation

When nuclei are accelerated, their relativistic motion flattens them generating an overlap of gluons that start a non-linear process of gluon-gluon recombinations. Seeing evidence of recombination can lead to proving that gluons reach a postulated steady state called saturation, where gluon splitting and recombination balance out [5]. In QCD this self-regulating process gives rise to the saturation scale (Q_s) where the gluon density is

expected to reach a balance. Observing this phenomenon can lead to find new universal properties of hadronic matter in the Color Glass Condensate[2] (CGC) state, schematized in Figure 1.4. Thanks to the EIC capability of accelerating heavy ions it will access more easily the saturation scale. The abundant presence of quarks involved in the process results in a minor kinematic energy needed to reach gluon saturation. Thus, EIC could for the first time reliably quantify the nuclear gluon distribution over a wide range of momentum fraction x [3].

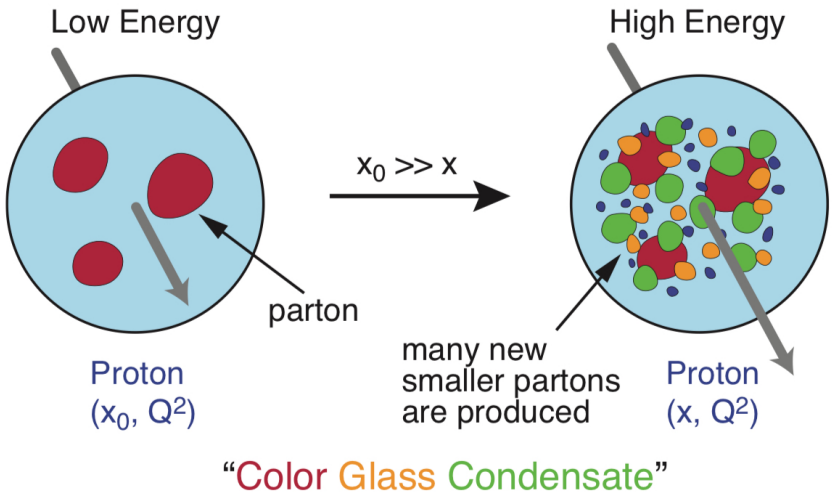

Figure 1.4: [3] On the left, configuration of protons for high x (Bjorken variable representing the momentum fraction of the parton on which the photon scatters). On the right a scheme for low x ($x = Q^2/W^2$(W^2 is the center-of-mass energy squared of the photon-proton system, therefore small x corresponds to high-energy scattering) where new partons can be seen. The figure is a projection on the plane transverse to the beam axis (the latter is shown by arrows coming out of the page, with the length of the arrows reflecting the momentum of the proton).

1.2.5 Passage of Color Charge Trough Cold QCD Matter

During a $e+A$ scattering, in the regime of standard perturbative QCD (high Q^2 and from moderate to high x), the electron can lose its energy via transmission of virtual photons. The latter ones interact with nucleon's quarks. The struck quark in turn interacts with other color charges while traversing the nucleus, continually losing energy. As soon as it leaves the nuclear environment it binds in color-neutral hadrons. This process is known as Quark Hadronization. The Elecron-Ion Collider providing a wide variety of ion beams could give insights into how this cold nuclear matter is formed during an electron-nucleus collision. The location of measurements within the shaded area, represented in Figure 1.5, can provide new pieces of information on when mesons are formed and what governs the transition from quarks to hadrons.

[2]Color Glass Condensate: "Color" refers to the eight types of color charge that the can be carried by Gluons. "Glass" represent the disordered state of elements changing their positions and "condensate" refers to the high density of the state.

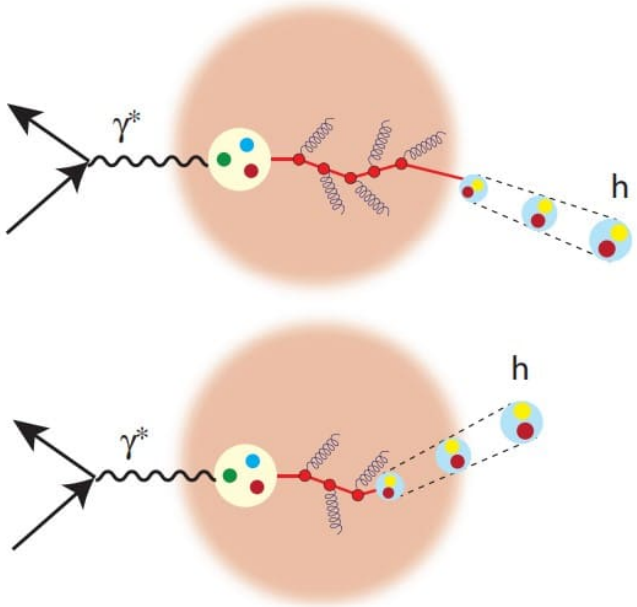

Figure 1.5: [3] Illustration of the interaction of a parton moving through cold nuclear matter. The $\gamma*$ represents a virtual photon. The hadron is formed outside (top) or outside (bottom) of the nucleus.

1.3 Detectors

EIC Detectors will provide the detailed measurements needed to explore the physical observables described in the previous section. The location of the ePIC detector is the one nearer to the synchrotron, named Detector II in Figure 1.6. The structure consists in a well-equipped central detector situated in the interaction region, where is available a space approximately 10 m long, and includes the instrumentation of the small angle regions, indicatively covering angles below 2°, in the forward and backward directions, with detectors situated along the collider beamlines. In the central detector, a 1.7 T superconducting solenoid provides the magnetic field for momentum analysis [6]. The detector is organized in three regions barrel, forward and backward. To characterize the four-vector of each particle involved in the electron-ion collision over the range $\sim 10MeV/\sim 10GeV$ of momenta, the detector will be integrated with forward and backward detectors, particle tracking, precision energy measurements and particle identification. This project aims to combine complementary detector technologies operating in one facility with high efficiency, despite taking data with a large rate background due to the circulating hadron beams. It will cover a wide momentum range of $3 - 40GeV/c$ (dual radiator RICH), working in a high magnetic field (SiPM), fitting in a limited space, the asymmetry of the $e + A$ collisions and working with a wide variety of particles .
The detector design is made up of three different main systems, outlined in Fgure1.7, listed below:

- The inner system for particle tracking and vertexing. The detector combines semiconductors that collect electron/hole pairs, caused by the passage of charged particles, with a gas-based tracking technology that collects ionization caused by tracks;
- The outer system is calorimetry that measures energy for electrons and hadrons.

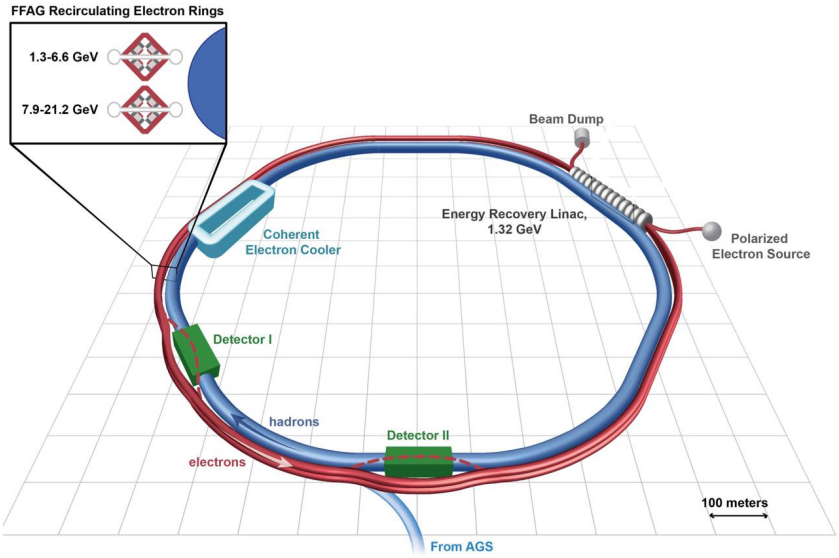

Figure 1.6: Schematic of the eRHIC [3]

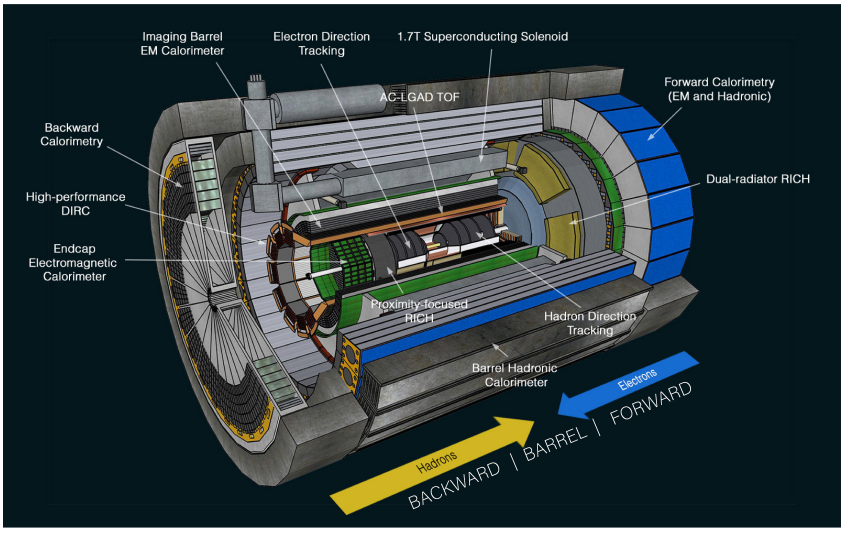

Figure 1.7: Cutaway view of the ePIC detector[7]

Currently for these measurements are considered SiPMs together with short radiation length material.

- A system for particle identification (PID) that allows to distinguish electrons from other particles like pions, kaons and protons through detectors based on Cherenkov radiation.

1.3.1 Particle identification: dRICH

The Dual-Radiator Ring Imaging Cherenkov detector (dRICH) determines the identity of the track originated by $e + A$ collisions in the forward end-cap, using detectors based on Cherenkov radiation and the time-of-flight (TOF, barrel region) measurements. To fully identify a charged particle, it is necessary to know its charge and its mass. The charge is determined by analyzing the Lorentz curvature of the particle's track and its mass can be obtained by variables measured with dRICH.
In the dRICH prototype the scattered particle crossing the detector passes through the

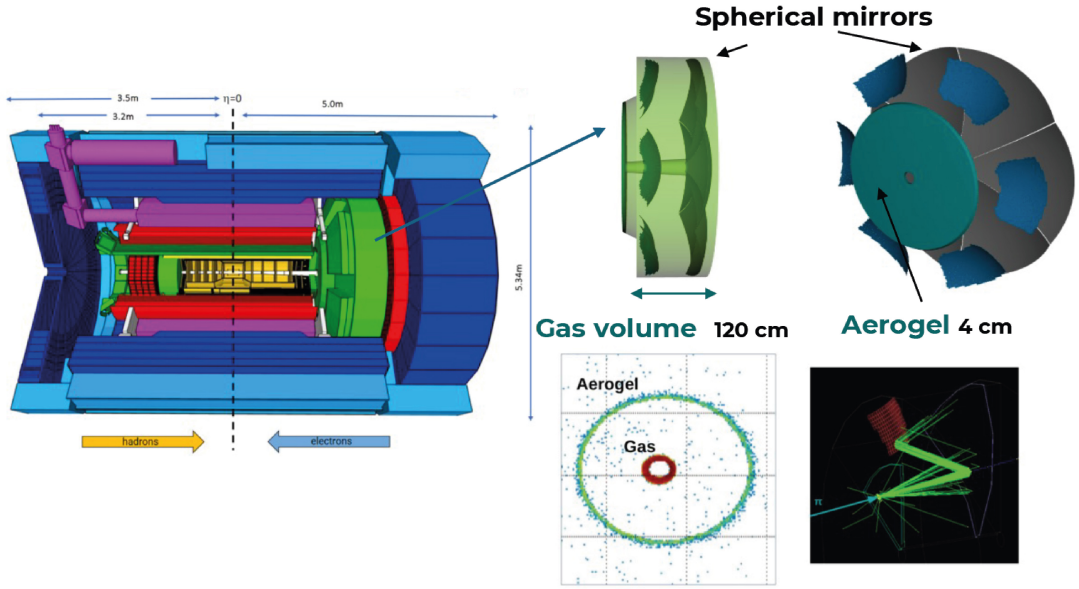

Figure 1.8: Scheme of dRICH(represented in green) pointing out the positions of the two radiators[8].

radiator media and produces a Cherenkov-photons cone (11° aperture for aerogel and 2° for the gas). This is then reflected by a spherical mirror into the photon detector direction.
To detect particles in different momentum ranges the dRICH comprises **aerogel** and gaseous $\mathbf{C_2F_6}$ cherenkov radiators with different refractive indexes ($n = 1.02$ and $n = 1.008$ respectively), see Figure 1.8. This feature consents a continuous forward particle detection in the extended $3 - 50\ GeV/c$ momentum interval and will enable dRICH to cover the range $\eta \sim 1.5 - 3.5$ of pseudorapidity in the forward ion-side region. Finally in terms of particle recognition electron identification will be up to $15\,GeV/c$ and the coverage at forward rapidity will be $\pi/k\,3\sigma$ separation for pi/k at $50\,GeV/c$

The detector is made up of six identical open sectors, $0.5m^2$ each, which share the same outward focusing mirror. In these areas are placed highly segmented photosensors clustered in several Photon Detector Units (PDU), on which this study is mainly focused. For the dRICH readout system has been chosen SiPMs with $3 \times 3\,mm^2$ pixels, organized as in Figure 1.9, because of their Single photon sensitivity ($\sim$ 10phs per Cherenkov event), good timing performance (<100 ps) and their insensitivity to magnetic fields (due to photosensor dimension). On the other side, SiPMs are highly radiation sensitive and have a high dark count rate. These properties will require attention in the testing phase, such as using an integrated cooling system to mitigate dark count rate effects.

1.3.2 Cherenkov radiation

Cherenkov radiation is emitted by charged particles moving through an optically transparent (dielectric) medium, with a speed greater than the phase velocity of light in that medium.
Imaging Cherenkov detectors are used to exploit Cherenkov light emission by particles produced from a collision. RICH produces an image of a circumference, from its radius the angle of incidence θ_c can be reconstructed and with θ_c is possible to evaluate the particle's identity.
The characteristic emission angle θ_c depends on the particle speed v and the refraction

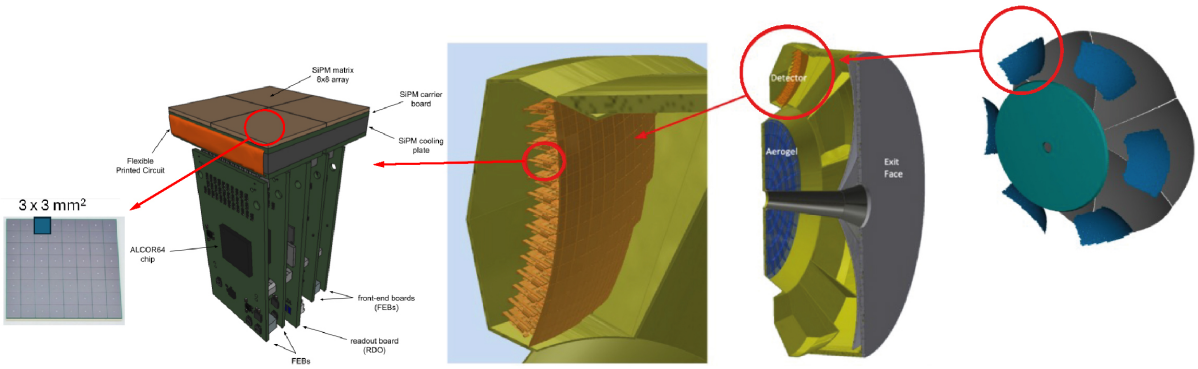

Figure 1.9: Structure of a single PDU, SiPMs organization and position inside the Dual-Radiator RICH

index of the medium n [9]:

$$\cos\theta = \frac{1}{n\beta}; \tag{1.1}$$

with $\beta = v/c$, c is the speed of light in vacuum. Cherenkov radiation is emitted only above a threshold velocity v_{thres}, given by:

$$|\cos\theta_c| \geq 1 \;\rightarrow\; \beta_{\text{thres}} = \frac{v_{\text{thres}}}{c} \geq \frac{1}{n}, \rightarrow\; v_{\text{thres}} \geq \frac{c}{n}; \tag{1.2}$$

Thus Cherenkov light is emitted exclusively when the particle's velocity is greater than the light's speed in that medium. Having measured θ_c with the detector, a measure of v is derived through Eq. 1.1. With v the **mass** and consequently the identification of the particle can be obtained through:

$$m = \frac{p}{\gamma\beta c}. \tag{1.3}$$

Chapter 2

Single photon readout with Silicon Photomultipliers

In this chapter are described three main components of the SiPM photodetector prototype for particle identification, subject of this study. In Section 2.1 semiconductor detectors are introduced, specifically Silicon Photomultipliers and its main features, which are widely used for photons detection in high-energy physics and, as mentioned before, is the thecnology selected for the dRICH detector. Section 2.2 focuses on the Peltier modules as part of the prototype cooling system for the SiPM and Section 2.3 describes the ALCOR front-end ASIC chip used for data collection and readout.

2.1 Photon detection with Silicon Photomultiplier

2.1.1 Semiconductors and P-N juction

Solid-state detectors use non compound semiconductor materials made up of elements from the IV group of the periodic table. These detectors, like the ones implemented in EIC, usually use silicon, whose atoms are organized in a tetrahedral lattice structure. Pure silicon crystals have positive and negative carriers (*holes* and *electrons*) in a steady equilibrium, a state called *intrinsic*.
The potential that characterizes crystalline structure, with the increase of reticular atomic distances, becomes a periodic space function where in every site its value is the result of every atom's contribution. While inner electronic levels are not influenced by other atoms' presence, electrons in the outer shells are. That is because the valence electrons are common to several atoms.
Each atom of Silicon is bound to its four nearest neighbors with covalent chemical bonds, sharing 4 of its valence electrons [10]. Silicon crystal lattice is schematized in Figure 2.1.

Using statistical mechanics, can be defined different electrons' energy levels for the crystalline structure. Pairing between valence electrons produces a band of energy levels very close together. In silicon lattice, and all other semiconductors as in Figure 2.2, two energy bands can be distinguished: The Conduction band and the Valence band.

In the valence band electrons are tightly bound in covalent bonds between atoms, while in the conduction band electrons are free to move and can conduct electrical current. These two bands are separated by an energy prohibited gap. As the excitation energy increases, the gap becomes smaller and bands wider. At ambient temperature ($\sim 300K$) electron-holes density in Silicon is about $10^{10} cm^{-3}$ corresponding to a resistivity of about $350\, K\Omega\, cm$. The energy gap under these conditions is 1.115 eV.

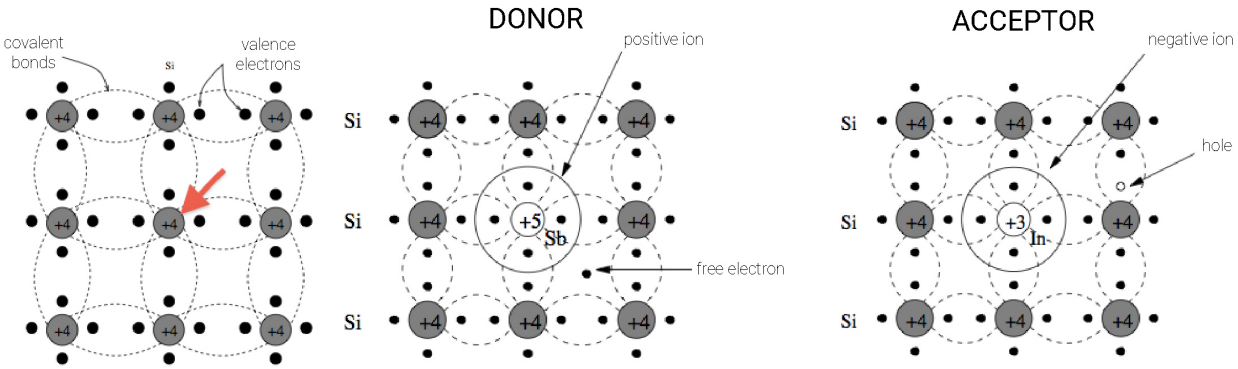

Figure 2.1: Scheme of Silicon tetrahedral lattice structure in which each element shares 4 valence electrons (left). Silicon semiconductor doped with atoms of Sb, donor of the Vth group (center). Silicon semiconductor doped with atoms of In, acceptor of III group (right)

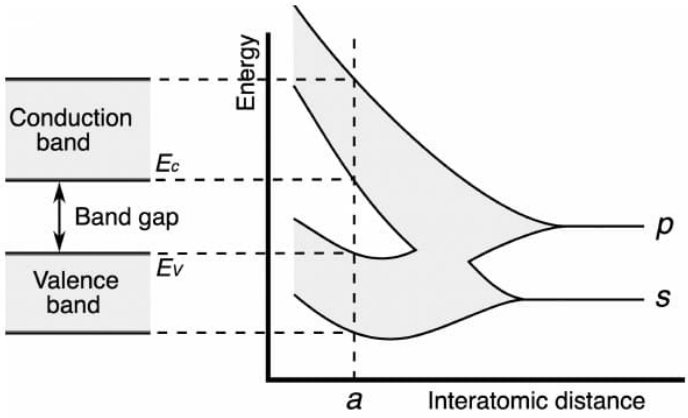

Figure 2.2: Diagram of bands structure for semiconductors at low inter-atomic distances

It is possible to reduce the energy gap by 'creating' new energy levels that are allowed and discrete inside the gap, by doping, substituting some of the atoms in the semiconductors lattice, with other elements. This process can be seen in Figure 2.3.

The elements of Group V, like Phosphorus (P) or Arsenic (As), have five valence electrons, these atoms can easily lose the excess electron to the conduction band becoming **donors**. Donors give rise to the electronic type of conductivity, forming a **N-region**. In contrast, group III elements lack one valence electron, which they can easily capture from the lattice, giving rise to a mobile hole in the valence band, becoming **acceptors**. After capturing one electron the impurity center becomes negatively charged while a hole appears in the valence band generating conductivity by holes and a **P-region** [10].

A **P-N junction** is formed bringing together the two types of drugged semiconductors. The diodes in which silicon detectors usually consist are based on p-n junctions. In the interface between the two drugged semiconductors is created a concentration gradient between the primary charge carriers of the two regions. This charge carrier density causes a diffusion current of electrons moving towards the p side and holes to the n side. In this region, called *depletion region*, the mobile charges recombine. As a consequence of this process, the depletion region in the n-region becomes positively charged due to the loss of electrons and vice versa the one in the p-region becomes negative, giving rise to

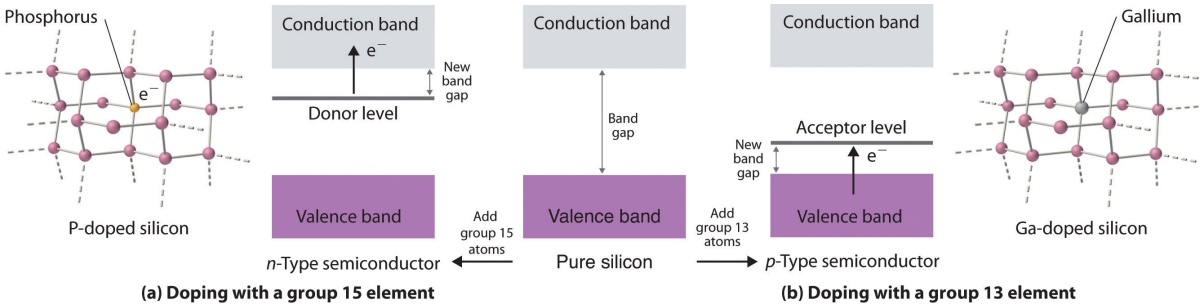

Figure 2.3: Diagram of bands structure for doped semiconductors with donor (left) and acceptor (right) elements.

an internal electric field. This one opposes the diffusion motion until an equilibrium is reached and the charged carrier flow stops. p-n junctions are schematized in Figure2.4.

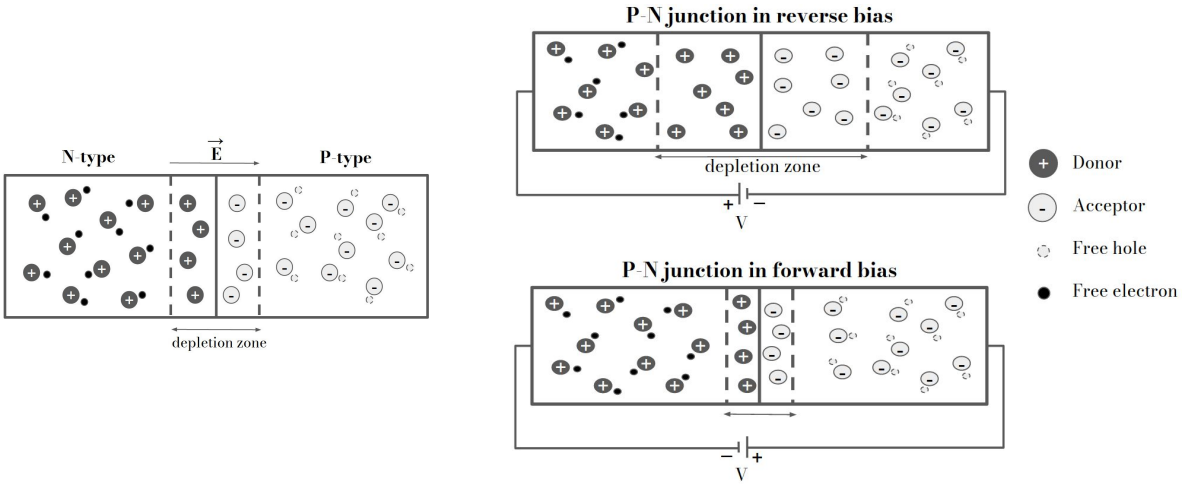

Figure 2.4: Scheme of a p-n junction (left) in reverse (upper right) and forward bias (bottom right) with their respective depletion regions.

To increase or decrease the width of the depleted zone an external voltage can be applied, thus a p-n junction can operate in two different regimes, shown in Figure 2.4. Forward bias is realized by connecting the p-region to the positive electrode and the n-region to the negative one, which generates a narrower depletion region. Conversely **Reverse bias** has p-region attached to the negative electrode, which causes the junction to behave as an open switch. In this configuration, the width of the depletion region increases as the barrier potential increases in correspondence to the junction, opposing the primary charges flow. In reverse bias a smaller reverse current flows through the diode and the passage of the particle produces a higher number of carriers, this is why Silicon detectors operate in reverse bias. Therefore, when a particle occurs through the detector generating an electron-hole pair with its energy, due to the depletion region's electric field, the electron-hole pairs eventually travel to the electrodes generating a measurable current.

Silicon Photodiodes The equilibrium between the electric field and charge drift can be broken by either thermal agitation or photoelectric effect. When a photon interacts with the detector structure hitting the junction of a diode, if its energy is greater than the one of the gap, it will break a covalent bond creating an electron-hole pair. Applying a reverse bias to a photodiode sets up the electric field across the depletion region that

will prevent its recombination causing these charge carriers to be accelerated towards the anode (holes) or the cathode (electrons). Therefore, an absorbed photon results in a net flow of current that can be measured [11]. The signal persists until all of the charge carriers generated by the process reach their corresponding collection electrode. Silicon detectors of 300 μm are usually crossed by electrons in $\sim$ 10 ns and by holes in $\sim$ 25 ns.

2.1.2 The SiPM

A Silicon PhotoMultiplier (SiPM) is a matrix of independent microcells on a common silicon substrate, consisting in a repeated combination of an avalanche photodiode (SPAD) and a quenching circuit. All of the microcells have identical size, are connected in parallel and are arranged in a rectangular pattern. SiPMs have spectral sensitivities from UV to IR, peaking in the visible (270 nm - 900 nm)[11]. The SiPMs utilized in this study, shown in Figure 2.5, are Hamamatsu S13360-3050/3075. These devices are characterized by 50 and 75 μm pixel pitch with an effective photosensitive area of 3 x 3 mm and a total of 3600 and 1600 pixels [12].

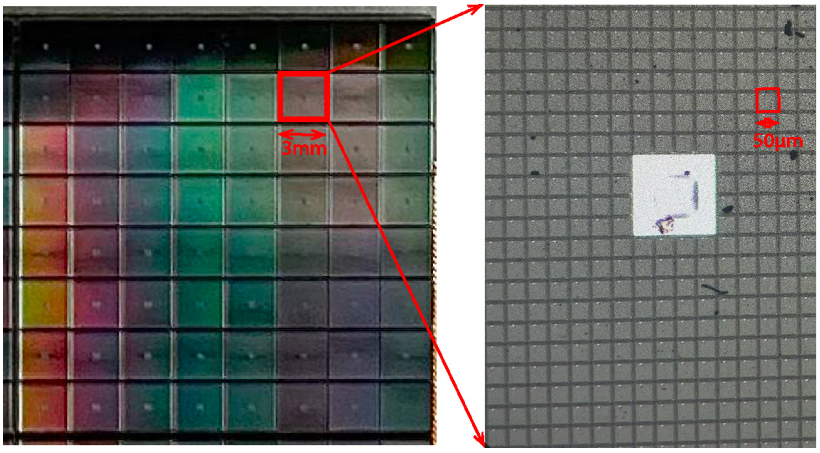

Figure 2.5: Structure of the Hamamatsu S13360-3050 and 3075 SiPMs. With an enlargement on the single SPAD.

SPAD and quenching circuit In a SiPM each Single Photon Avalanche Diode (SPAD) is connected to its own quenching resistor, as illustrated in Figure 2.6.

The SPADs are photodiodes that consent single-photon detection resolution. If the depletion region of the SPADs is subjected to a sufficiently high electric field, when a microcell absorbs a photon and a charge carrier is generated, the latter gains enough energy to create a new electron-hole pair. This process is called *impact ionization* and gives rise to a self-sustaining avalanche process, resulting in a current flow through the microcell, a process called *Geiger discharge*. The Geiger discharge happens when the diode is reverse-biased with a voltage above a breakdown threshold. Thus, this technology is utilized in SiPMs that operate above the breakdown voltage. Indeed, in order to reach the high electric field, to the diode is applied a reverse bias voltage greater than the nominal breakdown voltage of the diode. The generated flow of current is then stopped only by lowering the voltage of the diode. This is the purpose of the quenching circuit. The latter is formed by a parasitic capacitance (C_q) in parallel with the quenching resistor (R_q). The generated current inside the SPAD triggers the action of the quenching resistor, which quenches the avalanche as just explained. Then the diode returns to the nominal value of the bias voltage, being newly able to detect photons in a time called *recovery*

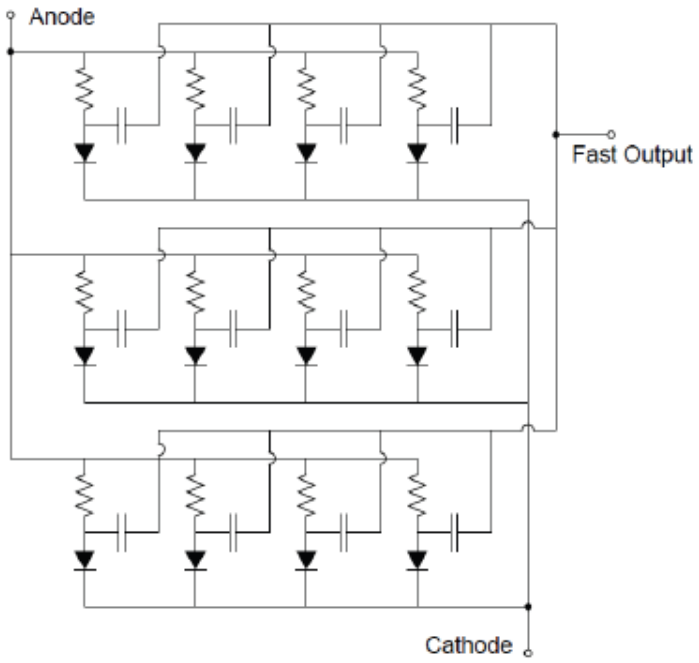

Figure 2.6: Schematic circuit of an SiPM consisting in an array of photodiodes and quenching resistors [11].

time. The process of this photon-triggered switch is represented in Figure 2.7. Typically, the recommended operating bias voltage in SiPM is a few volts ($\sim 3\ V$ in the Hamamatsu sensors considered in this work) above the breakdown. This value can be expressed as the over voltage (see Paragraph 2.1.3). It has to be noted that the breakdown voltage has a temperature dependence and decreases with decreasing temperature. Therefore for stable operation of the SiPM, either the temperature must be stabilized or the bias voltage must be changed with changing temperature.
The process just described is limited to the single struck microcell, while other microcells are ready to detect photons in the meantime. Due to the parallel connection the generated signal will depend on how many SPADs are activated. It is not possible to distinguish whether the single SPAD is simultaneously hit by several photons.

SiPM output pulse and Recovery Time A typical SiPM output pulse is shown in Figure 2.8. It presents a steep rise, and its characteristic time is determined by the avalanche formation, linked to the incident wavelength of the photon, by the variation of transit time of the signal generated in different sites of the sensor, and especially by Geiger discharge through the capacitance C_q of the quench circuit.

The recovery time in which the cell returns to its initial condition is the decay time of the pulse and depends on the microcell recharge time constant τ_{RC}, given by:

$$\tau_{RC} = C_d(R_q + N \cdot R_s) \tag{2.1}$$

Where R_s is any resistance in series with the sensor and N is the number of the microcells. The capacitance C_d depends on the size of the cells, wider cells have longer recovery time. The considered cells have $C_d = 320\ pF$ [12].

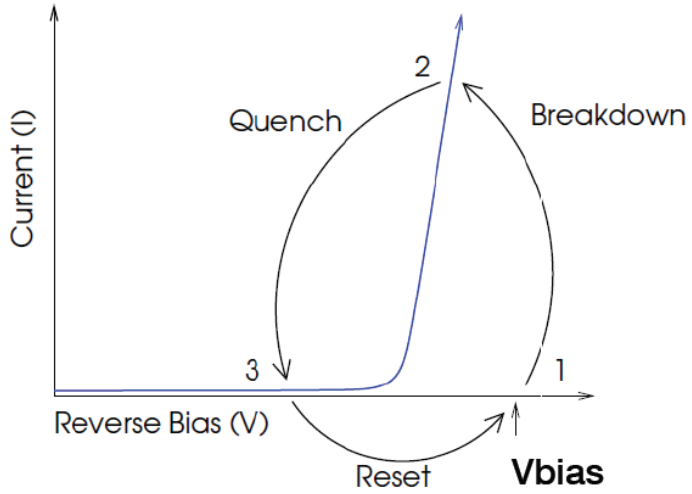

Figure 2.7: Plot of current as a function of applied voltage, with a highlight on the breakdown, quench and reset cycle of the SPAD. [13]

2.1.3 Performance parameters

Breakdown voltage and gain The *breakdown voltage* (V_{bd}) is defined by the p-n junction characteristics of the SiPM technology and is the minimum reverse bias voltage that leads to Geiger avalanche multiplication. The SiPMs operate, as said before, at a higher bias (V_{bias}) than V_{bd}. The difference between the bias voltage value and the breakdown point is called *overvoltage*. The overvoltage can be defined as follows:

$$V_{ov} = V_{bias} - V_{bd} \tag{2.2}$$

The extent of the increase of the drifting carriers population after the impact ionization, thus the difference between the original photo-carrier count and the final charge signal collected is the *gain* (G) of the avalanche process. G is a function of overvoltage and of the microcell size:

$$G = \frac{C_d \cdot V_{ov}}{q} \tag{2.3}$$

where q is the elementary charge. The microcell can still acquire a pulse during the recovery time but the gain will be reduced in proportion with the reduced overvoltage, see Figure 2.9.
The acquisition rate of successive photons in the prototype depends also on the threshold set on the discriminator of the electronics and is about 20-25 ns.

Fill Factor The total area occupied by the microcells is the active area. Certain regions of the sensor have no photosensibility since for electrical and optical isolation the cells must be separated. Also, the resistor occupies some of the area. The percentage of the active area sensitive to light is known as *fill factor* (F). For Hamamatzu S13360-3050 and 3075 SiPMs the fill factor is respectively 74% and 82%. The larger the cells are the higher the fill factor is, this point influences the gain parameters and the efficiency of the SiPM.

Photon detection efficiency A measure of the sensitivity of the SiPM is the Photon Detection Efficiency (PDE), which is defined as the ratio between the detected photons

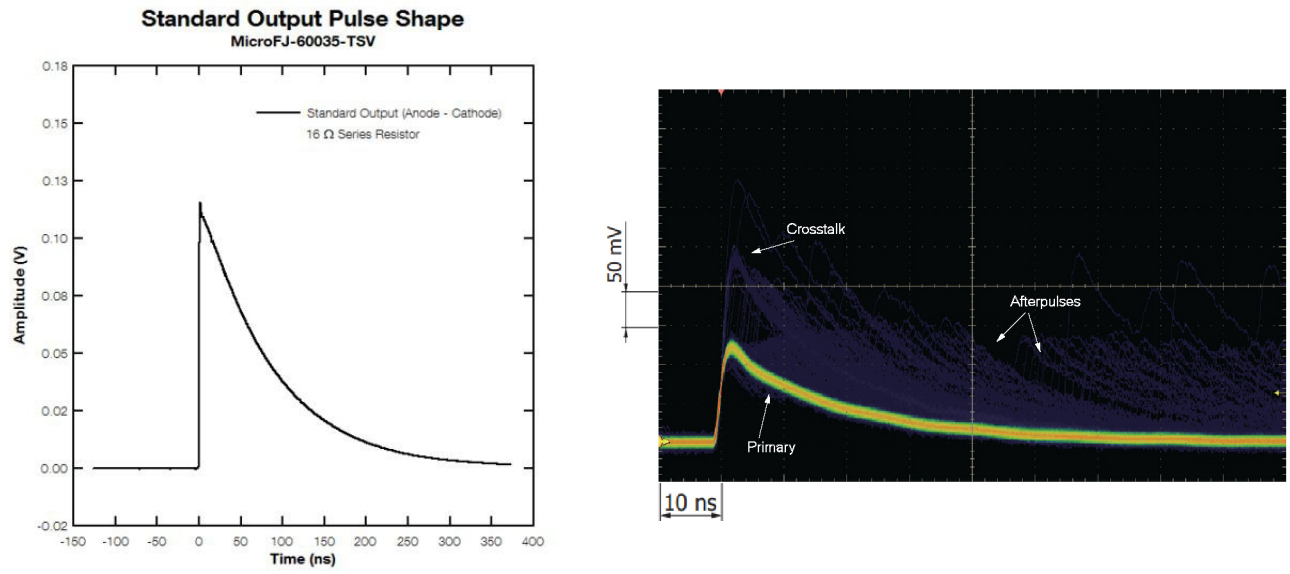

Figure 2.8: Output pulse showing the recovery time of the cell (left), typical output pulse of Hamamatzu S13360-3050 SiPM with highlight oh afterpulse (right)[12].

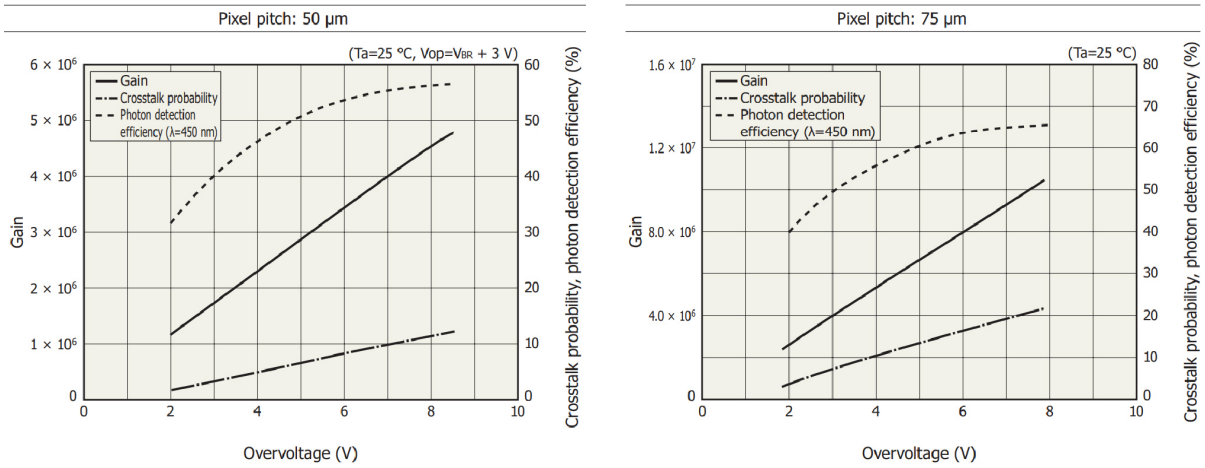

Figure 2.9: Gain, crosstalk probability and photon detection efficiency as a function of the overvoltage for 50 μm (left) and 75 μm (right) microcells [12].

of wavelength λ with the actual number of photons striking the detector. It represents a statistical probability for an impinging photon of producing an avalanche inside the stuck microcell, thus of producing a detectable signal. The PDE depends on the wavelength of the incident photon, on the overvoltage and on the fill factor through the functional relation:

$$PDE(V_{ov}, \lambda) = QE(\lambda) \cdot P_T(V_{ov}, \lambda) \cdot F(V_{ov}, \lambda) \tag{2.4}$$

Where the variable QE is the *quantum efficiency*, which is the probability for the incident photon to create an initial electron-hole pair in the active volume and the P_T is the avalanche triggering probability. Both of them depend on the wavelength, the inherited dependence of PDE on λ for the specific SiPMs used in this study is plotted in Figure 2.10

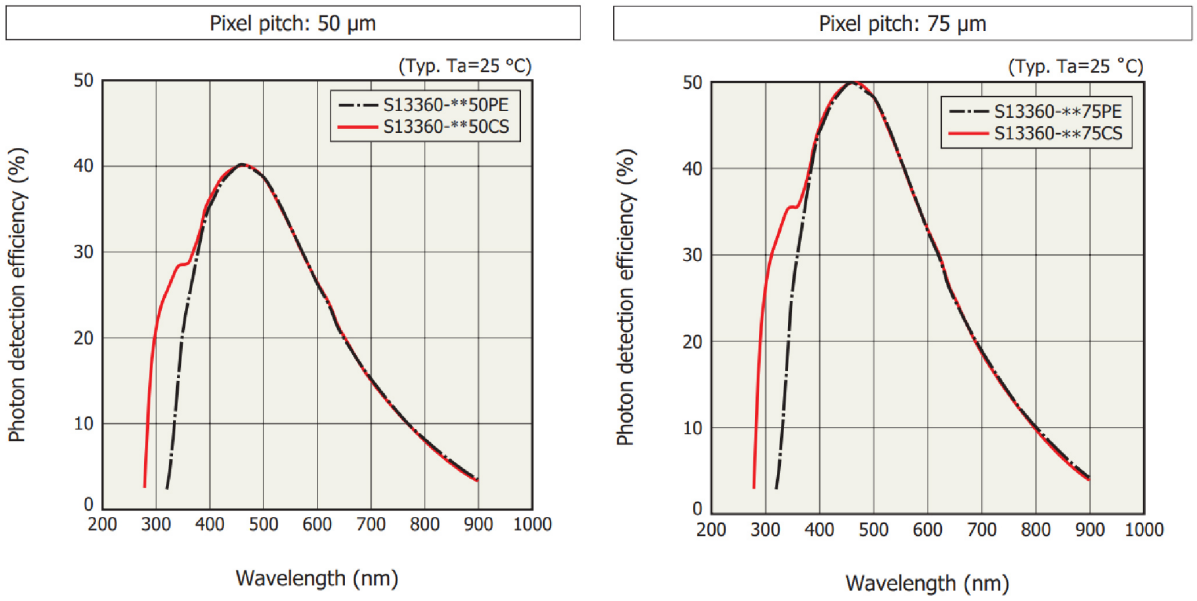

Figure 2.10: Photon detection efficiency as a function of the incident light wavelength for 50 μm (left) and 75μm (right) microcells [12].

2.1.4 Noise

There are two main types of noise in SiPMs: *primary* and *secondary* (or correlated). The main source of primary noise is the Dark Count Rate (DCR) and consists of avalanche pulses triggered thermally. These effects depend on the quality of the silicon, the volume of the depletion region, the fill factor and mostly temperature.
Correlated noises are subsequent noise events. In this case, the avalanche pulse is generated because of the primary event. These are mainly *afterpulses* in the same cell and *crosstalk* effects in nearby cells of the same array of SPADs.

Dark count rate The DC rates are false signals caused by charge carriers generated thermally or due to the tunneling in the high field of the p-n junction in the bulk, that triggers avalanche pulses. When these electrons give rise to an avalanche, it results in nothing different from the one that would result from photon absorption. Thus, DCRs are random and always present in the acquisition process, regardless of SiPM's light conditions and illumination level. The DCR depends strongly on temperature (it decreases by approximately a factor 2 every 10 K temperature drop), on the overvoltage and is affected by radiation damage. Actively cooling the sensor can significantly reduce DCR, as plotted in Figure 3.10. To keep the DCR at acceptable levels, below $\sim 100\,kHz/mm^2$, data acquisition for the dRICH prototype is held at $-40°$. Is expected a DCR of 300 kHz/ch at maximum SiPM damage before performing an *annealing cycle*, a procedure defined in 2.1.5 [14]. It is possible to reduce DCR noise for single photon detection by setting a threshold above the single photon level. However, in dRICH detector and other applications that need single photon sensibility this procedure cannot be used, so this noise source will still contribute to the obtained signal.

Optical crosstalk and aferpulse A secondary form of noise is crosstalk between neighbouring SPADs. When an avalanche occurs in a SPAD, it can generate up to $3 \cdot 10^{-5}$ photons per charge carrier, with wavelength in the infrared region [2]. These isotropically

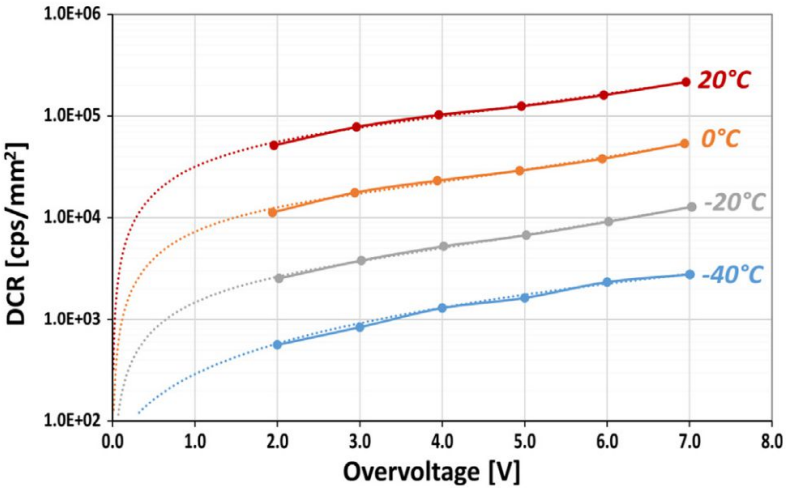

Figure 2.11: Measured DCR of a SiPM per unit area as a function of overvoltage for different temperatures [15].

generated photons can trigger a different avalanche in the nearby SPADs within the SiPM array. More SPADs can then see the generated current, acquiring a signal corresponding to two or more photons, even if only one single photon hit one SPAD. This phenomenon increases with overvoltage due to the amount of charges that cross the junction in a SPAD, so it can be minimized using low-gain SPADs consequently reducing secondary photon production.
Another form of secondary noise is the *afterpulse*, which is a delayed pulse signal made of a spurious avalanche generated by the release of carriers that remained trapped in a defect of the sensor silicon crystal. Its amplitude is usually lower than the one of the primary pulse and its probability depends on the number of incident photons and release time of the traps, with respect to the recovery time of the SPAD. If the latter is long compared to the delay, the afterpulse can be overlooked, otherwise, if the rate is high it can impact the measurements. Thus, the afterpulse can be reduced by adjusting SiPM's recovery time or minimizing the defects in the sensor's silicon. Afterpulse can also take the form of a prompt optical crosstalk, due to the absorption of secondary photons from the same SPAD, triggering again an avalanche. This ones can be solved by inserting an inverted-doping substrate which originates a junction that blocks all secondary generated charge from diffusing. Crosstalk and afterpulse effects can be seen in Figure 2.8 (right).

2.1.5 Radiation damage and annealing

Silicon sensors suffer from the radiation damage originated by particles traveling through them. There are two types of damage: bulk damage from non-ionizing energy loss (NIEL) and surface damage from ionizing energy loss (IEL, energies $< 300\ keV$)[16]. Both increase the dark current[1] and consequently the dark count rate. In the NIEL case, the passage of high energy neutral particles, as neutrons, can displace atoms in the crystal lattice generating cluster defects. In IEL, radiation produces electron-hole pairs of which electrons can leave the crystal, while holes remain creating interface traps in the junction

[1]The dark current (DC) is formed by thermally generated charge carriers inside the silicon. Increasing the depth of the depletion region leads to an increase in the sensitivity of the photodiode toward longer wavelengths, but so does also in the ability to collect thermally generated carriers forming the dark current. So hypersensitive detectors suffer from high DC.

and surface current in an electric field. SiPM performance can be restored by thermal annealing[2] which can also be electrically induced both in forward or reverse bias taking advantage of an intense electric field. The paths of recovery are shown in Figure 2.12

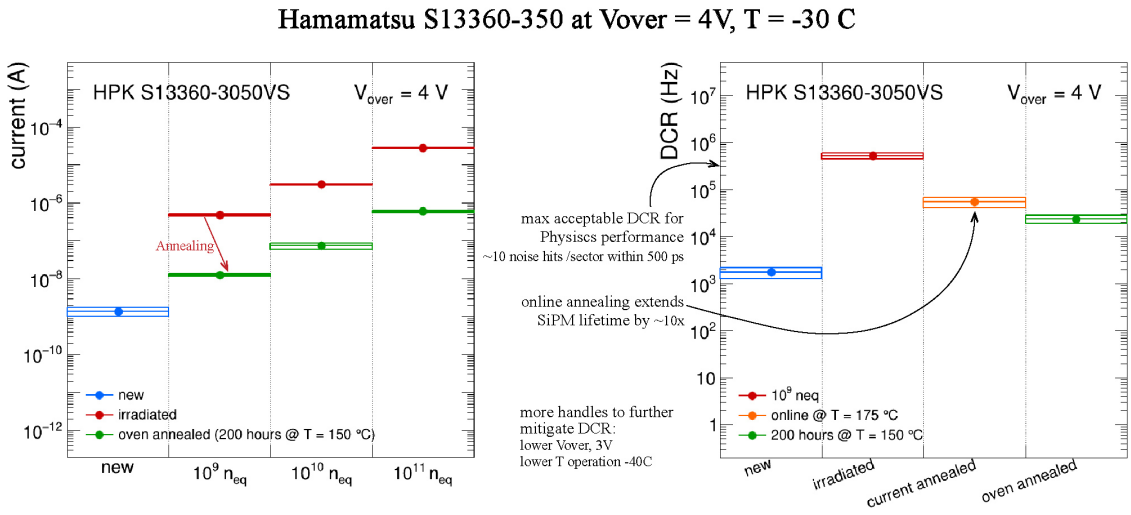

Figure 2.12: Silicon detector's recovery statistics in both oven and online annealing. Forward bias for current annealing results more effective. The latter results in 25% efficiency loss, whereas with oven annealing there is none [8].

2.2 Peltier modules

Peltier modules are thermoelectric devices used to cool down objects or to maintain them in a steady temperature. These systems have been used to cool down SiPM at $-40°$ during the data acquisition inside the dRICH detector prototype. The Peltier modules are based on the thermoelectric Peltier effect, discussed in Section 2.2.1. The structure of the Peltier modules used in the detector is described in Section 2.2.2. These types of devices are also employed in other fields to generate electric current[3].

2.2.1 Peltier effect

The Peltier effect is a thermoelectric phenomenon in which the passage of an electric current, generated by a potential difference through the two materials forming a thermocouple, causes the two junctions to reach different temperatures [17]. Since one junction absorbs and the other releases thermal energy, the one that releases heat can be used to cool down a region or an object by placing the hot junction outside the concerned area, as shown in Figure 2.13. The reverse process can be done by changing the direction of the current flow, inverting the potential difference sign. This method allows us to cool down materials without the use of circulating fluids, which are only used to dissipate the heat transferred in the hot junction.

[2]Interstitial and clusters generated by displaced atoms are very mobile at high temperature, above 150 K those can annihilate curing the defects.

[3]If the two surfaces are at different temperatures, a voltage is generated. Such uses are common in space applications, where a thermal generator (made of radioactive material) heats one side while the other side remains cool.

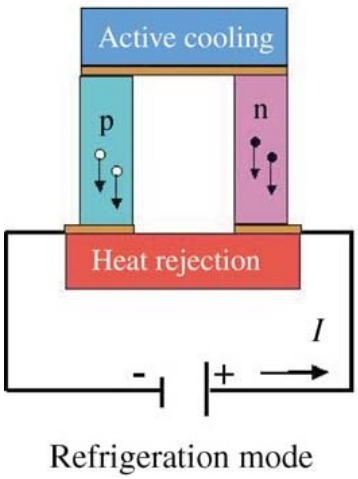

Figure 2.13: Diagram of a thermoelectric couple composed of an n-type and a p-type semiconductor, used as a cooler based on Peltier Effect [17].

2.2.2 Thermoelectric cooler

The thermoelectric cooler used in the sensors of dRICH prototype is made up of the elements listed below [18]:

- Thermoelectric Cooling (TEC) Controller ;
- Peltier element;
- heat sink based on circulating water, to dissipate the heat on the hot side of the Peltier modulus;
- a software to configure and monitor the TEC controller;
- a power supply system.

For the prototype construction have been used TEC that are directly connected to the power supply to provide the current for the modules. Afterward, the system is connected to a software that directly monitors the power supply and the temperature of the NTCs. The Peltier modules comprise Bismuth Telluride (Bi_2Te_3) semiconductor pellets connected thermally in parallel and electrically in series with a Thermoelectric Cooling (TEC) Controller. These pellets are alternately doped so that charge carriers that give rise to the principal current are either positive or negative. The upper and bottom bases for the pellets and the conductive tabs are made of ceramic for electrical insulation whereas the electrical interconnect that holds the semiconductor elements is made of copper, as illustrated in Figure 2.14.

The water base cooling is placed in touch with the hot side of the Peltier elements to dissipate the heat produced and transferred inside the Peltier element douring heat pumping. The structure is combined with a power supply, which provides the current for the Peltier unit, regulating its temperature by providing the thermoelectric element with the right amount of current. In the Peltier operations, for the TEC there is a current limit I_{max} after which the temperature rises again due to the dissipation of power. The current level used in the test done for this thesis, most widely described in section 3.2.6, is $\sim 1A$ with a voltage of $\sim 2V$, far below the threshold.

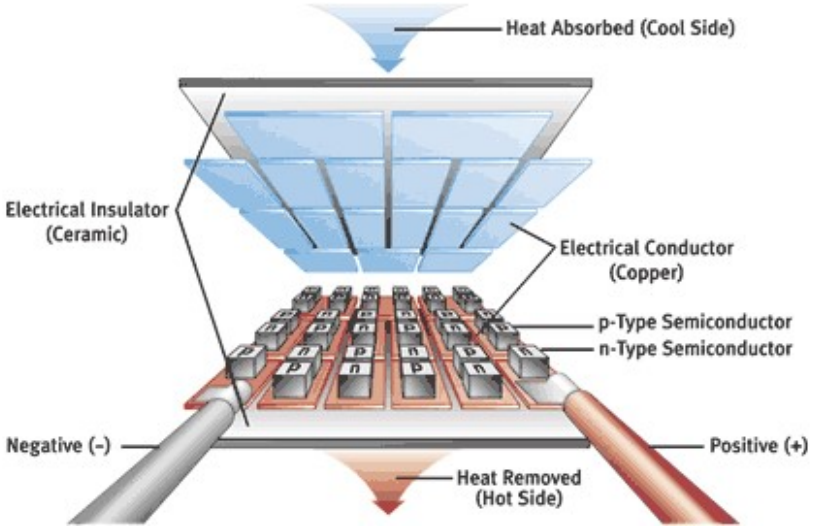

Figure 2.14: Diagram of a typical Thermoelectric System made of Peltier modulus.

2.3 Data analysis and timing: ALCOR-V2 ASIC

For the readout and digitalization of the dRICH SiPMs signals the board ALCOR (A Low-power Chip for Optical Readout) has been chosen. ALCOR is a mixed-signal Application Specific Integrated Circuit (ASIC) that is designed to read SiPMs signals at cryogenic temperatures. The full chip area is $4.95 \times 3.78\ mm^2$ and its core consists of 32 parallel channels arranged in an 8 x 4 pixel matrix structure, shown in the top level layout in Figure 2.15. It can be configured to operate in Single photon counting (as used in this study) and allows also operation in Time-over-Threshold (ToT) mode. Each pixel has dimensions approximately of $440\ \mu m \times 440\ \mu m$, is designed in a $110\ nm$ CMOS technology and the power consumption is $\sim 10 - 12\,mW$ per channel [19]. Each one is designed with a dual-polarity front end, with the Regulated Common Gate (RCG) framework, providing a low input impedance. The RCG enables the reading of both anode or cathode signals and provides communication between sensors and other elements. However, the dRICH SiPMs will operate with signal readout via anode.

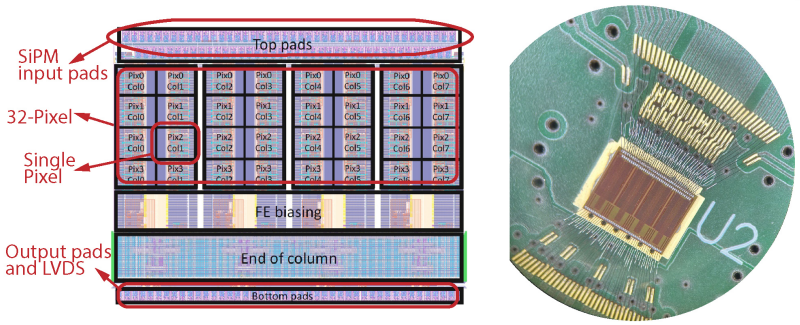

Figure 2.15: Diagram (left) and microscope image (right) of the top level layout view of the ALCOR chip.

The analog and the digital parts are placed in different regions to minimize crosstalk, thus adjacent readout pixels are mirror-assembled. Analog inputs are on top whereas digital outputs are at the bottom.
The front end contains two independent trans-impedance amplifier (TIA) branches, each

connected to a leading-edge discriminator [14]. After the input phase, the signal passes through the two amplifiers with independent programmable gain and shaping time. The two leading-edge discriminators have a 6-bit DAC programmable threshold that can be set to a desired voltage. When it is surpassed by the rising edge of the analog pulse, the comparator generates a logical pulse, as reported in Figure 2.16. Thus the chip includes amplification, conditioning and digitalization of the signal, with a fully digital output. Figure 2.17(b) shows the ALCOR DUAL board developed for the dRICH SiPM prototype to host 2 ALCOR chips.

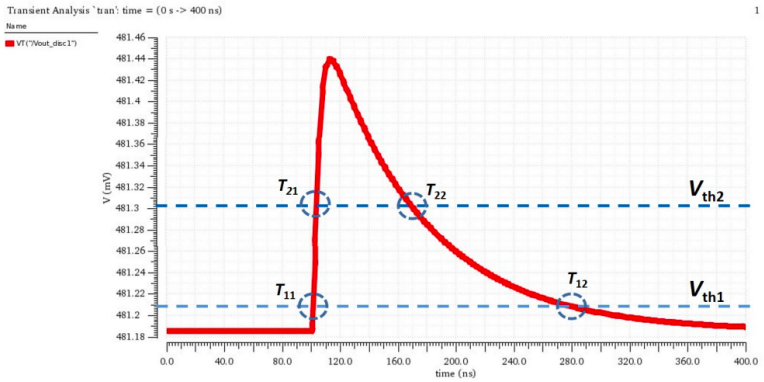

Figure 2.16: Chart of dual threshold voltages. T_{11} is the leading edge timing, V_{th1} is a lower threshold, fixed to take advantage of the faster signal slope and V_{th2} is the set desired threshold voltage for detection.

Afterwards, the discriminator generates the trigger CMOS signals that are provided to the channel digital control block.
For each signal, the timing information is derived from a binary 15-bit counter and from a 9-bit fine part generated by time-to-digital converter (TDC). The clock frequency and the bin size determine the dead time of the TDC, which is 150 ns for a clock of 350 MHz and a time-bin size of 50 ps [14]. Thereby, when a photon is detected a pixel generates a 32-bit word containing information about the column and pixel position tag, TDC address, coarse and fine counter. Data from each pixel are collected and transmitted in the periphery of the chip by the End-of-Column (EoC) that acts as an interface between the channels and the outside facilities. Via LVDS (Low-Voltage Differential Signaling) drivers, data is finally transmitted off-chip, with a maximum transmission speed of 640 $Mbit/s$ [14]. The operation mode of the pixel and the front-end can be configured by a FPGA, shown in Figure 2.17 (c).

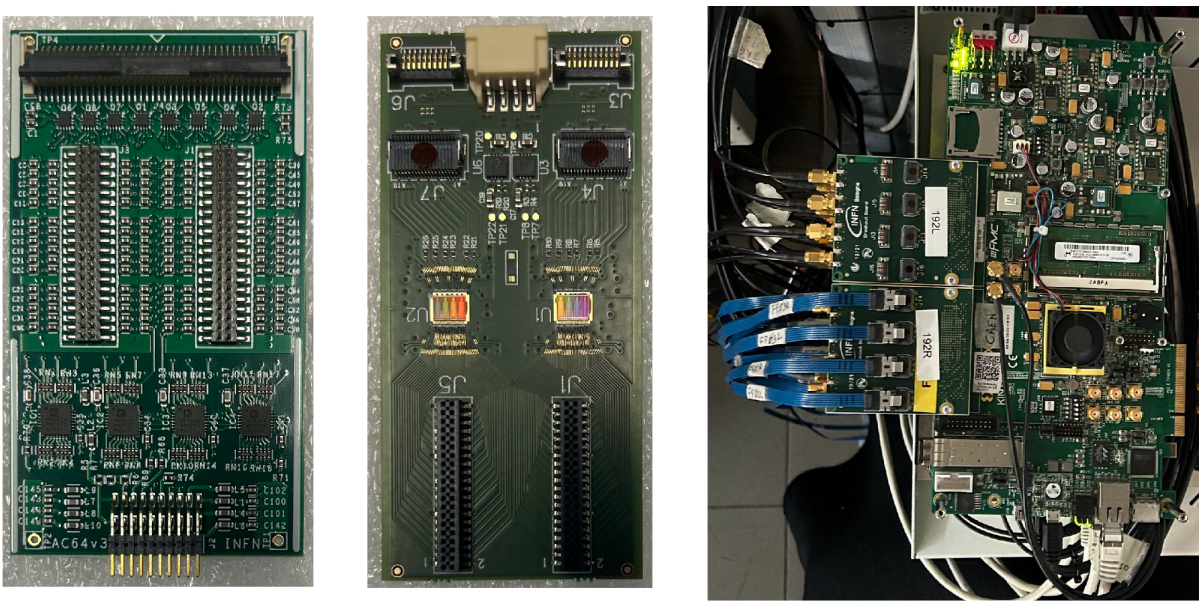

(a) Front (b) Back (c) FPGA

Figure 2.17: Images of both sides of ALCOR DUO board (a,b) and the connection with the FPGA (c) used in the experimental set-up of this study.

Chapter 3

The dRICH SiPM prototype

The subject of this study is the tests and the construction of the dRICH SiPM-based photodetector prototype readout for the Test Beam conducted in May 2024.
The prototype setup and its components are discussed in Section 3.1. Section 3.2 focuses on the tests and the characterization that we performed on the listed components. SiPM sensors for single photon detection and NTC temperature sensors tests are reported in Section 3.2.2, along with the test based on the DCR of the SiPMs. To maintain a steady temperature of the SiPMs in the prototype readout box throughout the beam test SiPM carriers are coupled with a stack of Peltier cells, whose test is reported in Section 3.2.6. The construction phase, the final assembly and organization of the prototype are described in Section 3.3, while the test beam results are briefly set out in Section 3.4.

3.1 Experimental equipment and setup

The dRICH prototype provides particle identification exploiting the Cherenkov light produced by charged particles through aerogel and perfluorocarbon radiator gas (C_2F_6), used to cover the full momentum range. The beam test purpose is to analyze the performance of SiPM sensors for particle identification at EIC, proving their capability to detect single photons, produced through the Cherenkov effect, while keeping DCR at low levels despite radiation damage of the SiPMs. A scheme of the dRICH prototype facility is reported in Figure 3.1. The experimental setup of the prototype consists in two main parts, the gas chamber and the detector box.
The gas chamber is made of two concentric cylinders with a different radius placed in sequence. It contains the dRICH, placed upstream, and sustains the two spherical mirrors allowing them to change their angle and position along the detector. The mirrors are based at the opposite side of SiPM sensors to align and focus the incoming Cherenkov radiation onto the sensor array. To introduce the gas C_2F_6 the chamber withstands over and under pressurization. A charged particle of the beam initially passes through the aerogel ($n = 1.02$) producing a cone of Cherenkov photons of ~ 11 degrees aperture which is reflected back and focused onto the SiPM plane by the first spherical mirror. The latter has an inner hole to allow the passage of particles into the gas that fills the chamber (n= 1.00085), producing another Cherenkov cone of ~ 2 degrees aperture. This one is reflected back by the second mirror into the photon detector [20]. The information obtained by the SiPMs of the two Cherenkov radiations combined with the known beam momentum will allow pions, kaons and protons identification.

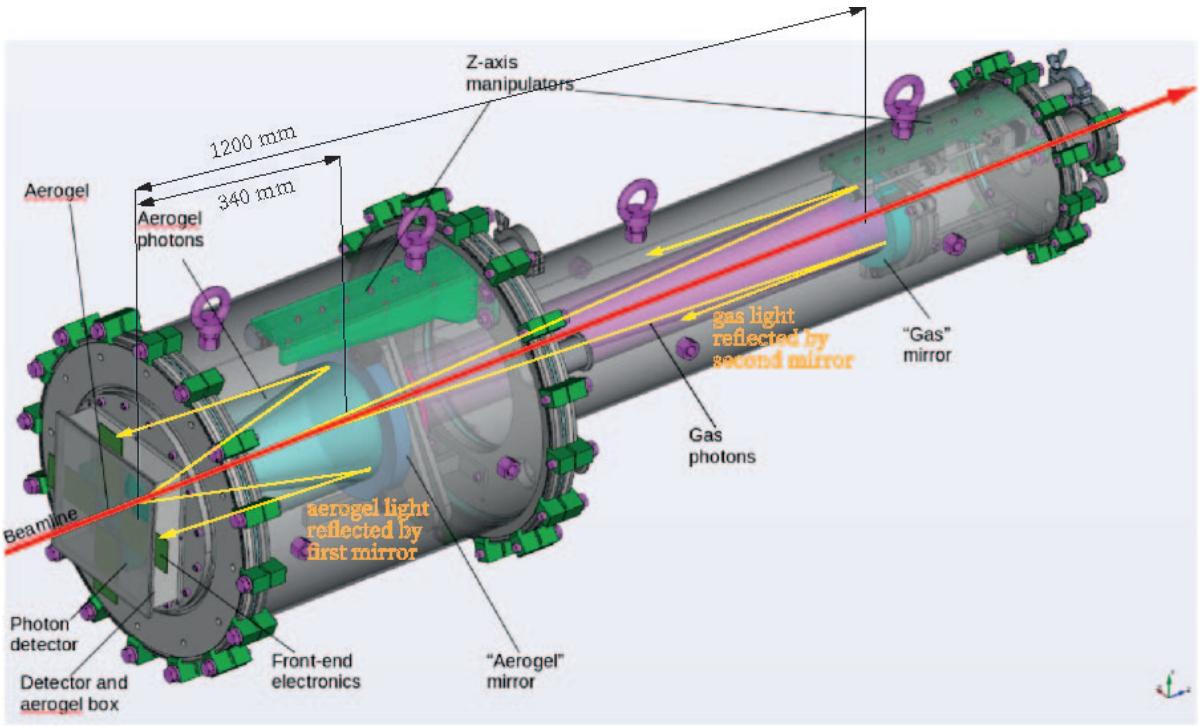

Figure 3.1: dRICH detector prototype [20].

3.1.1 Prototype EIC readout with thermoelectric cooling

The prototype developed for the test beam in this study consists in the detector box, containing the elements for the cooling and data acquisition. The detector box houses the aerogel box in a N_2 dry atmosphere, sustains the photon detector and the front-end electronics and supports the thermoelectric cooling system for the SiPM matrices.

The devices employed in the prototype integration includes a large area readout plane based on a total of 2048-channels $3 \times 3\ mm^2$ SiPM sensors. The modular sensor is made of EIC-driven prototype photodetector units (PDU) each integrating 256 SiPM pixel sensors, cooling and TDC electronics in a volume of $5 \times 5 \times 14\ cm^3$ [21]. The prototype box includes:

- 8 **carrier boards** each one hosting 4 **SiPM matrixes** for a total of 256 channels; Situated in the 8 sections of the box to keep in place the SiPM detectors for Cherenkov imaging. Each matrix consists of 8 x 8 arrays of $3 \times 3\ mm^2$ SiPMs [22].
- 2 **Peltier cells** for each carrier board;
  placed in contact with the carrier boards on their back side inside the box. The carrier boards along with the SiPM are cooled down to $-30°C$. The Peltier keep them at this fixed temperature for the whole test process.
- A **cooling block** for each PDU;
  Water circulating system to dissipate the heat that is transferred in the hot side of the Peltier modules away from the sensors.
- 4 **ALCOR DUAL** front-end electronic boards for each PDU;
  Each matrix of the 4 situated on the carrier board is connected to an ALCOR DUAL front-end card on which two ALCOR chips are situated, each one with 32 channels.

- 4 Adapter boards;
  The adapter boards adapt the SiPM carrier board connector to ALCOR. They also regulate through electronic circuits the V_{bias} value supplied to the SiPMs.

- A digital output humidity and temperature sensor with Arduino.

The SiPM used for this setup are two different types Hamamatsu S13360-3050 and Hamamatsu S13360-3075, whose characteristics are reported in Table 3.1:

Type name	S13360-3050VS	S13360-3075VS
Pixel Pitch (μm)	50	75
Active area (mm)	3.0 $\times$ 3.0	3.0 $\times$ 3.0
Number of SPADs	3600	1600
Fill Factor (%)	74	82
Resin	Silicon	Silicon
Spectral response range λ	270 to 900	270 to 900
Photon detection efficiency PDE[1] $\lambda = \lambda_p$ (%)	40	50
Dark count[2] (kcps)	500/max1500	500/max1500
Terminal Capacitance C_t (pF)	320	320
Gain M	1.7 $\times$ 10^6	4.0 $\times$ 10^6
Breakdown voltage V_{BR} (V)	53 $\pm$ 5	53 $\pm$ 5

Table 3.1: Main features of Hamamatsu SiPM models used for the setup. Values valid at 25°C [12].

Outside of the box, the setup consists of:

- A **Master Logic** board for each adapter board (32 boards in total);
  Master logic boards are responsible for communication with circuits on the adapter boards and are connected to them through a flat cable. The master logic boards, shown in Figure 3.2(a) are then connected to the power supply system that provides the bias voltage for the SiPMs. Two 32 V channels from the power supply have been connected in series to define the 64 V input voltage. The control of the Master Logic boards is performed via a Linux computer through a USB cable implementing the RS-485 serial communication protocol.

- 12 **FPGA** KG705 Xilinx Evaluation Boards;
  The Field-Programmable Gate Array (FPGA) platforms program and read data from ALCOR, with whom are connected through SAMTEC Firefly cables, as shown in Figure3.2(b). The FPGAs are in turn connected to their power-supply cables, to the computer through which are programmed and to the clock generator boards that provide a synchronized clock (320 MHz) to the whole system [23].

- A computer-controlled CAEN power supply system based on a SY5527 main frame with several low-voltage modules was used to bring power to the front-end boards, to the Peltier elements and bring the high voltage to the sensors.

[1]Photon Detection Efficiency does not include crosstalk or afterpulses
[2]Threshold = 0.5p.e.

- A refrigerated circulator HAAKE PHOENIX II C41P. A water cooling system for the Peltier modules inside the box.

In order to monitor the conditions and to operate the elements inside the box the web application **Grafana** has been used [24]. In the operational pannel, several programmable buttons are available in order to start and stop measurements, turn on and off the power supply, monitor and change temperature, and be informed about the overall state of the setup components.

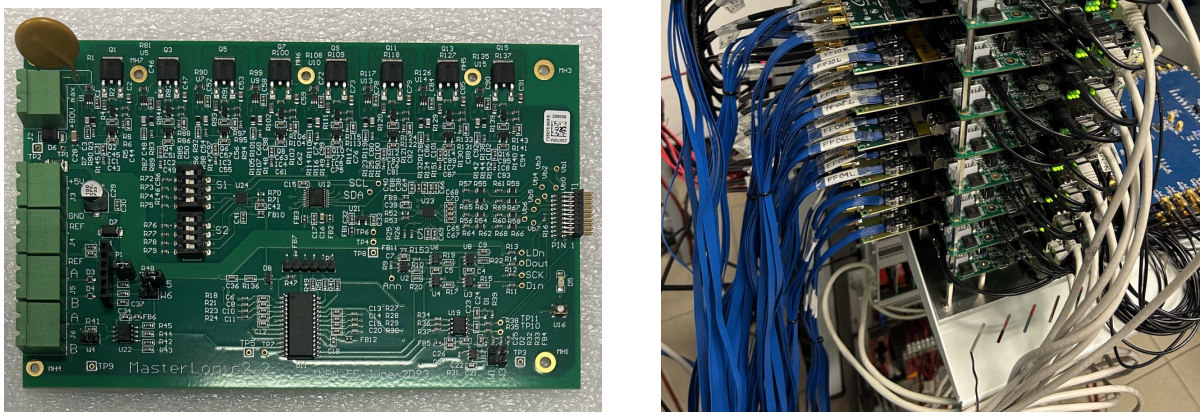

(a) (b)

Figure 3.2: Image of a Master Logic board (a) and of FPGAs (b) positioned one upon the other and cooled down by a fan as used in the setup.

The image of the completed metal box prepared for the test beam and containing the elements described above is shown in Figure 3.3:

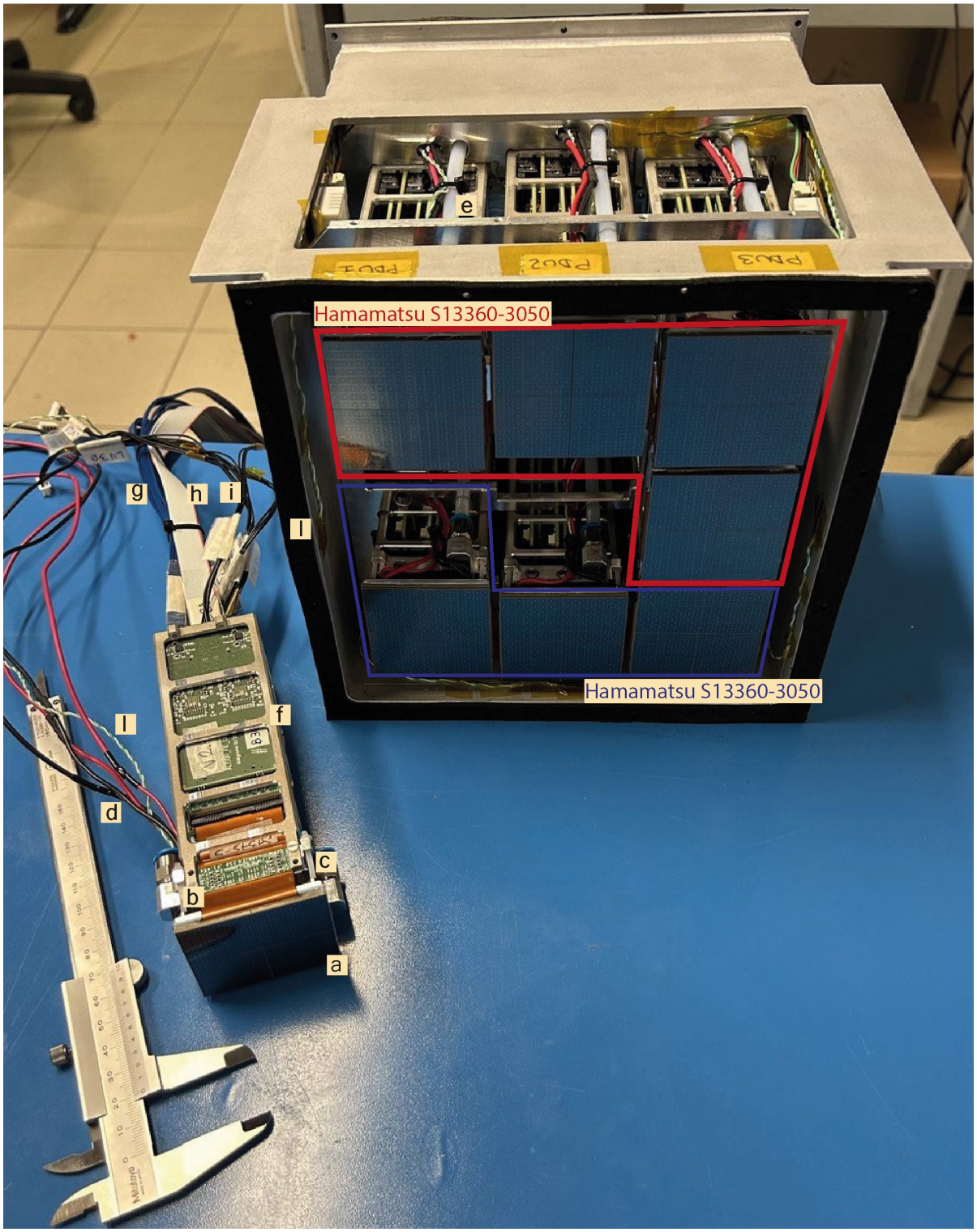

Figure 3.3: Image of the set up of the prototype dRICH readout with thermoelectric cooling inside the metallic box. The picture shows how the mini-crates are positioned inside the box, with Hamamatsu S13360-3050 and Hamamatsu S13360-3075 SiPMs (a). Beside the SiPM are located the carrier board (b) and the Peltier modules (c) whose power supply is given through the cables (d). The Peltier elements hot face is cooled by circulating water through tubes (e). Each carrier board is connected with an ALCOR DUAL and the adapter board (f) which are in turn connected with firefly cables (g) to the FPGA, with cables (i) to the low voltage power supply and with a flat cable (h) to the Master Logic. All these elements form a single PDU (left). The box temperature and humidity along with the Peltier temperature are measured through sensors based on thermocouples (l).

3.2 Quality Test and characterization of the single components

The following section presents all the tests conducted on the individual components of the acquisition and readout system of the dRICH detector prototype, in which I personally participated. This includes the implementation of the measurement apparatus used for testing, the execution of the tests themselves and the corresponding results.
The tests presented here focus on the correct operation of the SiPMs, their proper communication with the readout system, and the performance and efficiency of the SiPM cooling system. Sections 3.2.2 and 3.2.3 focus on NTCs[3] and SiPMs quality assurance and characterization measurements, while 3.2.5 and 3.2.6 on the integrated cooling system building and performance validation process.

3.2.1 Test equipment

During the test processes several instruments have been used:

- **Climatic Chamber MEMMERT CTC256**;
  It is an environmental test chamber that guarantees the right atmosphere for climate and temperature tests [26]. The climatic chamber is used along with a heatless regenerative desiccant dryer KAESER DC 2.0 that keeps the air humidity low to down the dew point temperature at -70 $°C$, which is well below the test temperature of $-30°C$, avoiding to reach the dew point during experimet processes.
- Thermal imaging Camera **FLIR**[4];
- A TSX1820P Programmable DCPSU power supply for the Peltier elements;
- A QL355TP power supply to the front-end boards for the DCR test and for the PDU tests;
- parallel power supplies CAEN A2551A and A2553A providing respectively 8 V/12 A and 32 V/ 3 A;
- Refrigerated circulator HAAKE PHOENIX II C41P and pipes for water circulation.

The **dRICH electronic launch control** interface, shown in Figure 3.4, has been used to begin and stop the supply and measure processes, while for monitoring the state, the temperature conditions, current and voltage levels of the systems within the apparatus Grafana has been used.

3.2.2 Comparative Analysis of NTC Performance Across Varying Temperatures

The DCR of the SiPM, as explained in Section 2.1.4, decreases with temperature. Thus, to obtain better measurement conditions, throughout the detection of Cherenkov light,

[3]NTC stays for Negative Temperature Coefficient. The NTC Thermistors are non-linear resistors that display large changes in resistance as a consequence of small temperature changes [25]. With a small direct current passing through the semiconductor material of the NTC is possible to measure the voltage drop and thus the resistance, through which their temperature can be obtained.

[4]Fixed camera FLIR A400 Smart Sensor + Smart Sensor Configuration for quality assurance tests [27].

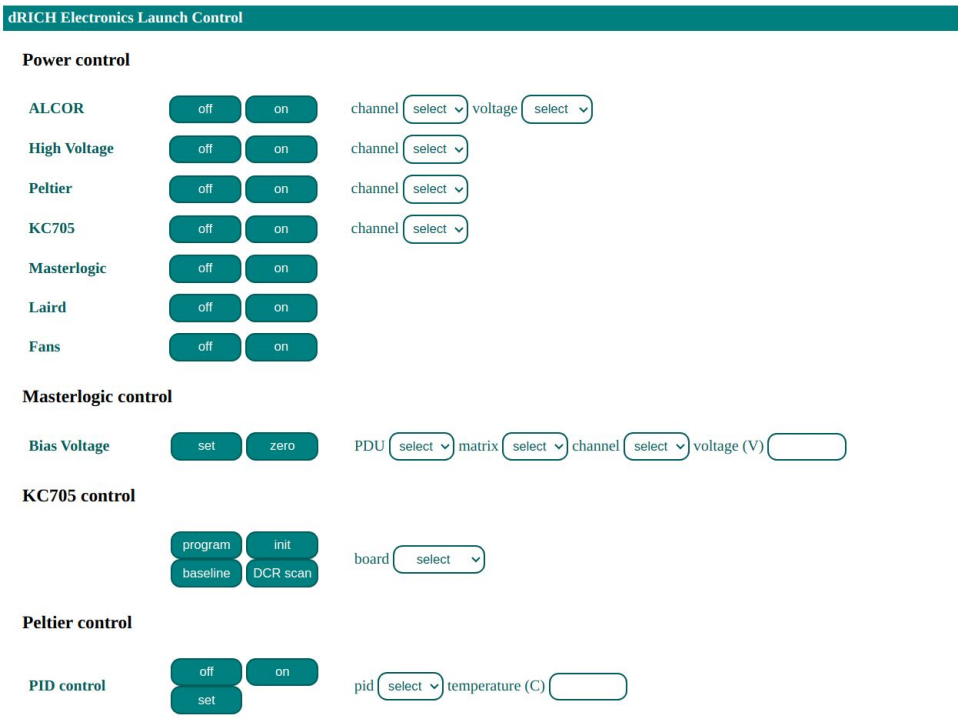

Figure 3.4: Image of the interface of the dRICH electronic launch control on the computer screen. The interface is divided into several sections, including power, Masterlogic, FPGA and Peltier modules control settings. It features a technical layout with clearly labeled elements, allowing precise control during the experiment.

the SiPMs are held at $-30°C$. The temperature is monitored through NTC thermistors, installed on the backside of the SiPM carrier board, as shown in Figure 3.5. The response of the NTC temperature sensors has been tested for the eight SiPM carrier boards used in the prototype. We also tested a spare one. The NTCs test has been carried out on every matrix of the PDUs[5] S1375-1, S1375-2, S1375-3, S1375-4[6], S1375-5, S1350-1, S1350-2, S1350-3 and S1350-4.

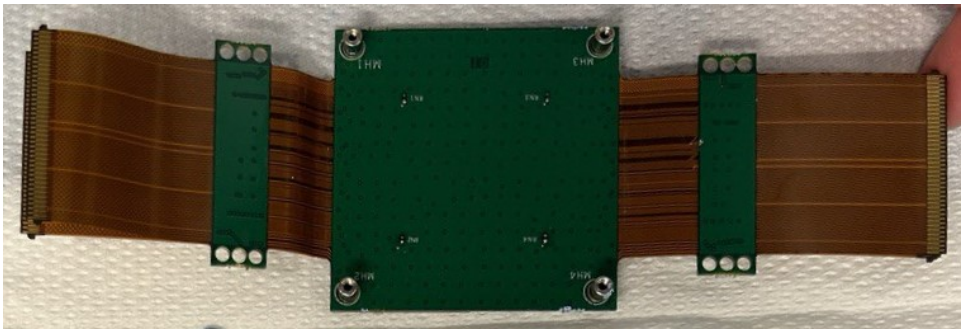

Figure 3.5: Image of the SiPM carrier board where are visible the four NTCs, each associated with one of the four SiPM matrices of the single PDU.

[5]The acronyms S1375 and S1350 refer to the matrices of 75 and 50 μm used in each PDU. The serial number was assigned in the laboratory to identify each PDU.

[6]The spare one.

Inside the Climatic Chamber

The test setup inside the climatic chamber is displayed in Figure 3.6. The NTC sensors inside the chamber have been connected to the full readout system. Each matrix of the SiPM carrier, containing the NTC sensors, has been connected to an ALCOR board and an adapter board, which in turn has been connected to the Master Logic with a flat cable. This allowed the sensor to have the power supply (Master logic boards have been connected throughout the test to the CAEN power supply with a total of 64 V) and to be monitored by the application Grafana. The climatic chamber has been driven through the dRICH electronic launch control.

Figure 3.6: Set-up of the NTC functionality test inside the MEMMERT climatic chamber for SiPM S1375-1, S1375-2, S1375-3, S1375-5 (left) and S1350-1, S1350-2, S1350-3, and S1350-4 inside the mini crate (right).

Grafana

Grafana is the computer interface through which the temperature measures of the NTCs inside the chamber have been collected. An image of the display of the application Grafana is shown in Figure 3.7.

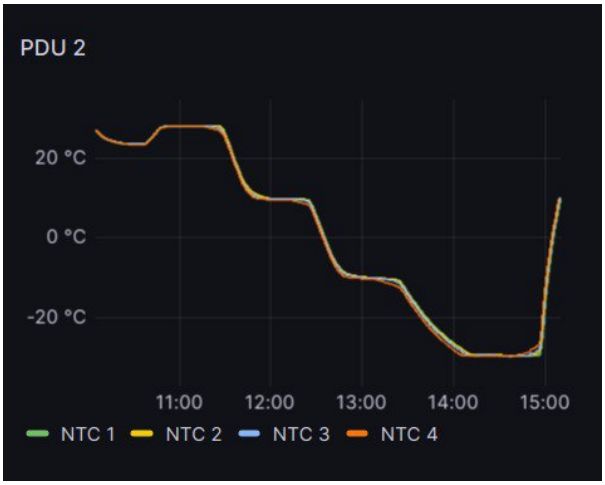

Figure 3.7: Grafana interface for NTC temperature measurements. Measures relative to S1350-1 carrier.

Data NTC test

The data used for this testing process have been collected by simultaneously placing the four NTCs of each tested PDU inside the MEMMERT to guarantee stable temperature. Measurements have been performed at various temperatures between -30 $°C$ and 30 $°C$. The measurements have been taken for approximately ten minutes at four selected temperatures, respectively $+30°C$, $+10°C$, $-10°C$, $-30°C$. Particular care has been taken to guarantee that the measurements were taken when the climatic chamber reached a stable temperature. A waiting time in the program and a verification of the reached temperature process has been set. The reference temperatures used were those provided by the climatic chamber, to test the response of the NTC sensors and ensure that they were properly working[7]. Taking into account the time necessary to the chamber for operating these temperature changes, each test lasted approximately 4 hours, allowing us to test 2 boards, and thus 8 NTCs of SiPM matrixes, per day of testing.
From the analysis four data sets were obtained, one for each selected temperature value with a rate of 1 second, for each NTC of the nine examined boards. One of the plots obtained of the NTC temperature measurements is shown in Figure 3.8. The mean values of these sets of measurements from the NTCs are presented in Table 3.2.

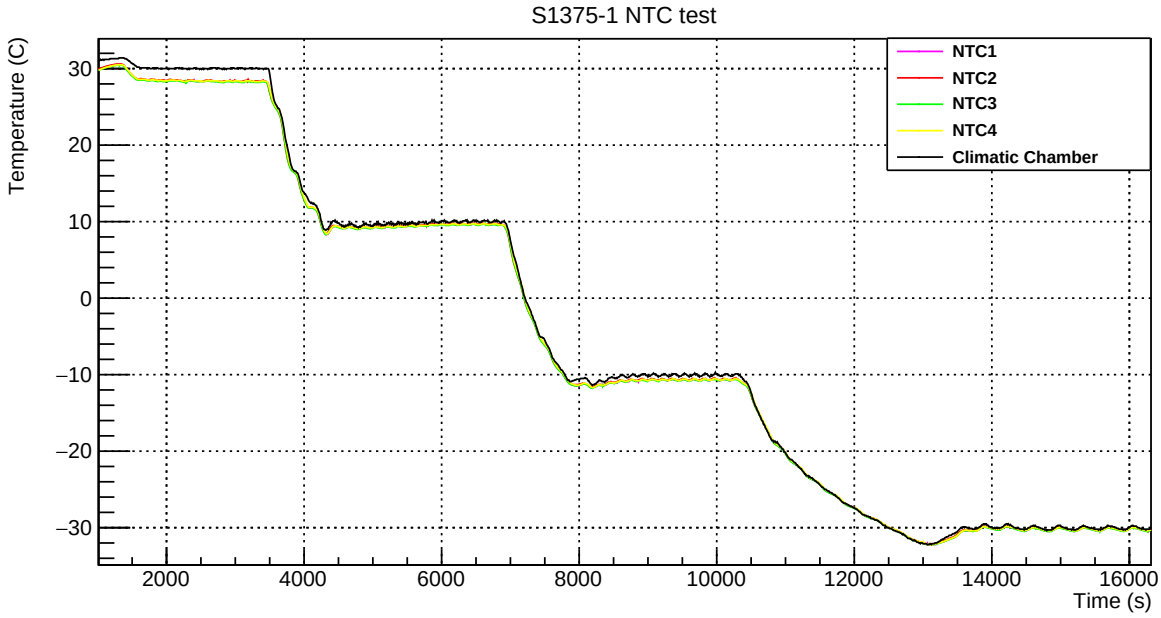

Figure 3.8: Graph of the measured temperature by the Memmert Climatic Chamber, considered as the true measure, and the NTCs measurements for the PDU S1375-1.

NTC calibration results

This test was necessary to assess the functionality of the NTCs, but also useful to ensure that the response and temperature calibration remained within our specifications (a margin of a few degrees).
The obtained data have been analyzed in order to verify the accuracy of the NTC. In Figure 3.9 (a) are shown the values for the temperature differences between the ones measured by every NTC of S1375-1 unit and the expected ones (-30,-10,10,30 $°C$),

[7]The previous batch of the SiPM carriers had many of these NTC not properly functioning, therefore this test was a mandatory quality assurance one.

SiPM carrier	MEMMERT	NTC 1	NTC 2	NTC 3	NTC 4
S1375-1	30	28.42	28.47	28.32	28.42
	10	9.65	9.73	9.59	9.66
	-10	-10.7	-10.62	-10.73	-10.67
	-30	-30.22	-30.15	-30.28	-30.21
S1375-2	30	28.16	28.38	28.38	28.36
	10	9.39	9.57	9.61	9.54
	-10	-10.91	-10.72	-10.69	-10.73
	-30	-30.38	-30.23	-30.19	-30.25
S1375-3	30	28.27	28.25	28.44	28.34
	10	9.64	9.63	9.82	9.68
	-10	-10.61	-10.64	-10.45	-10.56
	-30	-30.2	-30.28	-30.09	-30.19
S1375-5	30	28.48	28.34	28.41	28.3
	10	9.74	9.6	9.67	9.55
	-10	-10.42	-10.59	-10.48	-10.58
	-30	-30.05	-30.14	-30.07	-30.14
S1350-1	30	28.32	28.4	28.4	28.2
	10	9.85	9.91	9.92	9.74
	-10	-10.1	-10.03	-10.03	-10.18
	-30	-29.73	-29.68	-29.67	-29.8
S1350-2	30	28.5	28.4	28.5	28.33
	10	9.9	9.8	9.91	9.78
	-10	-9.95	-10.05	-9.94	-10.07
	-30	-29.54	-29.64	-29.54	-29.67
S1350-3	30	28.2	28.15	28.14	28.06
	10	9.76	9.7	9.7	9.64
	-10	-10.22	-10.29	-10.26	-10.33
	-30	-29.82	-29.9	-29.87	-29.94
S1350-4	30	28.11	28.3	28.28	28
	10	9.72	9.9	9.9	9.65
	-10	-10.19	-10.06	-10.05	-10.26
	-30	-29.85	-29.72	-29.73	-29.93

Table 3.2: NTC test mean values obtained for every Thermistor at $+30°C$, $+10°C$, $-10°C$, $-30°C$ temperatures.

$\Delta T = T_{NTC} - T_{true}$, as a function of the climatic chamber predicted temperatures. The graphs relative to all the PDUs comprehensive of the error bars, are shown in Appendix A.1. The NTC readout system turned out to be all functioning and well-calibrated. The

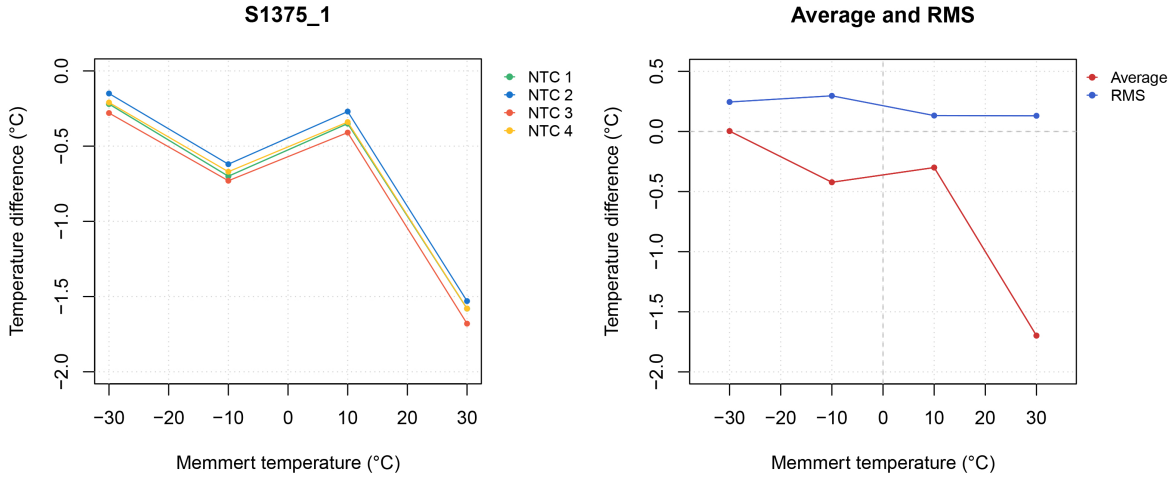

(a) (b)

Figure 3.9: Results of the nine PDUs whose NTCs have been tested (a) Trend of the temperature differences between the measured and expected values for NTC 1, 2, 3, and 4 of the PDU S1375-1, plotted as a function of the climatic chamber temperatures (The graphs of all the NTC temperature difference measurements are in Appendix A.1). (b) Mean value of the temperature differences across all the verified NTCs and the root mean square of all the difference values as functions of the Memmert temperature. Both of these plots are generated using the software environment R.

measured temperature is sufficiently accurate for using NTCs in the context of SiPM temperature monitoring because, as shown by the graphs in Figure 3.9 (a) and Appendix A.1, the temperature difference ΔT remains steadily below $1°C$ for values below -10°C. However, a larger deviation from the actual climatic chamber value was measured at the highest temperature of 30 $°C$, a fact that can be neglected given the good coincidence of the value at the operating temperature of the prototype, which is -30 $°C$. Thus, it has not been necessary to apply corrective factors to the calibration of the NTCs.
In Figure 3.9 (b) are plotted the average of the temperature differences ΔT of all the NTCs and their associated Root Mean Square. At temperatures under 10 $°C$ measures are extremely accurate, within half a degree. Only at higher temperatures, as previously mentioned, the mean difference in absolute value grows, yet the RMS stays below 2 degrees Celsius, which is acceptable for the purposes of this study. The RMS also demonstrate that all the NTCs are, on average, accurate[8] and highly homogeneous with each other, with dispersion of at most **0.3** degrees at -10 $°C$. It can be observed that at -30 $°C$, the mean temperature difference is zero, while the RMS is 0.25 $°C$. This indicates a Gaussian distribution of the temperature differences at the lower MEMMERT chamber temperature, where sigma is 0.25 $°C$. This means that at -30°C all the NTCs are within a 0.75 $°C$ scope from the expected temperature. These data indicate that a residual calibration could be developed for the higher temperatures with a further study. However,

[8]The analysis points out a good state of the NTC used to assemble the prototype subject of this study. None of the tested NTCs has been replaced. Similar tests of the NTCs for the previous prototype in 2023 had shown a high level of damage, with at least one NTC not properly functioning on each PDU that needed to be replaced.

this falls outside the scope of our interests, as the SiPMs of the prototype operate at low temperatures.

Estimation of the true value from the NTC measurements

No corrections were applied to the calibrations of the NTCs used during the operation of the prototype, because them perform well at the working temperature of the prototype, as remarked before. However, below is stated an equation estimation that allows us to derive the true values of the temperature of the sensors, from the measurements obtained through the NTCs. The results presented here could, in the future, serve as a methodology to apply corrections to the NTC calibrations. In Appendix A.2 are reported the graphs with the parameters related to the NTCs of all the PDUs used in the prototype. The mean values of the obtained parameters describing the correlation between the true temperature value (T_{true}) and the values measured by the NTCs (T_{NTC}) are listed, along with their uncertainties, in Table 3.3:

Mean Fit Parameters			
$p0$ ($^{\circ}C$)	$p1$	$p2$ ($^{\circ}C^{-1}$)	$p3$ ($^{\circ}C^{-2}$)
0.21 ± 0.01	(-7.4 ± 0.9)·10^{-3}	(8.4 ± 0.2)·10^{-4}	(4.6 ± 0.1)·10^{-5}

Table 3.3: Mean parameters obtained as a mean of the third-degree polynomial fits from each of the 36 analyzed NTCs, shown in Figures A.3, A.4, A.5, A.6, A.7, A.8, A.9 and A.10 inside the Appendix A.2. The associated uncertainties are calculated as standard uncertainty of the mean for independent variables. (Fit parameters computed by the ROOT framework; $p0$ is the constant term, $p1$ is the linear coefficient, $p2$ is the coefficient of the quadratic term and $p3$ is the coefficient of the cubic term.)

Through these parameters, the subsequent equation for obtaining the true temperature of the sensors measured by the NTCs has been obtained:

$$T_{true} = p0 + (p1 + 1)T_{NTC} + p2\,T_{NTC}^2 + p3\,T_{NTC}^3 \tag{3.1}$$

This method allows us to derive correct measurements with a precision better than 0.15 $^{\circ}C$ at temperatures below 10 $^{\circ}C$. Finally, upon a careful examination of Figure 3.8, qualitative temperature oscillations common to both the NTCs and the climatic chamber measurements can be observed. These oscillations are due to the cooling system of the MEMMERT climatic chamber, which does not eliminate temperature fluctuations during data acquisition. These fluctuations then affect the NTC measurements and their associated uncertainties. Thus, a more detailed analysis could reveal a better actual precision of the NTC temperature measurements. Therefore, this system is potentially more precise than reported, but such in-depth analysis falls outside the scope of this thesis.

3.2.3 DCR threshold scan and SiPM communication test

The SiPMs exhibit a high Dark Count Rate (DCR), as mentioned previously, which is a stochastic process indistinguishable from photon signals [28]. The DCR can be obtained by measuring in the absence[9] of light the frequency of the events detected

[9]This is an ideal condition. In the laboratory where the test was carried out, we tried to achieve this condition by performing the test at night, by placing the SiPMs in a special box and covering it with a black napkin cloth.

above the electronics noise threshold. Therefore, using a test based exclusively on DCR, it is possible to determine whether the SiPM is functioning or not. Five units (four used in the prototype and one spare) each composed of 256 SiPMs, for a total amount of 1280 SiPMs, have been tested in one week. The SiPM tested are the Hamamatsu S13360-3075 ones inserted in the PDUs S1375-1, S1375-2, S1375-3, S1375-4[10] and S1375-5. Given the large number of SiPM channels, a way to achieve the functionality test in a reasonable time frame has been testing one full PDU (four matrices made of 64 SiPM channels) per day. The data taking was conducted during the night in order to avoid light interference, covering the setup with a black suede cloth. The setup, illustrated in Figure 3.10, includes the full readout system with the ALCOR chips connected to the low voltage cables for the ALCOR power supply (2 V for the analog power and 3 V for the digital power) and with the firefly data cables to the FPGA. Each of the four ALCOR boards and matrices are also connected to the adapter board, which is connected to the Master Logic, consequently to the high voltage, through a flat cable. The readout system has been the same through all the processes, only the PDUs have been changed to be tested. A threshold scan on the photon detection rate from all the SiPMs channels of

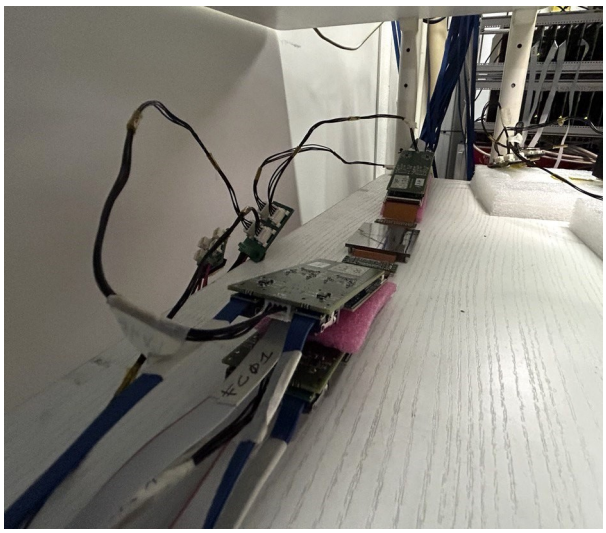

Figure 3.10: Setup for DCR test.

each PDU has been performed. The threshold can be changed through a software that associates voltage values to an integer set of numbers from 0 to 63. Measurements start from a pre-determined threshold level to obtain clearer results, avoiding the detection of electronic noise and optimizing data acquisition time. As the threshold voltage grows the frequency of dark counts is acquired. At a specific threshold, a signal selection cut occurs (which corresponds to the drop in rate that separates the two plateaus). This indicates the point at which the discriminator threshold is larger than the amplitude of the single-photon signal from the SiPM. The SiPM signals at a larger thresholds are the ones due to DCR and cross-talk. Since we do not have an analog-to-digital converter, and the signal is provided by the adapter boards, what we observe is a step that separates the signal associated with the detection of a single photon from that associated with multiple photons. The test is started through the dRICH electronic launch control and every matrix is supplied with 500 mA. The eight-channel arrays of the single matrix have independent voltage. The mean measurements of the dark photon detection rate as a function of the threshold voltage (at which data acquisition is triggered) are plotted

[10]The spare one.

in Figure 3.11. The graph is made of two levels, the first one at a higher rate and the

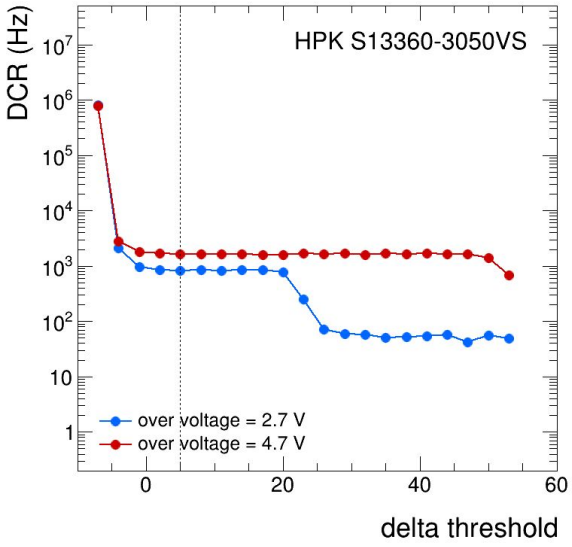

Figure 3.11: Plot of the DCR as a function of the delta threshold.

second at a lower rate, separated by a step threshold value. The higher rate is the DCR measured by setting the threshold at half the amplitude of the signal corresponding to a single avalanche, at half-photon level, the lower rate is the DCR measured by setting the threshold at one and a half single-cell signal. Therefore, the mean SiPM count rate from the higher plateau corresponds to the rate associated with the detection of a single photon, whilst the one from the lower plateau corresponds to the rate associated with the detection of more than one photon. Through the known threshold value, it is possible to measure the rate.
The SiPM channels, being formed by the same type of SiPMs, gave similar results proving to be all properly working. Some of the results are shown in Figures 3.12, 3.13, 3.14 and 3.15.

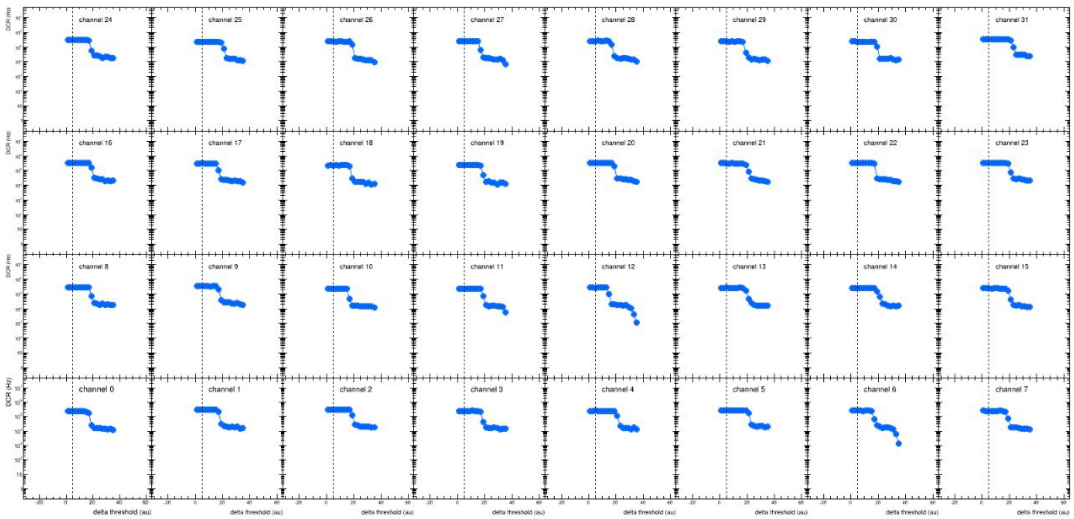

Figure 3.12: Threshold scan of 32 sensors on the SiPM matrix U1 of the S1375-1 unit performed at room temperature with no impinging light, with an NTC average of 28°C, with baseline taken at 0 V and a bias voltage of 53 V.

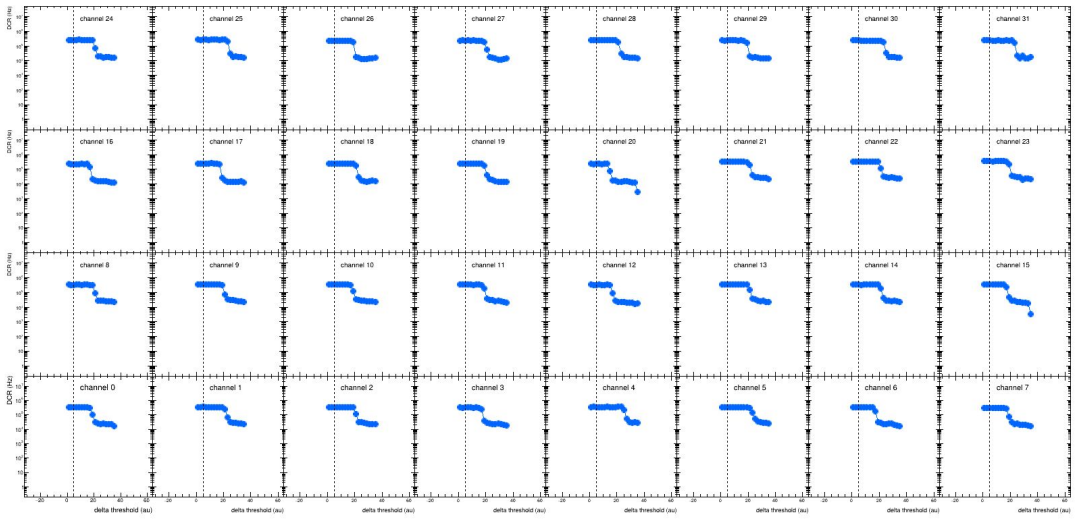

(a)

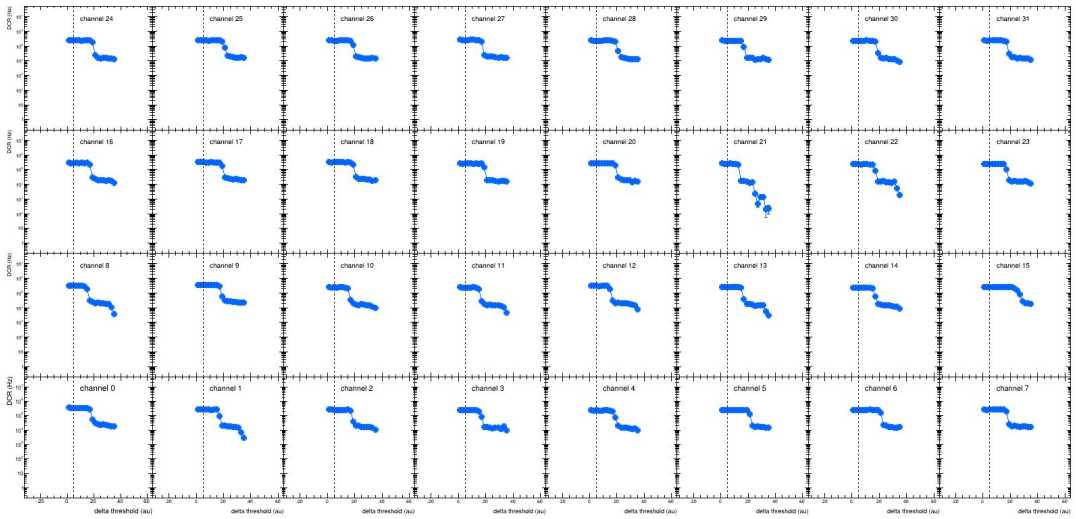

(b)

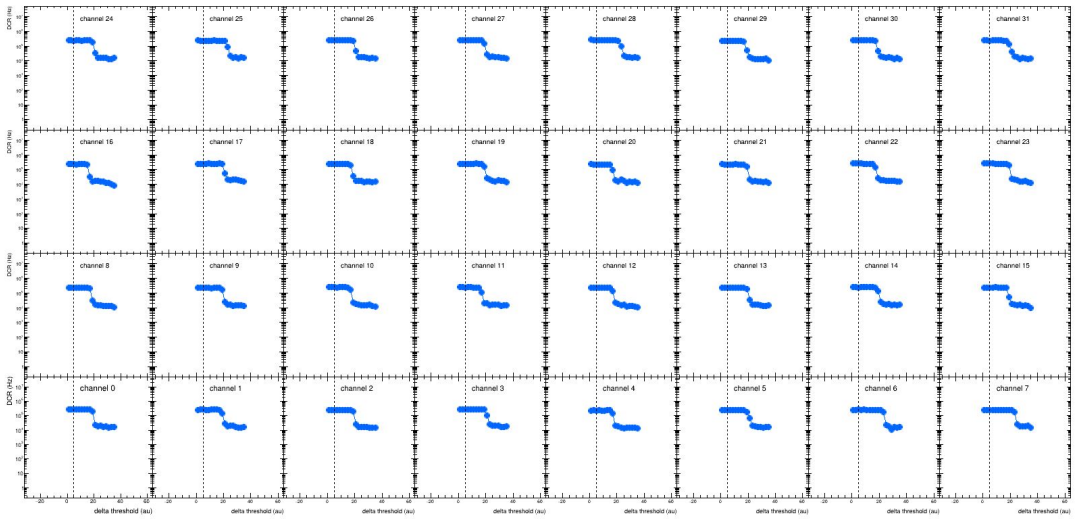

(c)

Figure 3.13: DCR test on the other 32 channels of U1 (a) and of the 64 channels of U2 (b) of the S1375-1 unit.

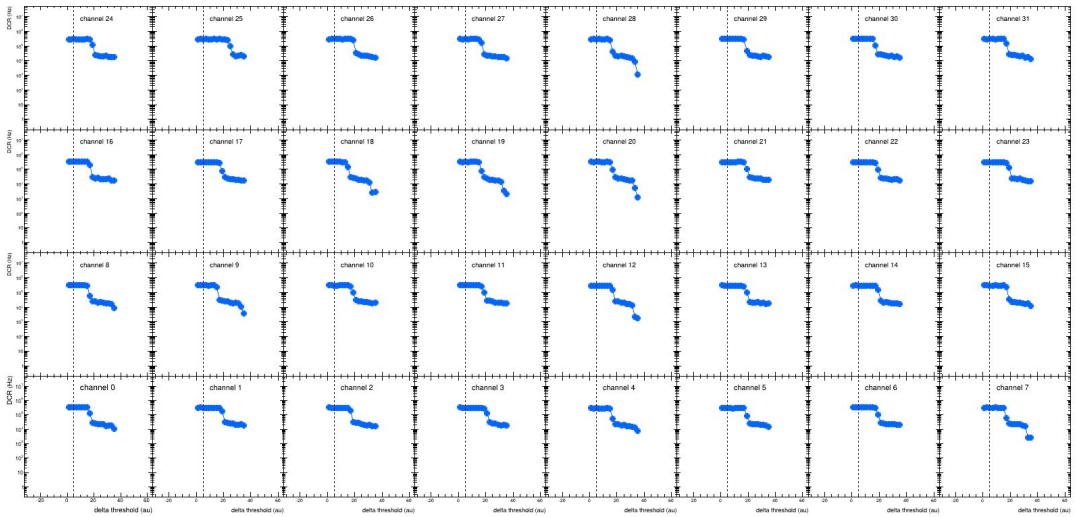

(a)

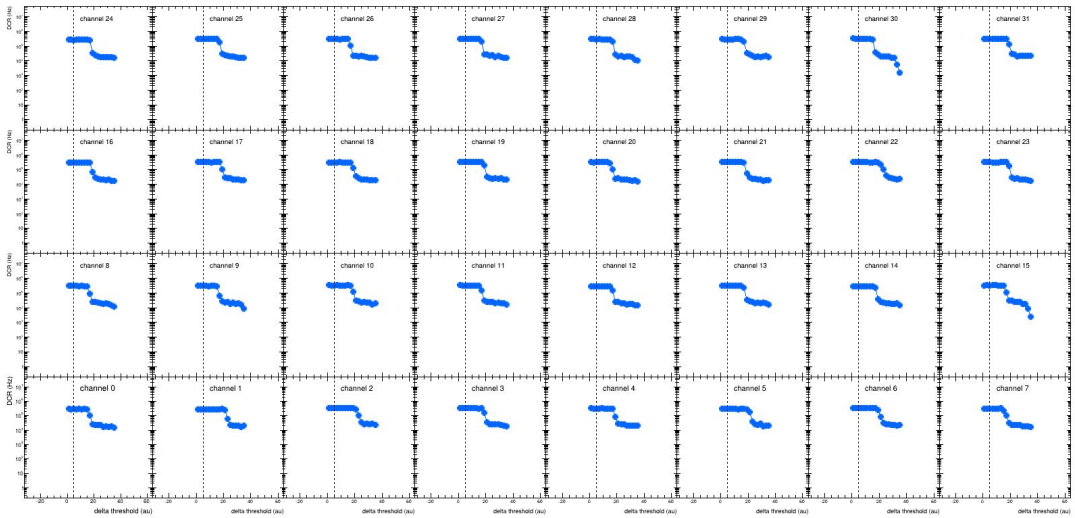

(b)

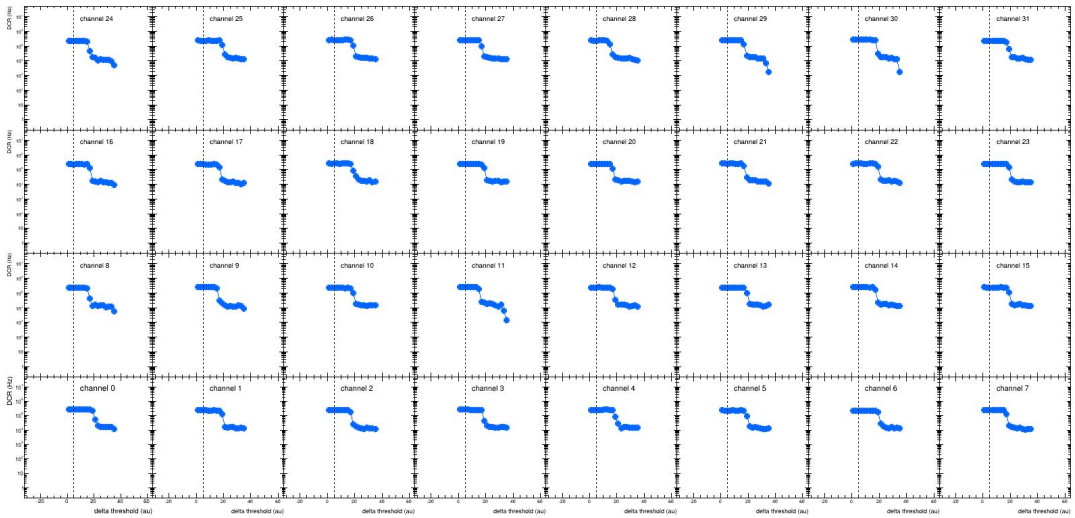

(c)

Figure 3.14: DCR test of the 64 channels of U3 (a) and of 32 channels of U4 (b) of the S1375-1 unit.

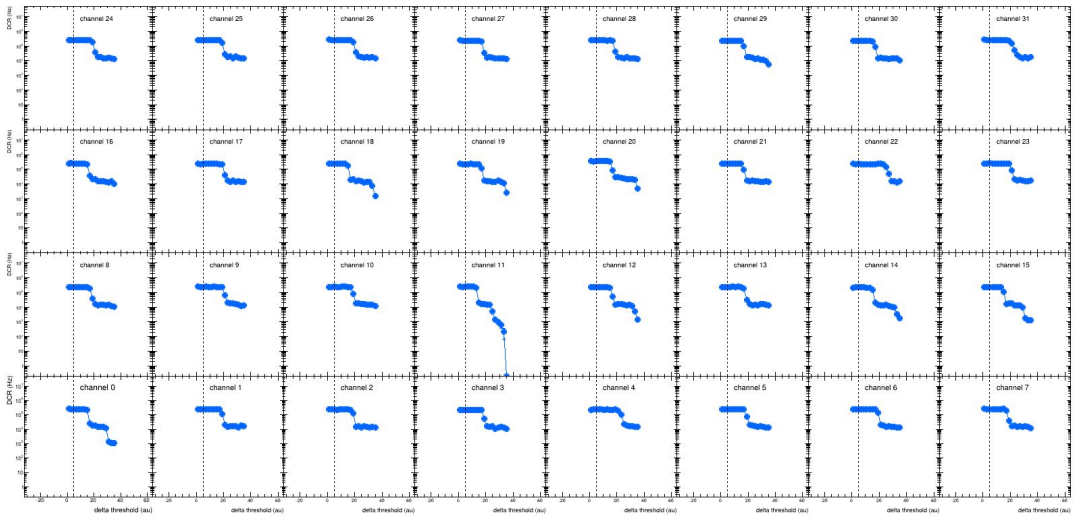

Figure 3.15: DCR of the last 32 channels of U4 of the S1375-1 unit.

3.2.4 Recovery of 2023 matrices

As stated in Section 2.2.2, the Peltier module is a thermoelectric cooling system that enables cooling on one surface and heating on the other when a low DC voltage is applied. In this case, it allows heat transfer from the face in contact with the SiPM carrier board to the other face, in contact withh the water-cooled cooling plate. The heat is dissipated from this surface through a mechanical low-temperature water circulation system using the HAAKE refrigerated circulator. In this phase, the supports used in the previous prototype of the detector, developed in 2023, were separated from the Peltier modules, as shown in Figure 3.16. This process allowed us to reuse the cooling system pieces replacing the four partially-populated SiPM matrices with new ones, fully populated with SiPM.

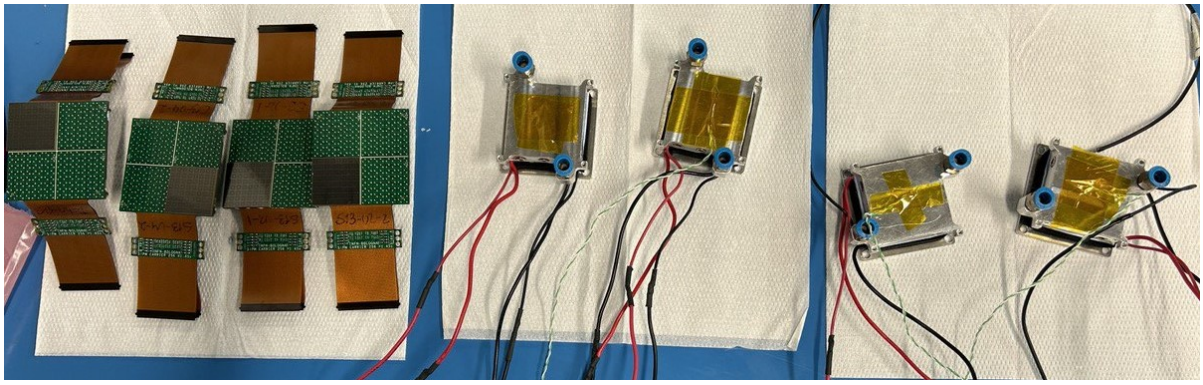

Figure 3.16: Laboratory process of separation of the 2023 matrices (left) for the prototype from the Peltier refrigeration structure modulus (right) used successively for the PDUs S1375-1, S1375-2, S1375-3 and S1375-5.

3.2.5 Leak-tightness inspection of water-cooling cables for Peltier cell

The dRICH SiPM photodetector unit has an integrated cooling system composed of one custom-made cooling plate made of aluminum ($\sim 50 \times 50 \times 19\ mm$) where water is circulating which is used to keep the hot face of the Peltier module at a constant temperature of around between $15 - 20°C$. The Peltier modules, as said previously, are used to cool down and create a heat flow from the cold face to the hot face which therefore allows the creation of a temperature difference and cool down the SiPM matrixes, which are in connection with the cold side of the Peltier element. To ensure that the system is thermally efficient thermal contact must be good. Several tests have been done to guarantee the soundness of the cooling system, from the point of view of the water tightness of the pipes and heat exchange block and thermal contact between the various surfaces.
The inspection of the leak-tightness of the water-cooling structure has been performed on all of the four previously separated cooling systems. This has been done to prevent, during the assembly and data acquisition phases, water leaks that could come into contact with the system's electronics.
The external cooling system was connected and tested sequentially for the four units S1375-1, S1375-2, S1375-3 and S1375-5. After the pipes for the external cooling system have been connected to the circulating structure in connection with the Peltier modules, the water circulation was initiated at +20°C in the HAAKE refrigerated circulator and maintained for approximately ten minutes. At the end of this period, after verifying

that there were no leaks, a handheld FLIR thermal camera was used to check that the temperature on the upper surface of the Peltier modules was comparable to that of the incoming water. Furthermore, this demonstrated the good condition of the thermal connection layer between the Peltier module and the water circulation system. The test setup can be observed in Figure 3.17.

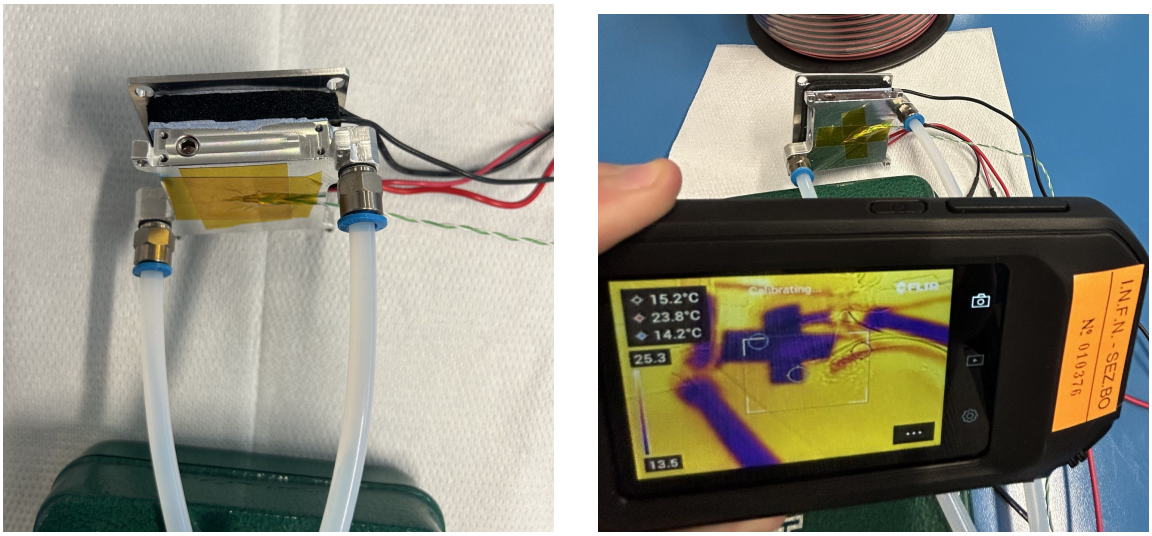

Figure 3.17: Connection of the pipes to the cooling structure (left) and temperature measurement with a thermal camera (right).

Assembly of SiPM with Peltier elemens

To proceed with the functional testing of the Peltier modulus, the SiPM units have been assembled with the integrated cooling system. After shaping and positioning on the Peltier structures base a thermal pad using a die-cutting tool with a 3-point tip, the cooling system was attached to the carrier and subsequently to the detectors. Thus, Peltier modules have been placed in contact with the detectors through a thermal silicone pad[11] to ensure thermal contact and therefore uniform heat conduction between the sensors and the cooling system. This also served to prevent air layers from forming between the two components, as air is a poor conductor of heat. Finally, the isolated Peltier modules were cleaned with isopropyl alcohol. The cables were aligned uniformly across the four units. The image of the assembled system is reported in Figure 3.18.

3.2.6 Functional testing of the integrated cooling system

While the PDUs S1350-1, S1350-2, S1350-3, S1350-4 were already been tested and assembled inside the mini crates, this test has been performed on the remaining four, the S1375-1, S1375-2, S1375-3 and S1375-5.
This test has been performed with the aid of the Thermal imaging Camera FLIR and the Power supply TSX1820P Programmable DCPSU. We assembled the modules and connected them to the chiller to circulate water for heat dissipation. Additionally, we connected the Peltier cell cables to a power supply and positioned the system in front of the thermal camera connected to the computer that took thermal images of the Sensors,

[11] Liart technology tflex 600 series thermal gap filler interface that produces low terminal resistance with a thermal conductivity of 3 W/mK [29].

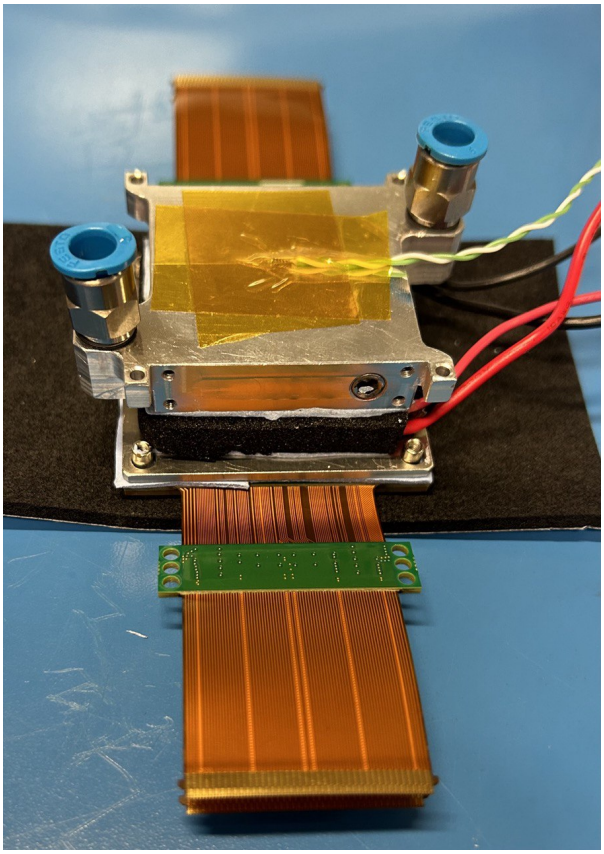

Figure 3.18: SiPM carrier board connected through the thermal pad to the Peltier element and the aluminum cooling plate.

allowing us to verify both the proper adhesion of the thermal pads and the overall functionality of the cooling system. The setup is shown in Figure 3.19. The integrated

Figure 3.19: Photon detection unit sensors aligned with the FLIR thermal camera (left) and the stabilized setup of the test (right) drawing attention to the power supply connected to the Peltier cells and the water circulating pipes.

cooling system has been connected through the pipes for water circulating to the HAAKE refrigerated circulator. The cables of the two inner Peltier cells were connected to the power supply in parallel. The system was tested with 1 A of current and approximately 2 V. This configuration allows independent control of the individual PDU units. If the thermal pad had been poorly connected, resulting in low conductivity, the thermal camera would have measured an uneven temperature distribution. Consequently, the unit was stabilized in alignment with the thermal camera.

Thermal Imaging-Based Temperature Test

The water circulation system was set to +40°C while keeping the Peltier modules inactive to initially verify the proper flow of water. For heat dissipation, a steady temperature of +35°C was reached on the detectors, measured using the thermal camera. While maintaining the water flow at +40°C, the power supply and consequently the Peltier modules (connected in parallel) were activated. These modules cooled the SiPMs until the temperature stabilized at approximately +18°C. The cooling, observed via thermal camera, appeared uniform and the resulting images are plotted in Figure 3.20. With 1 A of current

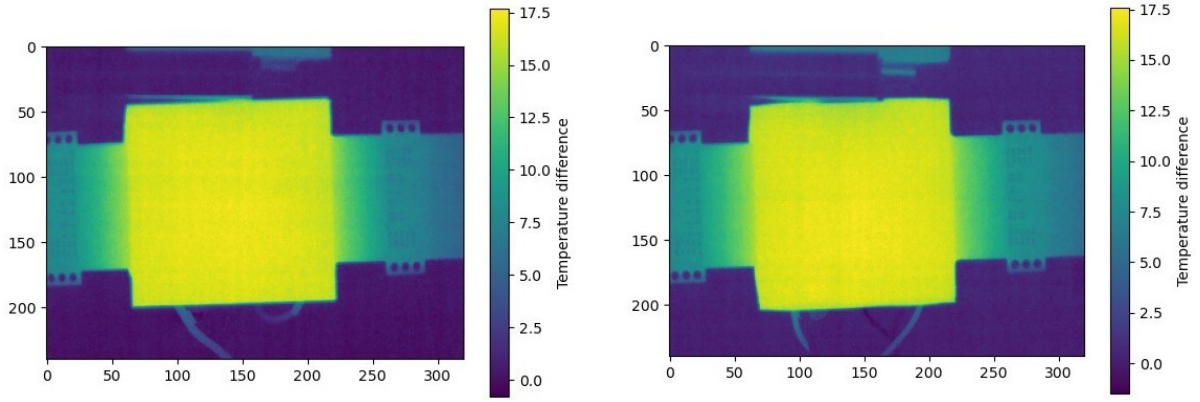

(a) Thermal image of S1375-1 unit

(b) Thermal image of S1375-2 unit

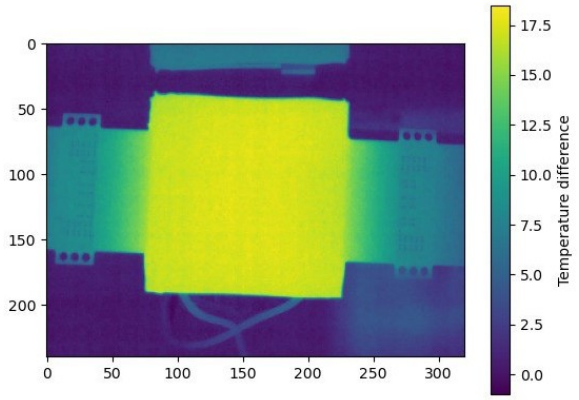

(c) Thermal image of S1375-3 unit

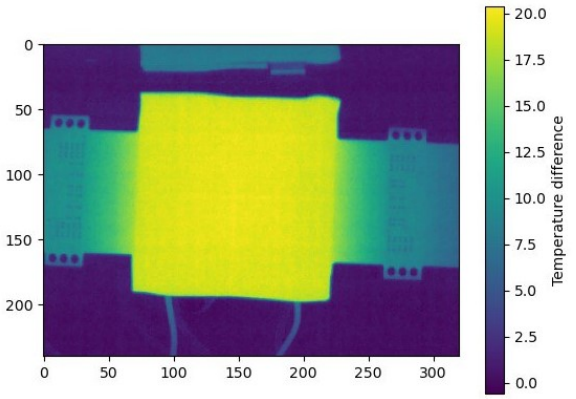

(d) Thermal image of S1375-5 unit

Figure 3.20: Thermal images acquired with the FLIR thermal camera showing the temperature difference obtained by subtracting thermal images taken before and after the activation of the Peltier elements. The values are measured in K.

input, the Peltier modules absorbed around 2 W of power (with a potential difference of approximately 2 V), generating a temperature difference of about 20 degrees. The generated plot shows the temperature difference between the sensors at room temperature with 0 V input to the Peltier cells, and their subsequent temperature after applying 1 A of current to the Peltier cells. As expected, this difference is approximately $20°C$ across the entire surface and in all the tested PDU units. As the image 3.20 shows, the temperature distribution appeared uniform and there were no visible areas with bad thermal contact. The temperature was qualitatively uniform across the entire surface of the SiPMs.

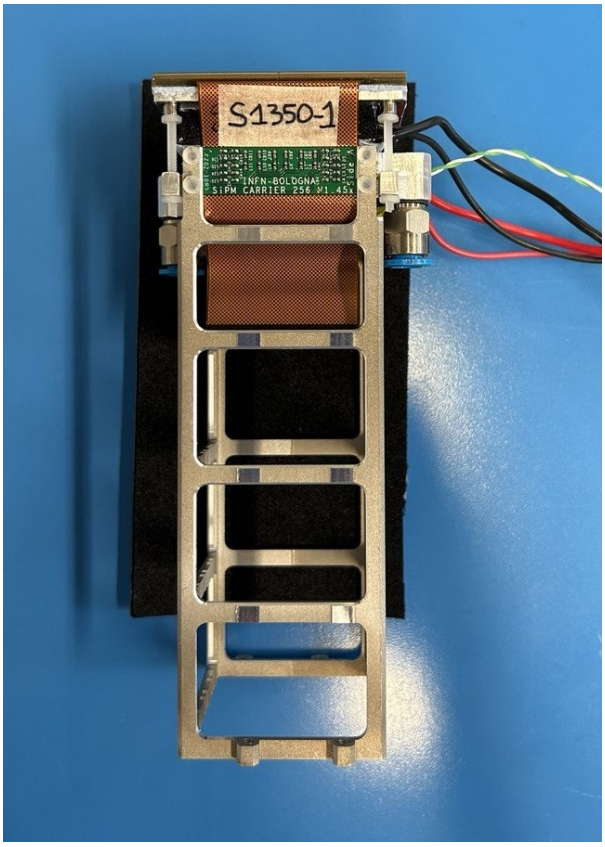

Figure 3.21: Insertion of the SiPM, Peltier, and cooling system unit into the minicrate.

3.3 Final construction and characterization of the prototype

Assembly of the eight units with the mini crates and ALCOR

After testing the individual components of the prototype, the system was assembled. While the PDU units S1350-1, S1350-2, and S1350-3 had already been installed in the minicrate, the structure that comprises the sensors and cooling system for the PDU units S1375-1, S1375-2, S1375-3, and S1375-5 was inserted and secured to the minicrate[12] using small plastic screws, as shown in Figure 3.21. Once the functionality of all 32 ALCOR version 2.1 boards was verified, they were assigned and inserted into the eight minicrates. Each board was connected to a single PDU Matrix, specifically U1, U2, U3, and U4. Before inserting each ALCOR DUAL into the minicrate, two Firefly cables were connected, followed by a Flat Cable connected to the Master Logic, and the low-voltage cable. This process is illustrated in the subsequent Figures 3.22 and 3.23.

Thermocouples

Inside the detector box, eight thermocouples connected to an Arduino board were installed to monitor the internal temperature and humidity of the prototype, particularly near to the electronics. One additional sensor has been installed at the center of the prototype on the minicrate of the PDU number six to measure more precisely the electronics

[12]The minicrate is a 14 cm long, light-weight aluminium lattice case, custom made to contain and secure the electronics connected to the sensor and dissipating system structure.

Figure 3.22: Connections of the single ALCOR and adapter boards.

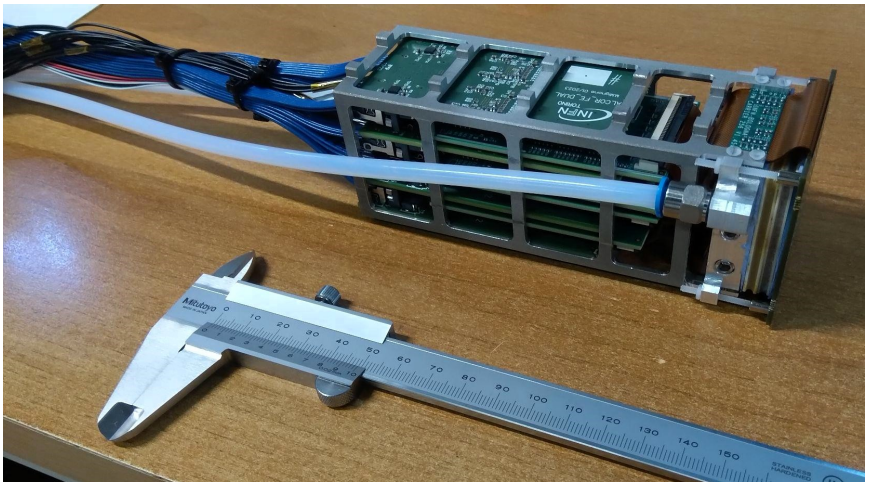

Figure 3.23: Assembled PDU with sensors, four matrixes of 8 x 8 SiPMs sized 3 x 3 mm^2 for a total of 256 channels, thermoelectric cooling system, two Peltier cells for subzero operating temperatures with temperature sensors under the SiPMs (NTC) and on the Peltiers and front-end electronics featuring the ALCOR ASIC chip. The pipes for liquid heat exchange for temperature control of hot-face of the Peltier are also present.

temperature. Their arrangement is shown in Figure 3.24.

Placement of Eight Modules Inside the Metallic Box

The prototype has been assembled inserting[13] all of the previously mounted mini crates in the eight prefixed spaces inside the metallic box and installing the pipes for the water circulation system. The placement of each crate in its PDU position along with the assigned ALCOR boards is schematized in Table 3.4. Several pre-commissioning tests were performed on the assembled box in order to verify the functioning of the full detector prototype. This process took about two days. We used seven FPGA boards[14]. For the available channels all the electronics have been connected as described in Figure 3.3. Each electronic component was connected to the respective Master Logic, Breakout Boards, FPGA, and power supply and all the components connection and functionality was checked. Connections to external readout systems are shown in Figure 3.25. In the final communication test process were detected some PDUs that did not properly communicate with the computer system. After identifying the problematic boards some ALCOR has been removed and substituted with properly working ones. The complete prototype box, fully assembled and tested, is shown in the Figure 3.27.

[13]Mini crates needs to be inserted inside the metallic box from the bottom line upwards.
[14]Some FPGA have been available onward during the Test Beam.

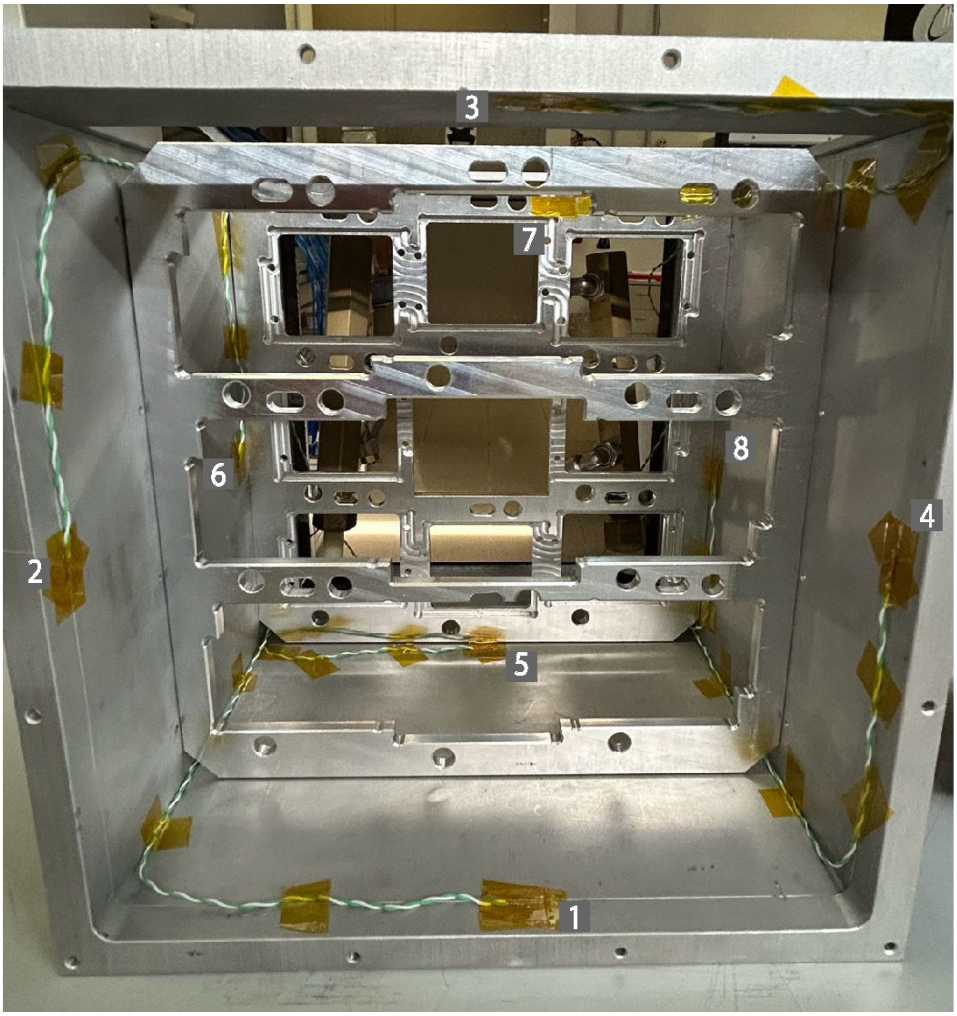

(a)

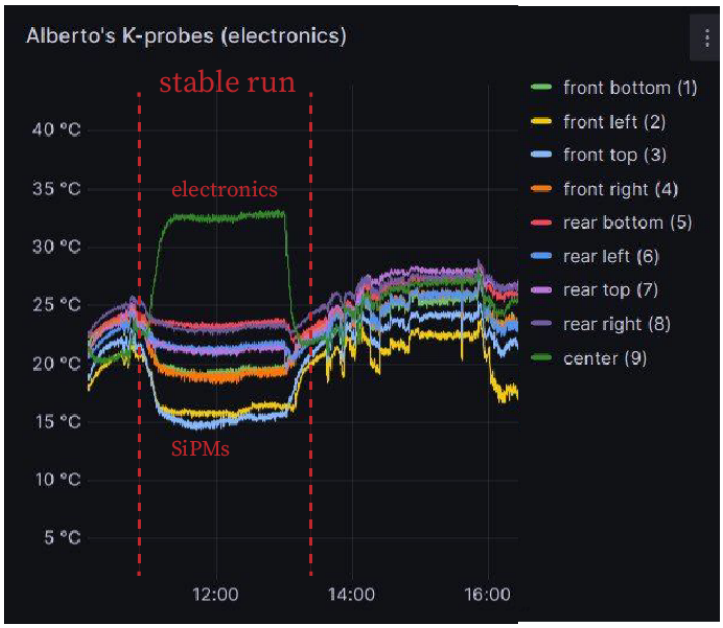

(b)

Figure 3.24: Front view of the temperature and humidity sensors positioned internally to the metallic box of the prototype and respectively numerated. Figure (a) is an image of the thermal sensor positions inside the prototype box, while (b) shows the computer interface for thermocouple readout.

Figure 3.25: Connections of the Adapter Boards with the Master Logic (left) and of the ALCOR chip with the FPGA and clock system (right)

PDU	**Head**	**ALCOR**			
		U1	**U2**	**U3**	**U4**
1	S1350-1	B33	B52	B51	B39
2	S1350-2	B37	B48	B49	B38
3	S1350-3	B53	B34	B45	B50
4	S1350-4	B54	B02	B46	B10
5	S1375-1	B21	B01	B08	B43
6	S1375-2	B14	B44	B04	B06
7	S1375-3	B16	B11	B07	B13
8	S1375-5	B36	B05	B12	B19

Table 3.4: List of PDU position in the metallic box, PDU recognition label (Head) and the corresponding ALCOR boards. The PDUs inside the box are numbered clockwise starting from the top and viewing the detector from the front

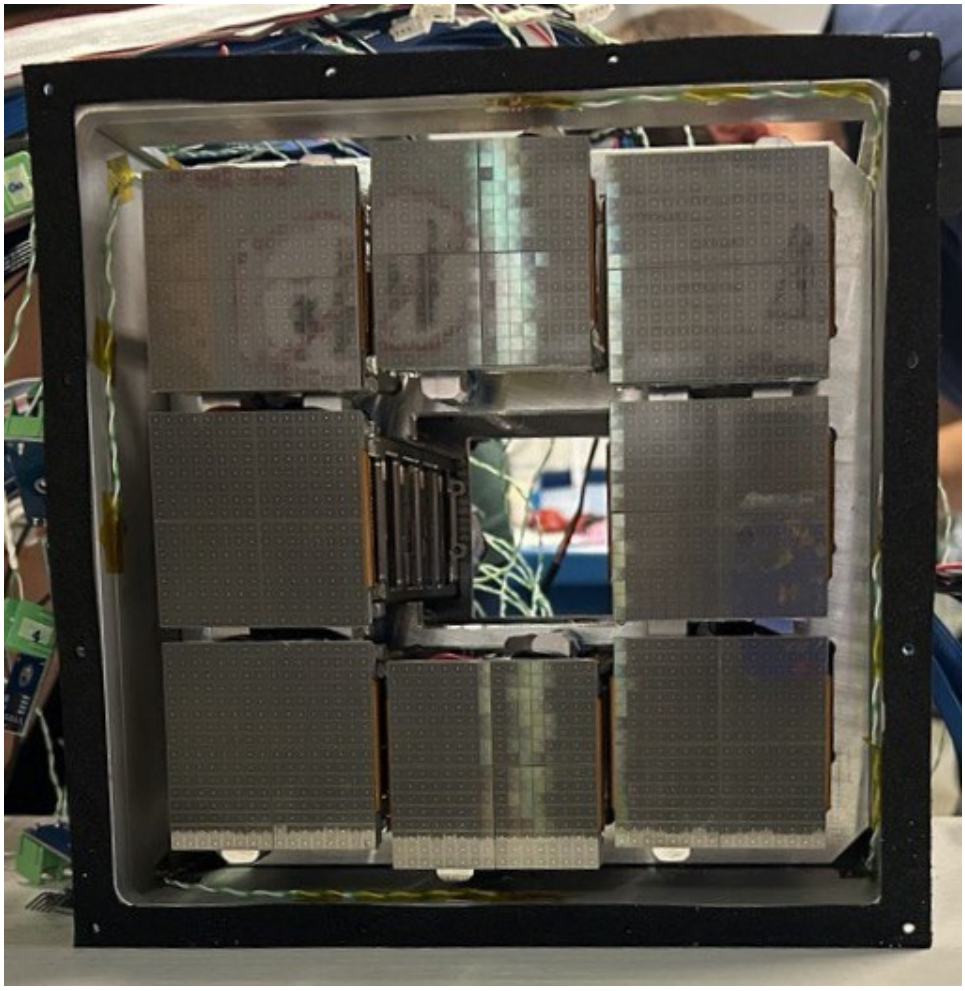

(a)

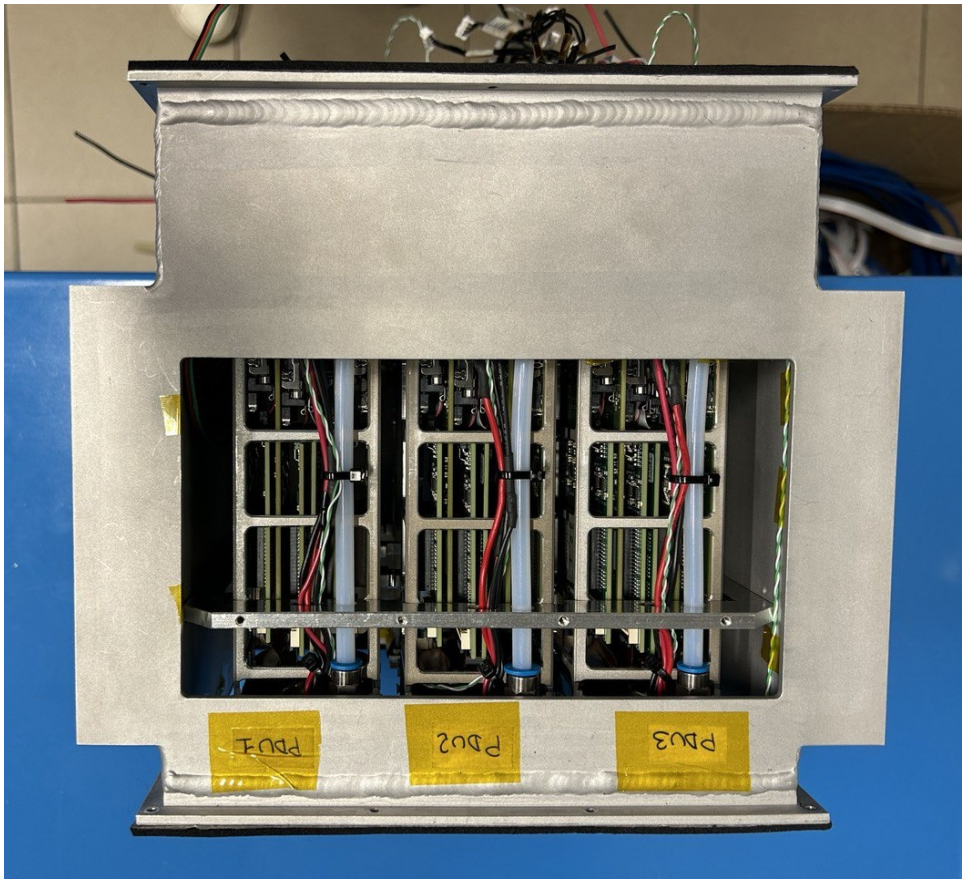

(b)

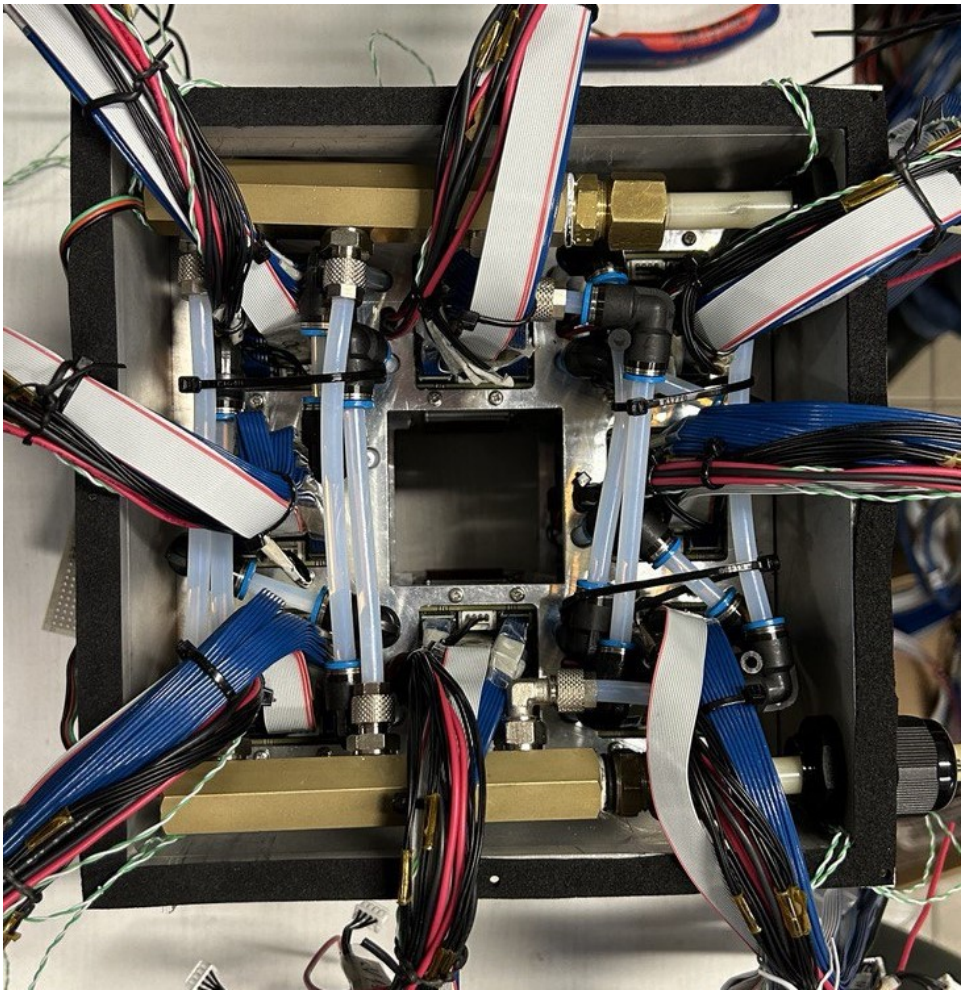

(c)

Figure 3.27: Front facing view (a), top view (b) and back side view (c) of the complete detector prototype box.

3.4 Test Beam Results

The prototype subject of this thesis has been used in the beam test conducted in May 2024.
The test beam setup at CERN is shown in Figure 3.28. In this section will be reported some of its results. With the test beam new data has been acquired, whose analysis is ongoing and the prototype has been successfully operated. The major focus of this test has been on light, radiators (aerogel and gas) and sensors suitability and the major data acquisitions have been done with the same detector configuration but different beams [30]. The major improvement in this latest dRICH detector prototype is that the full possible coverage of Cherenkov light detection has been obtained. The Beam Test marked a significant advancement in electronics, sensor characterization, and light detection, leading to a deeper understanding of the future dRICH detector for particle identification. The obtained results are shown in Figures 3.29, 3.30 and 3.31.

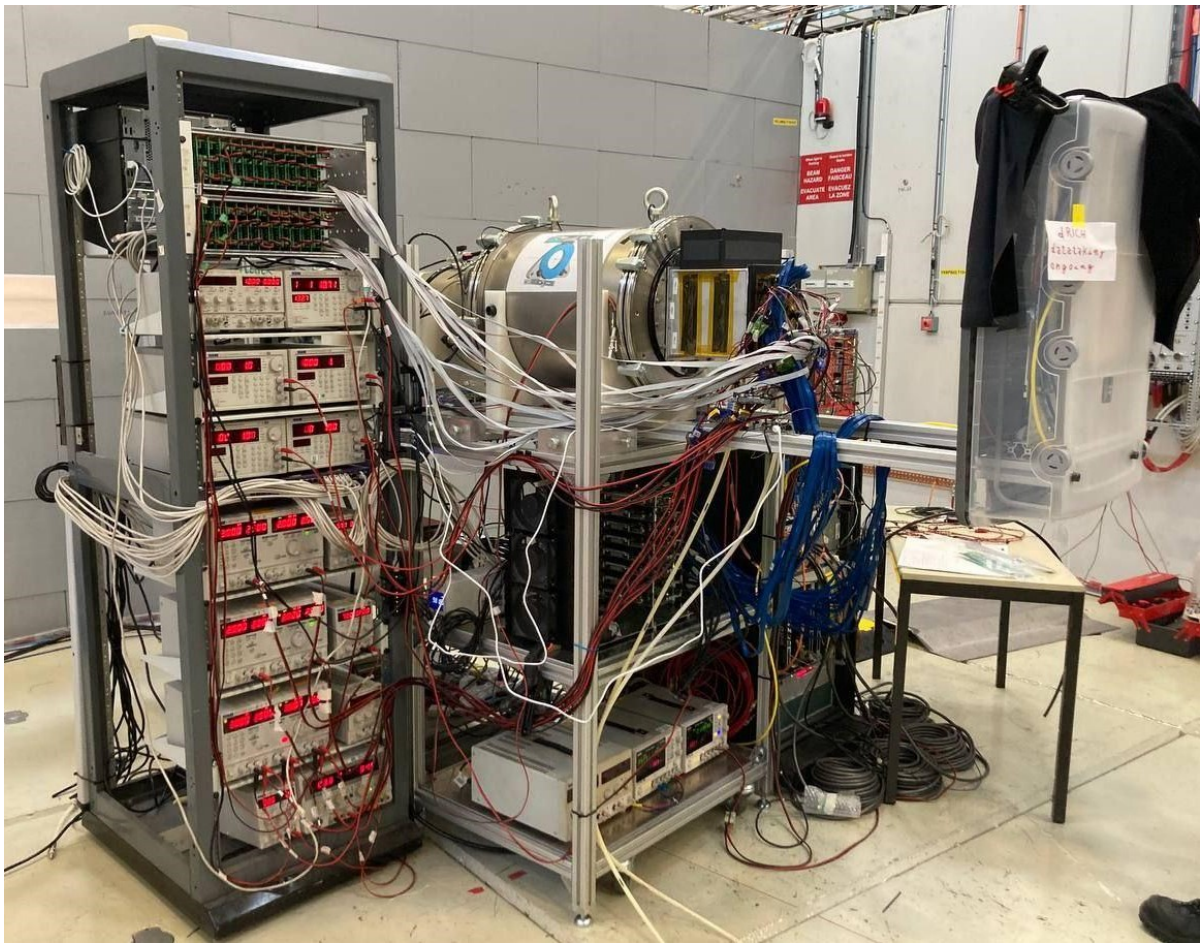

Figure 3.28: Beam test setup.

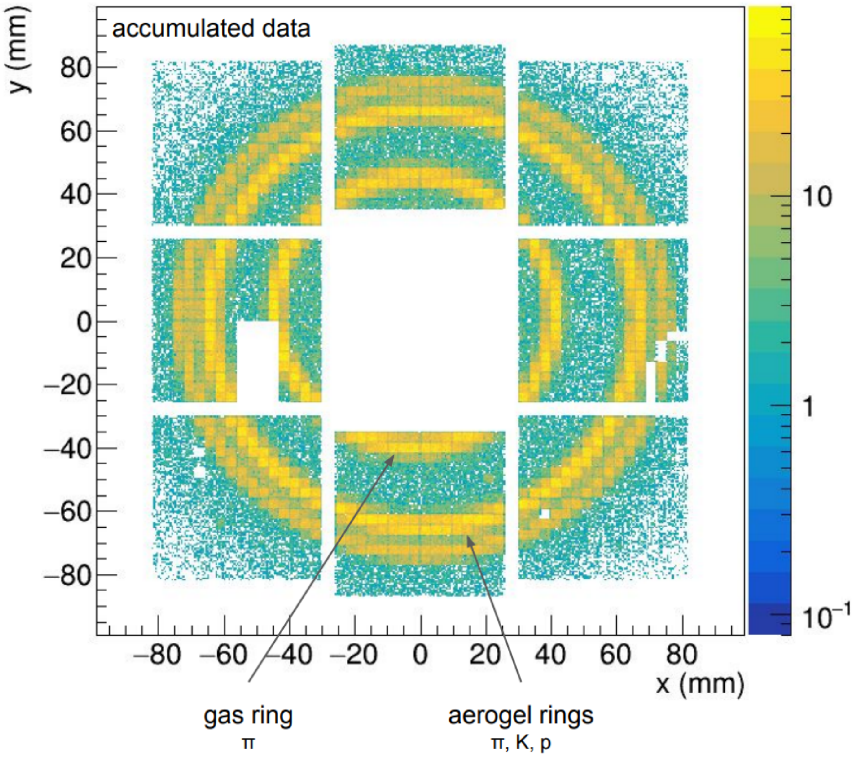

Figure 3.29: 10 GeV/c positive beam with no selection applied. The image shows the interplay between aerogel and gas radiator where gas ring tags pions. At 10 GeV/c kaons and protons are below C_2F_6 gas threshold. Unfortunately, one ASIC chip (32 ch) had some front-end problems.

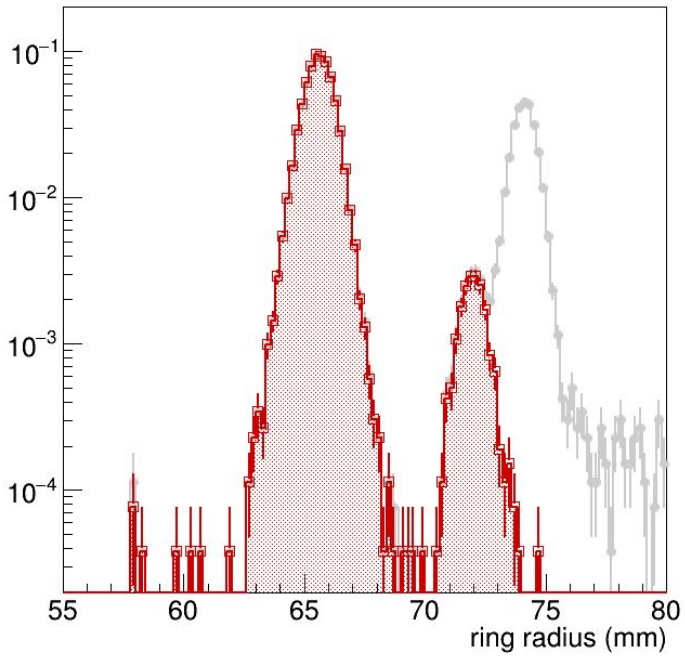

Figure 3.30: Reconstructed radii at 10 GeV/c with veto, which removes pions. Clear kaon identification at 10 GeV/c is observable [30].

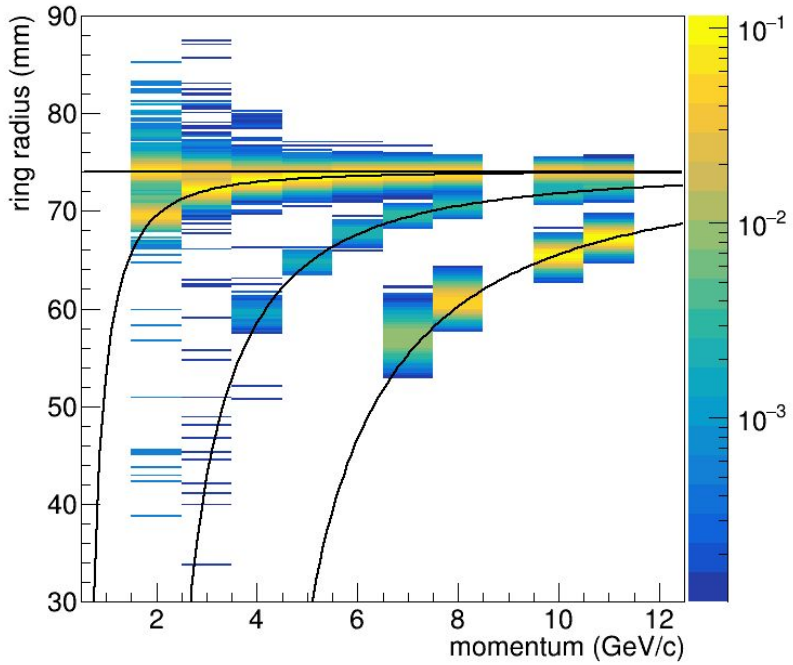

Figure 3.31: Beam with positive particles and only aerogel as radiator momentum scan. In the graph is reconstructed radii vs. beam momentum. Something went wrong with the beam configuration for 9 GeV [22]

Conclusions

The dRICH detector with integrated SiPM sensors will provide for particle identification through Cherenkov Radiation at the EIC.
This work aims to report the dRICH prototype readout box process of testing, characterization and construction. Firstly, were compared the temperature measurements of the NTC sensors mounted on the carrier boards with the ones assessed by the climatic chamber. The results on the difference in temperature at the four chosen levels of -30, -10, 10 and 30 $°C$ revealed a good state of all the NTC analyzed, with the largest inaccuracy of the NTC calibration at the higher temperature tested of 30 $°C$, however lower than a 2 $°C$ deviation. These plots show a mean relative difference of 0 ± 0.3 $°C$ at -30$°C$. With the obtained data has been derived an equation for the computing of the true temperature through NTC measurements. The deviation however, resulted smaller than the prototype requires and is negligible in correspondence with the working point of the prototype at sub-zero temperatures.
The proper functioning of the SiPMs and their communication through the electronics was analyzed via data acquisition of the Dark Count Rate (DCR), which confirmed their full operability. The assembly of the structure composed of the carrier board and thermoelectric cooling was completed and described, and its subsequent characterization for the PDU units S1375-1, S1375-2, S1375-3, and S1375-5 demonstrated correct adhesion of the thermal pad and the expected performance of the Peltier elements. Lastly, the entire box prototype, whose assembly is described, was subjected to a series of pre-commissioning tests, which are listed and outlined, to validate its performance. Some front-end problems were found and ended with the substitution of 2 ALCOR ASIC boards with properly functioning ones.
The fully equipped dRICH prototype box completely assembled and tested, with the complete ALCOR-based readout chain together with the SiPM optical readout has been successfully tested during the beam test in May 2024 at CERN showing the expected behavior. The data obtained now provide the foundation for a more precise characterization and understanding of the dRICH detector for particle identification, which will be constructed by 2030 as part of the EIC project.

Appendix A

A.1 NTC tests temperature difference graphs

In Figure A.1 and Figure A.2 are shown the graphs relative to the temperature difference ΔT for the NTCs 1, 2, 3 and 4 as a function of the climatic chamber temperature measures at -30, -10, 10 and 30 $°C$. The plot is carried out and reported below for the PDUs S1375-2, S1375-3, S1375-4, S1375-5, S1350-1, S1350-2, S1350-3 and S1350-4.

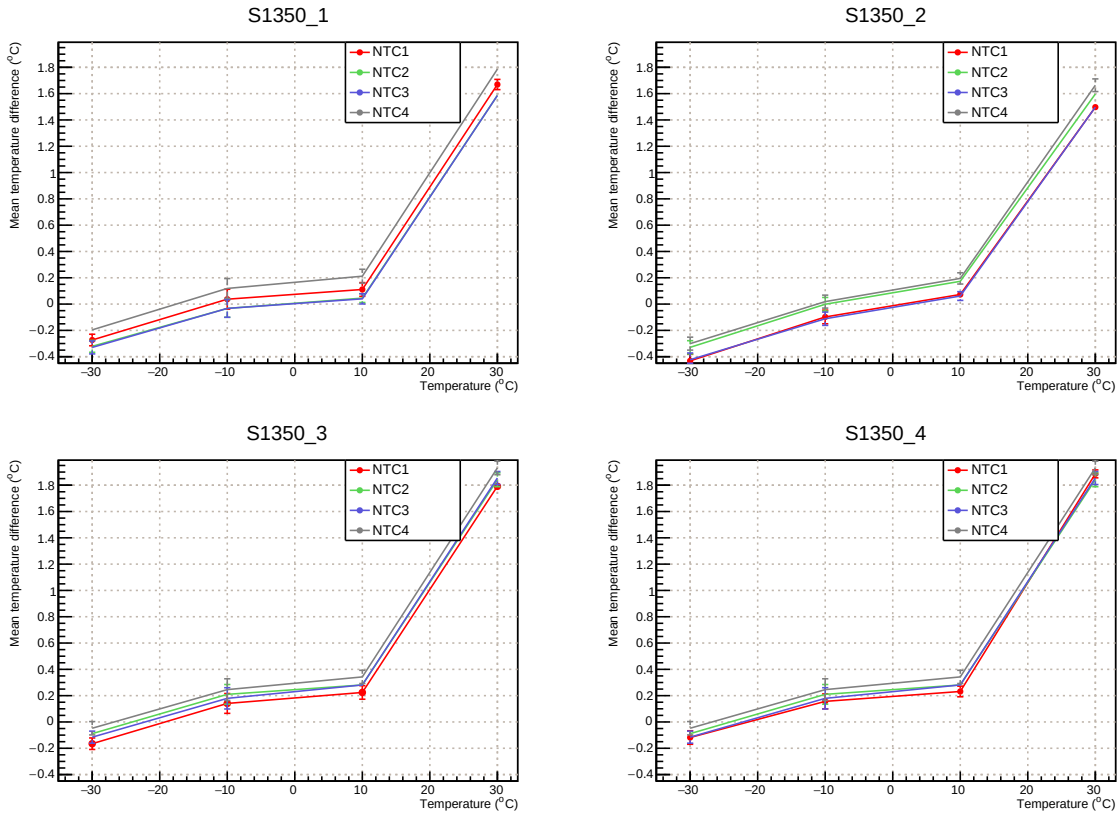

Figure A.1: Graph for S1350-1, S1350-2, S1350-3 and S1350-4 temperature measures differences.

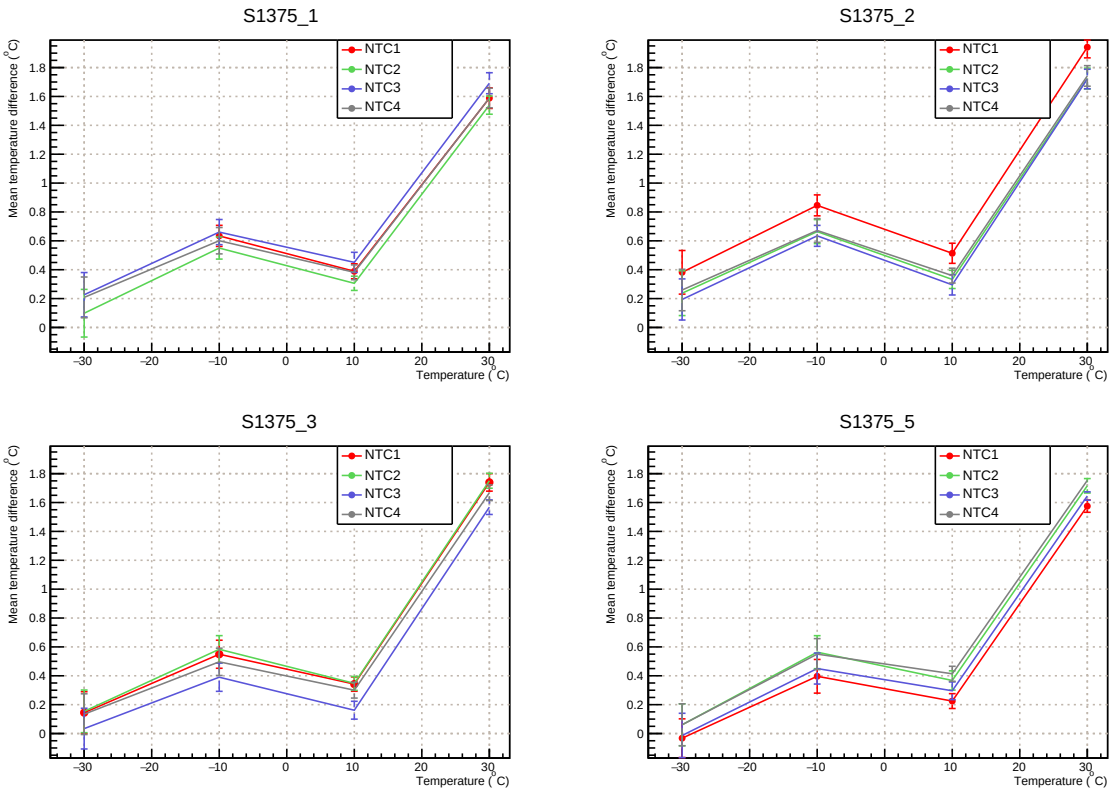

Figure A.2: Graph for S1375-1, S1375-2, S1375-3 and S1375-5 temperature measures differences.

A.2 Fit Graphs for the parameters of the NTC true value measure

In Figures A.3, A.4, A.5, A.6, A.7, A.8, A.9 and A.10 are shown the plots of the mean temperature difference ΔT as a function of the NTC mean measured temperature at -30, -10, 10, 30 $°C$. The parameters obtained from each third-degree polynomial fit are used in Section 3.2.2 to obtain the equation of the true temperature (T_{true}) as a function of the temperature measures of the NTCs (T_{NTC}).

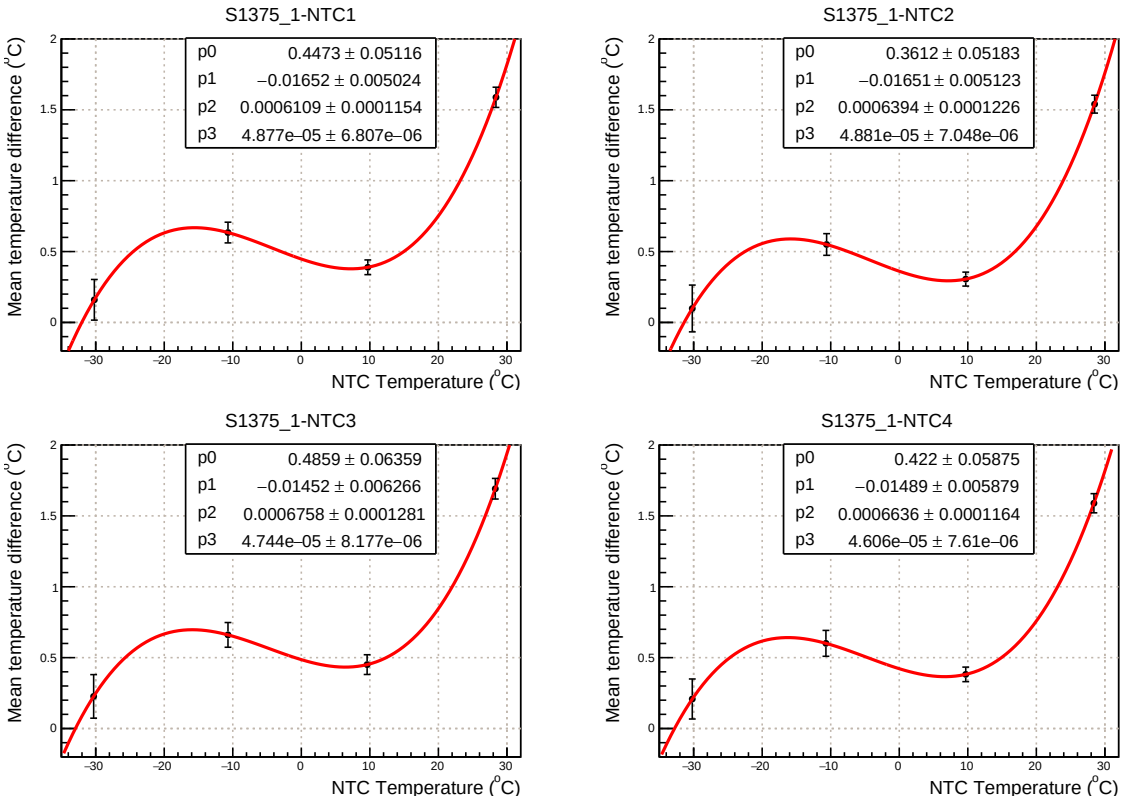

Figure A.3: Graph for the S1375-1 true temperature parameters.

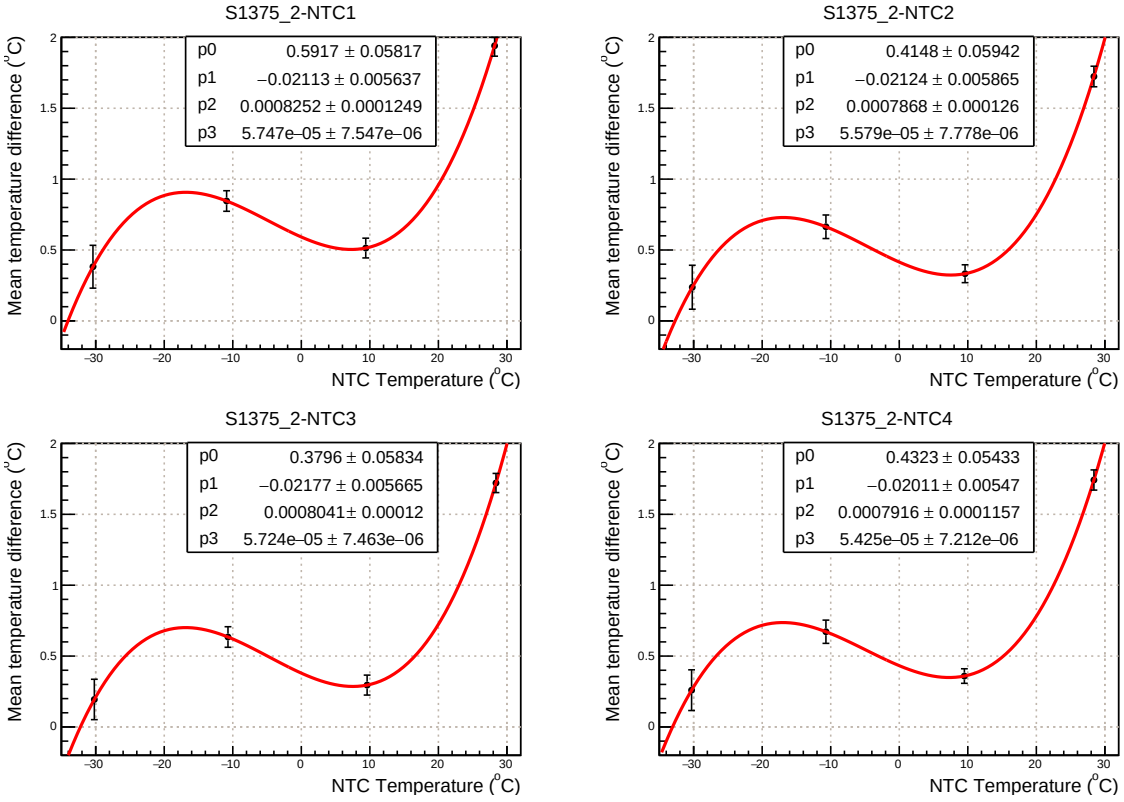

Figure A.4: Graph for the S1375-2 true temperature parameters.

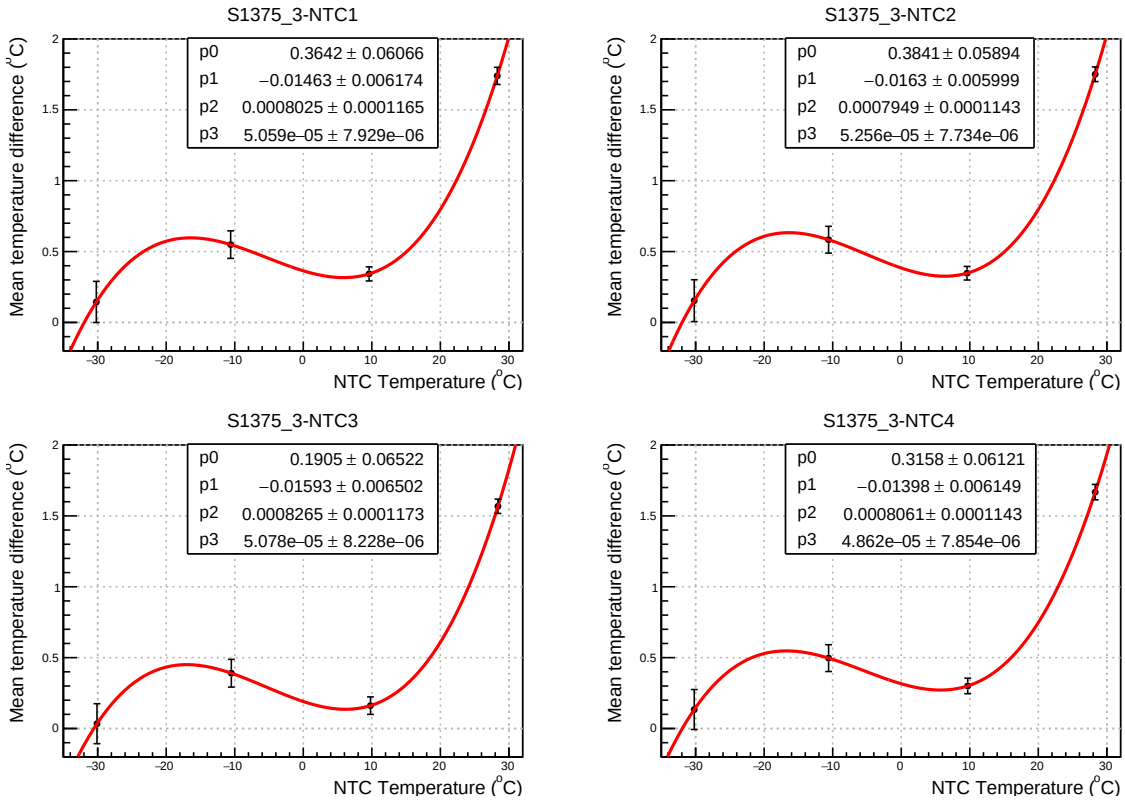

Figure A.5: Graph for the S1375-3 true temperature parameters.

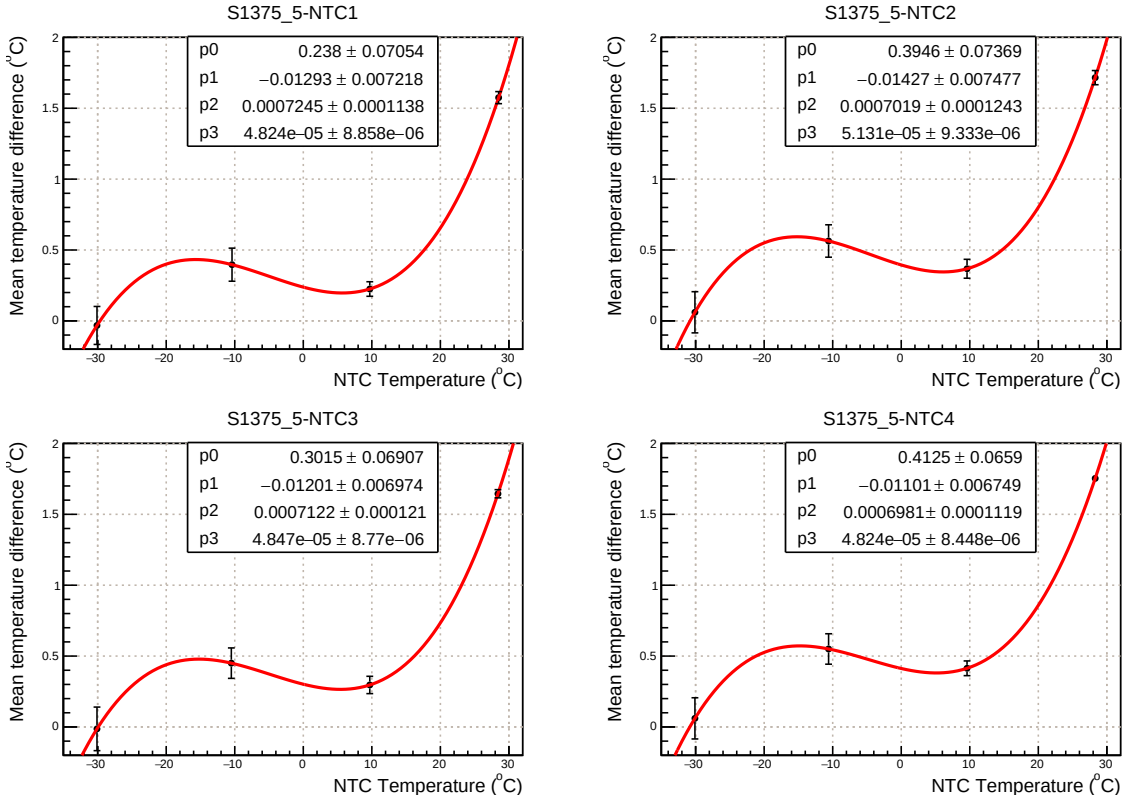

Figure A.6: Graph for the S1375-5 true temperature parameters.

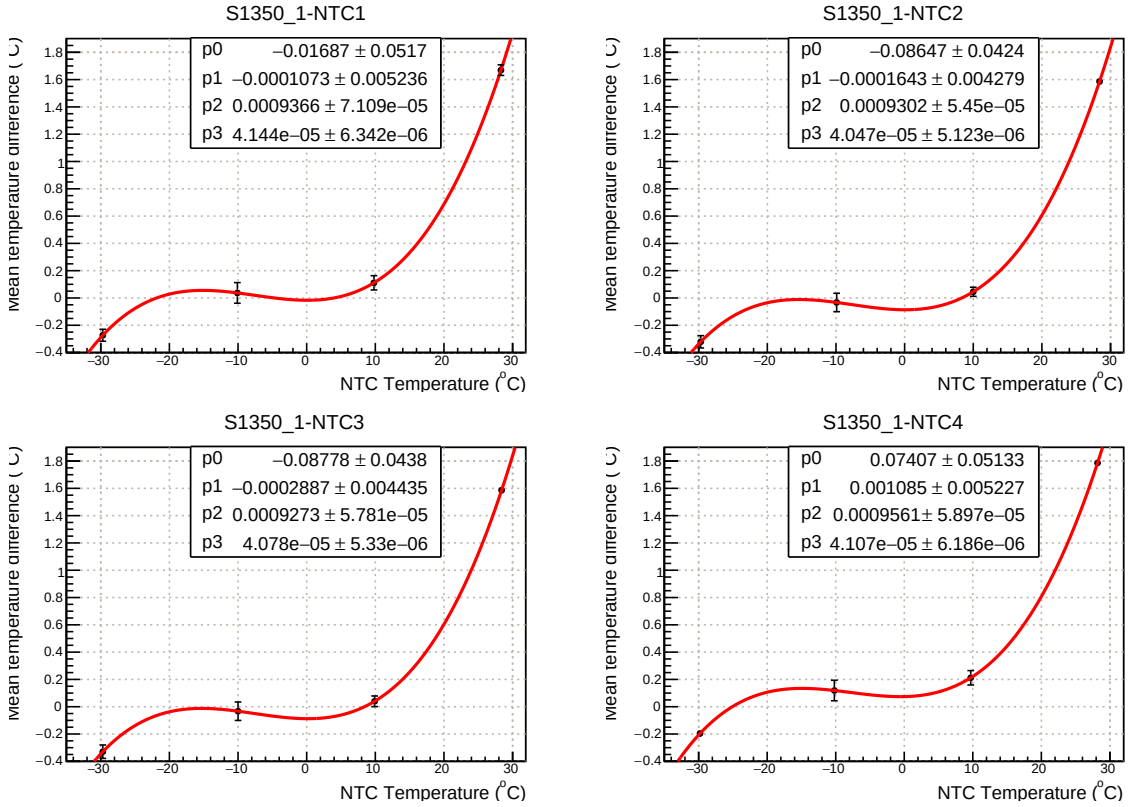

Figure A.7: Graph for the S1350-1 true temperature parameters.

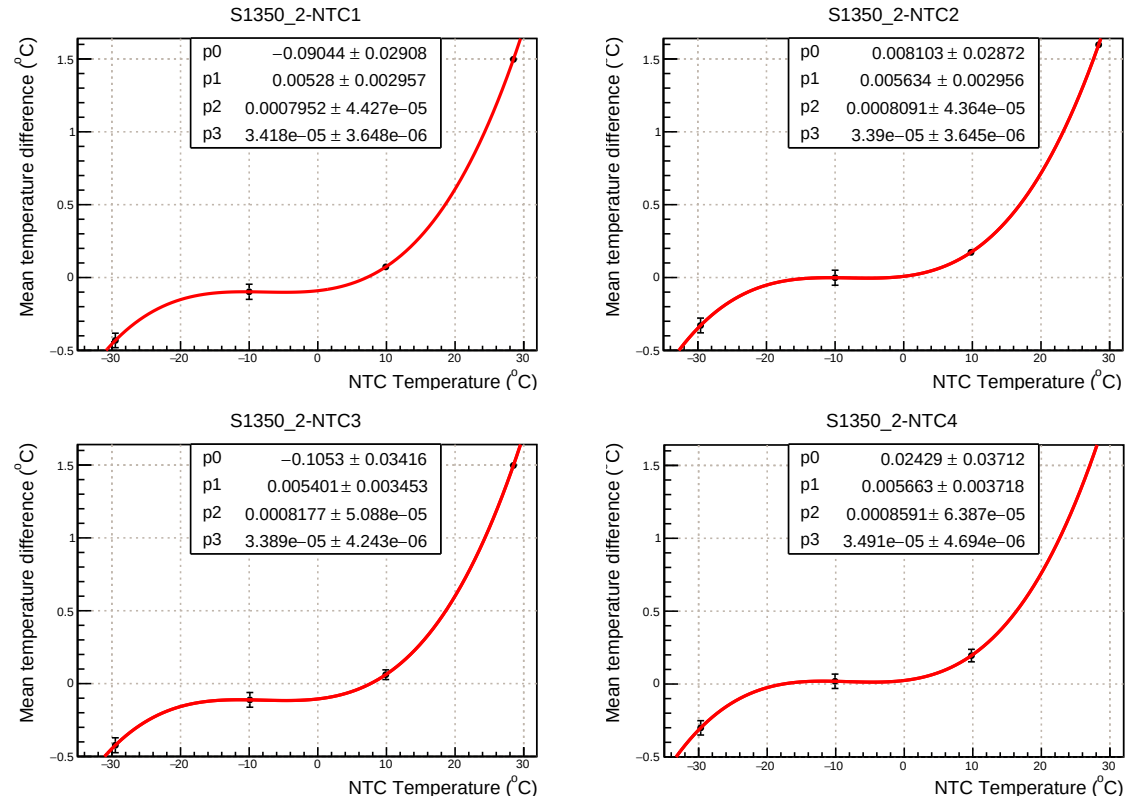

Figure A.8: Graph for the S1350-2 True temperature parameters.

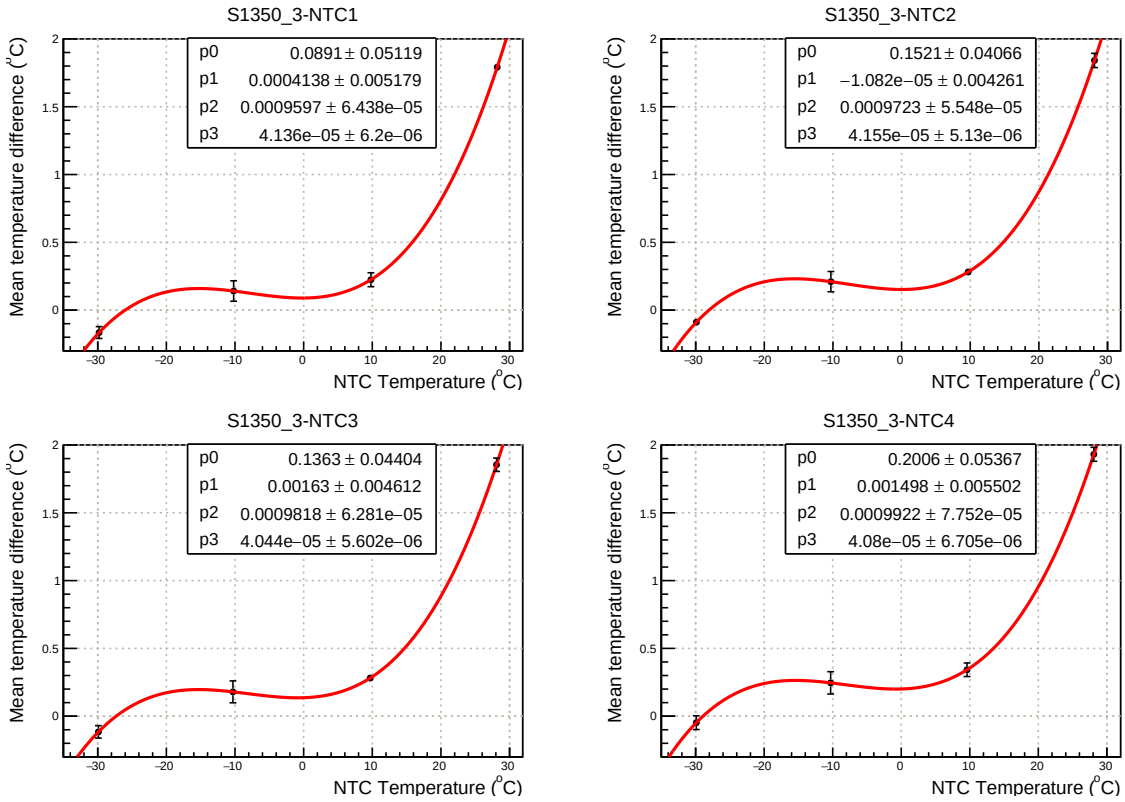

Figure A.9: Graph for the S1350-3 True temperature parameters.

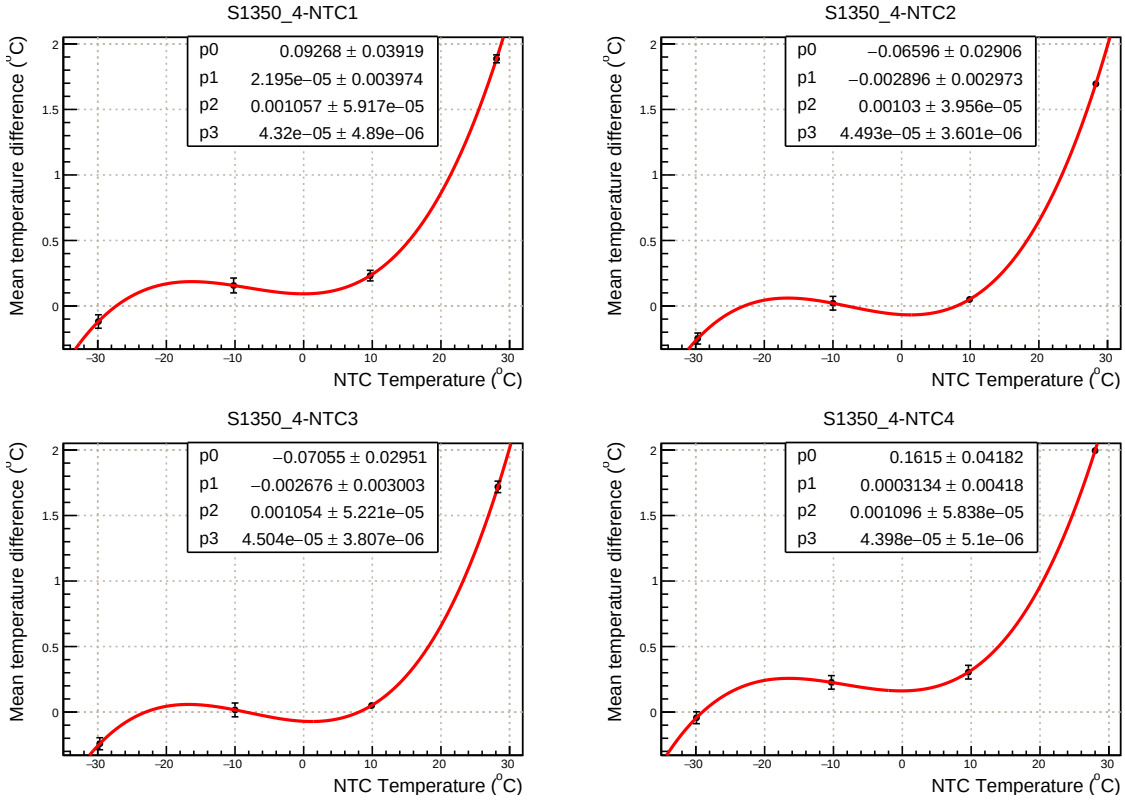

Figure A.10: Graph for the S1350-4 True temperature parameters.

Bibliography

[1] *ElectronIonCollider*. URL: https://www.bnl.gov/newsroom/news.php?a=219454 (cit. on p. 5).

[2] R. Abdul Khalek et al. "Science Requirements and Detector Concepts for the Electron-Ion Collider". In: *EIC Yellow Report* (2021). URL: https://arxiv.org/pdf/2103.05419 (cit. on pp. 5, 6, 22).

[3] A. Accardi et al. "Electron Ion Collider: The Next QCD Frontier. Understanding the glue that binds us all". In: *Nuclear Instruments and Methods in Physics Research* (2014). URL: https://www.bnl.gov/newsroom/news.php?a=219454 (cit. on pp. 5, 7–11).

[4] A.B. Dubna Arbuzov. "Quantum Field Theory and the Electroweak Standard Model". In: *arXiv:1801.05670* (2018) (cit. on p. 7).

[5] *Signs of Saturation Emerge from Particle Collisions*. URL: https://www.energy.gov/science/np/articles/signs-gluon-saturation-emerge-particle-collisions (cit. on p. 8).

[6] S. Dalla Torre. "The Electron-Ion Collider and the ePIC experiment". In: *Il Nuovo Cimento* (2023). URL: 10.1393/ncc/i2024-24144-6 (cit. on p. 10).

[7] *The ePIC Collaboration*. URL: https://www.bnl.gov/eic/epic.php (cit. on p. 11).

[8] *The dRICH photosensors: SiPM studies*. URL: https://agenda.infn.it/event/39909/contributions/236368/attachments/122702/179715/Rignanese%20giornate%20nazionali.pdf (cit. on pp. 12, 24).

[9] Claus Grupen Irène Buvat, ed. *Handbook of Particle Detection and Imaging*. Springer, 2012. DOI: 10.1007/978-3-642-13271-1 (cit. on p. 13).

[10] A.L. Efros B.I. Shklovskii, ed. *Electronic Properties of Doped Semiconductors*. Springer-Verlag Berlin Heidelberg, 1984 (cit. on pp. 15, 16).

[11] K. Kobayashi A. Ghassemi K.Sato. *A technical guide to silicon photomultipliers (MPPC)*. Hamamatsu Resources, 2021. URL: https://hub.hamamatsu.com/us/en/technical-notes/mppc-sipms.html (cit. on pp. 18, 19).

[12] *MPPCs (SiPMs) / MPPC arrays*. URL: https://www.hamamatsu.com/content/dam/hamamatsu-photonics/sites/documents/99_SALES_LIBRARY/ssd/s13360_series_kapd1052e.pdf (cit. on pp. 18, 19, 21, 22, 31).

[13] SensL. *An Introduction to the Silicon Photomultiplier*. URL: https://elearning.unimib.it/pluginfile.php/521118/mod_folder/content/0/SiPM.pdf (cit. on p. 20).

[14] B.R. Achari et al. F.Cossio. "ALCOR: A mixed-signal ASIC for the dRICH detector of the ePIC experiment at the EIC". In: *Elsevier B.V.* (2024). URL: https://doi.org/10.1016/j.nima.2024.169817 (cit. on pp. 22, 27).

[15] S. Gundacker F. Acerbi. "Understanding and simulating SiPMs," in: *Nuclear Inst. and Methods in Physics Research, A 926, 16–35* (2019). URL: https://doi.org/10.1016/j.nima.2018.11.118 (cit. on p. 23).

[16] Yu. Musienko E. Garutti. "Radiation damage of SiPMs". In: (2018). URL: https://arxiv.org/pdf/1809.06361.pdf (cit. on p. 23).

[17] S. H. Price. *The Peltier Effect and Thermoelectric Cooling*. 2007. URL: https://ffden-2.phys.uaf.edu/212_spring2007.web.dir/sedona_price/phys_212_webproj_peltier.html (cit. on pp. 24, 25).

[18] Meerstetter. *Peltier element design guide*. 2022. URL: https://www.meerstetter.ch/customer-center/compendium/32-tec-peltier-element-design-guide (cit. on p. 25).

[19] Ramshan Kugathasan. "A low-power mixed-signal ASIC for readout of SiPM at cryogenic temperatures". In: *Proceedings of Science* (2019). URL: hattps://pos.sissa.it/370/011 (cit. on p. 26).

[20] S. Vallarino et al. *Prototype of a dual-radiator RICH detector for the Electron-Ion Collider*. 2024. DOI: https://doi.org/10.1016/j.nima.2023.168834. URL: https://www.sciencedirect.com/science/article/pii/S0168900223008252 (cit. on pp. 29, 30).

[21] Chiara Alice et al. "A large-area SiPM readout plane for the ePIC-dRICH detector at the EIC: Realisation and beam test results". In: *Proceedings of Science* (2024). DOI: https://doi.org/10.1016/j.nima.2024.169669. URL: https://www.sciencedirect.com/science/article/pii/S0168900224005953 (cit. on p. 30).

[22] Roberto Preghenella. *A SiPM-based optical readout for the ePIC dual-radiator RICH*. 2024. URL: https://indico.cern.ch/event/1284854/contributions/5951359/attachments/2887220/5060533/%5B20240701%5D%5BiWorid%5D%20SiPM%20dRICH.pdf (cit. on pp. 30, 58).

[23] Weijing Shi et al. "Algorithm and hardware implementation for visual perception system in autonomous vehicle: A survey". In: *Integration* (2017). DOI: https://doi.org/10.1016/j.vlsi.2017.07.007. URL: https://www.sciencedirect.com/science/article/pii/S0167926017303218 (cit. on p. 31).

[24] *Grafana*. URL: https://grafana.com/ (cit. on p. 32).

[25] *Sensing Thermistor. What is an NTC Thermistor*. URL: https://www.ametherm.com/thermistor/ (cit. on p. 34).

[26] *memmert CTC256*. URL: https://www.memmert.com/en/products/climate-chambers/environmental-test-chambers/ctc256 (cit. on p. 34).

[27] *Teledyne Flir. FLIR Axxx Smart Sensor*. URL: https://www.flir.it/products/axxx-series-smart-sensor/?vertical=rd+science&segment=solutions (cit. on p. 34).

[28] Giovanni Chiesi et al. "Optimizing Silicon photomultipliers for Quantum Optics". In: *Scientific Reports* (2019). DOI: 10.1038/s41598-019-43742-1 (cit. on p. 40).

[29] *Tflex 600 Series Thermal Gap Filler*. URL: https://www.laird.com/sites/default/files/2023-06/Tflex%20600%20DS-011923.pdf (cit. on p. 47).

[30] Nicola Rubini. *dRICH test beam: results*. June 2024. URL: https://agenda.infn.it/event/41496/contributions/231961/attachments/122583/179480/%5B2024-06-21%5D%5Bepic-drich-beam-test-data-analysis%5D%5BT%5D%20dRICH%20test%20beam_%20results.pdf (cit. on pp. 56, 57).